Title
Discovery of Nanoscale Biophysics through Super Resolution Microscopy

Author
Wang, Bowen

Publication Date
2022

Discovery of Nanoscale Biophysics through Super Resolution Microscopy

by

Bowen Wang

A dissertation submitted in partial satisfaction of the

requirements for the degree of

Doctor of Philosophy

in

Chemistry

in the

Graduate Division

of the

University of California, Berkeley

Committee in charge:

Professor Ke Xu, Chair
Professor Steven Conolly
Professor John Groves

Fall 2022

Abstract

Discovery of Nanoscale Biophysics through Super Resolution Microscopy

by

Bowen Wang

Doctor of Philosophy in Chemistry

University of California, Berkeley

Professor Ke Xu, Chair

Unveiling the nanoscale structural mechanism is believed to be key of understanding the nature of biology. In the last 15 years, the advancement of super resolution microscopy, especially *ST*ochastic *O*ptical *R*emonstration *M*icroscopy (STORM) or *S*ingle *M*olecule *L*ocalization *M*icroscopy (SMLM), equivalently brought the resolution of optical microscopy down to ~10nm and thus enabled many disrupting biological discovery. In this dissertation, I initially show the how the spatial resolution of optical microscopy could be largely increased through the development of photo-switchable fluorophore and single molecule localization algorithm. Then, I use two interesting examples to show how STORM could provide new angle in fundamental cell biology research. First, I illustrate the discovery of a novel structural model of tubular endoplasmic reticulum as well as its regulation mechanism by curvature formation protein, Rtn4, and luminal bridge, Climp63. Second, I apply STORM to demonstrate the actin associated vesicle scission mechanism of clathrin coated pits during eukaryote endocytosis. In the last Chapter, I make some future outlook the in the recent development of functional super resolution microscopy, which not only achieve higher spatial resolution but also encode useful physicochemical insight in the image.

Acknowledgements

I would like to sincerely thank my supervisor, Prof. Ke Xu, for giving me day-to-day guidance through my Ph.D. study. I would never be able to accomplish the amazing scientific discoveries in this dissertation without his help and encouragement. I also learn how to stay curious and optimistic about science and research from him, which help me overcome many difficult moments in the past few years. I would also like to thank my co-workers, Dr. Limin Xiang, Dr. Kun Chen, Dr. Wan Li, Dr. Jeongmin Kim, Dr. Changdong He, Dr. Michal Wojcik, Dr. Megen Hauser, Dr. Samuel Kenny, Dr. Rui Yan, Miss Yunqi Li, Mr. Ha Park, Mr. Bret Unger, Mr. Alexander Choi, Miss Sinyoung Jo and Mr.Tylor Jepson. I would never have such a wonderful journey without them. I would like to give special like to thank my knowledgeable and motivated undergrad mentees, Mr. Zhiheng Zhao, Mr. Micheal Xiong and Miss Tong Zhan. It is my honor to work with them all and I really appreciated to all their contribution to the projects. In the end, I would also like to thank my family and friends giving me endless support during this period.

Table of Content

Table of Figure

Chapter 1: Overview

Understanding biology is a long term dream of humanity. The major difficulty comes from the small nature of the living system. To look at this question more closely, I give a few examples below. The size of a single cell is about 10-50μm, which is comparable to the diameter of human hair. Size of mitochondria, the power house of eukaryotic cell, is about 1-2μm. The cross section of microtubule, part of the cytoskeleton, is only 50nm and the size of an antibody could be down to 5nm. Also, most of the important biological processes are achieved by nanometer scale bio-machinery. A typical example could be the ATP-synthase complex in the inner surface of mitochondria that produce ATP driving by the ionic gradient across the membrane. Thus, to understand the structural organization as well as the associated biophysical principle behind, advanced research tool are always in demand.

Optical microscopy has been widely used for biology research, however, due to the wave nature of light, the resolution of optical microscopy is limited by diffraction. In reality, any infinite small emitter will form a ratio symmetric intensity profile on the camera and its full width half max (FWHM) was defined as the diffraction limit. The mathematical expression of diffraction limit can be approximated to $\boldsymbol{d}=\mathbf{0.61}\frac{\lambda}{\boldsymbol{NA}}$, where λ is the wavelength of light and *NA* stands for the numerical aperture, which represent the light collecting efficiency of the objective. For example, if the wavelength of light is about 600nm and applying high numerical aperture objective, NA can be as high as 1.45, the diffraction limit can be calculated to be about 252nm. In other words, if we gradual move two fluorophore toward each other, they we be look like a single peak when they are closer than the 252nm. This fundamental limit make the study of small biological feature in subcellular space inaccessible for long.

About 15 years ago, a few interesting method was introduced to overcome the diffraction limit using photoactivable protein or photo switchable organic fluorophores. They were named as (fluorescence-) photo-activated localization microscopy ((f)-PALM) or stochastic optical reconstruction microscopy (STORM)[1-3]. The core technology of these method are both making the fluorophores quickly switch on and off, or "blink"[4]. PALM is achieved by using a photo-activable protein. During experiment, majority of fluorophores was switched of by string laser and then a tiny small fraction was reactivated by a weak UV light[1]. With a similar mechanism, STORM was achieved by applying photo-switchable dye[5]. By blinking single molecule, we could capture the image of image of each blinking event and localized the center of each molecule. Approximately, the resolution of each localization was inverse related to the photon count of each blinking event, or $\boldsymbol{d_{STORM}} = \frac{\boldsymbol{d}}{\sqrt{\boldsymbol{N}}}$, where N represent the photon count of each single molecule event. Thus, by stacking tens of thousand localization center, the image could be reconstructed with much higher resolution. By inserting other optical element in the light path (i.e. a cylindrical lens), we could also estimate the z-depth of each localization and thus enable the three dimensional super resolution microscopy[6]. Currently, super resolution has been wildly applied in biology and unveil many fundamental phenomenon of living system[7-9].

Although STORM has dramatically increase the resolution of optical microscopy, majority of bright fluorophore was discovered in the 647nm excited channel, or red channel. In chapter 2 of this dissertation, I will introduce a strategy to optimize the photo-switching behavior of rhodamines for (d)STORM super-resolution microscopy. By replacing the benzene ring in the rhodamine core with a permanently charged 1,3-disubstituted imidazolium, the resultant dyes are markedly sensitized toward photo-switching, and exhibit outstanding (d)STORM performance with fast on-off switching, long-lasting blinking, and bright single-molecule emission. We thus attain excellent (d)STORM images under green excitation that are on par with the "ideal" red-excited dyes, including for difficult structures such as the mammalian actin cytoskeleton, and demonstrate high-quality two-color three-dimensional (d)STORM.

In the next few chapter of this dissertation, I will use a few examples to demonstrate the power of STORM in the biological research:

In chapter 3, I describe an interesting discovery about the endoplasmic reticulum (ER), a versatile organelle with diverse functions in eukaryote cell. Through super resolution microscopy, we show that the peripheral ER in the mammalian cell adopts two distinct forms of tubules. Whereas an ultrathin form, R1, is consistently covered by ER-membrane curvature-promoting proteins, for example, Rtn4 in the native cell, in the second form, R2, Rtn4 and analogs are arranged into two parallel lines at a conserved separation of ~105 nm over long ranges. The two tubule forms together account for ~90% of the total tubule length in the cell, with either one being dominant in different cell types. The R1–R2 dichotomy and the final tubule geometry are both coregulated by Rtn4 (and analogs) and the ER sheet–maintaining protein Climp63, which, respectively, define the edge curvature and lumen height of the R2 tubules to generate a ribbon-like structure of well-defined width. Accordingly, the R2 tubule width correlates positively with the Climp63 intraluminal size. The R1 and R2 tubules undergo active remodeling at the second/subsecond timescales as they differently accommodate proteins, with the former effectively excluding ER-luminal proteins and ER-membrane proteins with large intraluminal domains. We thus uncover a dynamic structural dichotomy for ER tubules with intriguing functional implications.

In chapter 4, I will elaborate the application of STORM to the unveil the role of actin during clathrin mediated endocytosis (CME). Actin assembly facilitates vesicle formation in several trafficking pathways, including CME. Interestingly, actin does not assemble at all CME sites in mammalian cells. How actin networks are organized with respect to mammalian CME sites and how assembly forces are harnessed, are not fully understood. Here, branched actin network geometry at CME sites was analyzed using three different advanced imaging approaches. When endocytic dynamics of unperturbed CME sites are compared, sites with actin assembly show a distinct signature, a delay between completion of coat expansion and vesicle scission, indicating that actin assembly occurs preferentially at stalled CME sites. In addition, N-WASP and the Arp2/3 complex are recruited to one side of CME sites, where they are positioned to stimulate asymmetric actin assembly and force production. We propose that actin assembles preferentially at stalled CME sites where it pulls vesicles into the cell asymmetrically, much as a bottle opener pulls off a bottle cap.

In chapter 5, I will make an future outlook of the current emerging possibilities to encode functional information of intracellular microenvironments, for example, local pH, small-molecule concentrations, chemical polarity (hydrophobicity), and protein activity, into diverse dimensions of the super-resolution signal, hence a class of approaches we collectively refer to as functional super-resolution microscopy. By adding remarkably rich functional information to the already powerful super-resolution arsenal, functional super-resolution microscopy transcends the structural information provided by existing methods, and opens up new ways to unveil fascinating local heterogeneities in live cells with nanometer-scale spatial resolution and ultimate sensitivity down to the single-molecule level.

Publications listed below was largely reproduced in this dissertation. Permission has been granted by all critical co-authors for the reproduction of the work in this dissertation:

B. Wang, M. Xiong, J. Susanto, X. Li, W.-Y. Leung, K. Xu, "Transforming rhodamine dyes for (d)STORM super-resolution microscopy via 1,3-disubstituted imidazolium substitution," Angew. Chem. Int. Ed., 61, e202113612, 2022.

B. Wang, Z. Zhao, M. Xiong, R. Yan, K. Xu, "The endoplasmic reticulum adopts two distinct tubule forms," Proc. Natl. Acad. Sci. U.S.A., 119, e2117559119, 2022.

M. Jin, C. Shirazinejad, B. Wang, A. Yan, J. Schöneberg, S. Upadhyayula, K. Xu, D. G. Drubin, "Branched actin networks are organized for asymmetric force production during clathrin-mediated endocytosis in mammalian cells," Nat. Commun., 13, 3578, 2022.

R. Yan, B. Wang, K. Xu, "Functional super-resolution microscopy of the cell," Curr. Opin. Chem. Biol., 51, 92-97, 2019.

Publications listed here were collaboration with other lab members although not discussed in this dissertation:

Y. Li, W. Li, M. Wojcik, B. Wang, L.-C. Lin, M. B. Raschke, K. Xu, "Light-assisted diazonium functionalization of graphene and spatial heterogeneities in reactivity," J. Phys. Chem. Lett., 10, 4788-4793, 2019.

Y. Li, B. Wang, W. Li, K. Xu, "Dynamic, spontaneous blistering of substrate-supported graphene in acidic solutions," ACS Nano, 16, 6145-6152, 2022.

R. Yan, K. Chen, B. Wang, K. Xu, "SURF4-induced tubular ERGIC selectively expedites ER-to-Golgi transport," Dev. Cell, 57, 512-525, 2022.

W. Li, Y. Li, B. Wang, K. Xu, "Visible-Light Azidation and Chemical Patterning of Graphene via Photoredox Catalysis" J. Phys. Chem. C . Accepted

REFERENCE

1. Betzig, E., Patterson, G. H., Sougrat, R., Lindwasser, O. W., Olenych, S., Bonifacino, J. S., Davidson, M. W., Lippincott-Schwartz, J. & Hess, H. F. Imaging intracellular fluorescent proteins at nanometer resolution. *Science* **313,** 1642-1645 (2006).
2. Hess, S. T., Girirajan, T. P. K. & Mason, M. D. Ultra-high resolution imaging by fluorescence photoactivation localization microscopy. *Biophys. J.* **91,** 4258-4272 (2006).
3. Rust, M. J., Bates, M. & Zhuang, X. Sub-diffraction-limit imaging by stochastic optical reconstruction microscopy (STORM). *Nature methods* **3,** 793-796 (2006).
4. Xu, K., Shim, S.-H. & Zhuang, X. Super-resolution imaging through stochastic switching and localization of single molecules: an overview, in *Far-Field Optical Nanoscopy*, edited by P. Tinnefeld, C. Eggeling & S. W. Hell (Springer, Berlin, 2015), pp. 27-64.
5. Dempsey, G. T., Vaughan, J. C., Chen, K. H., Bates, M. & Zhuang, X. Evaluation of fluorophores for optimal performance in localization-based super-resolution imaging. *Nat. Methods* **8,** 1027-1036 (2011).
6. Huang, B. *et al.* Three-dimensional Super-resolution Imaging by Stochastic Optical Reconstruction Microscopy. *Science* **319**, 810-813 (2008).
7. Möckl, L. & Moerner, W. E. Super-resolution microscopy with single molecules in biology and beyond-essentials, current trends, and future challenges. *J. Am. Chem. Soc.* **142,** 17828-17844 (2020).
8. Sigal, Y. M., Zhou, R. & Zhuang, X. Visualizing and discovering cellular structures with super-resolution microscopy. *Science* **361,** 880-887 (2018).
9. Shim, S. H., Xia, C., Zhong, G., Babcock, H. P., Vaughan, J. C., Huang, B., Wang, X., Xu, C., Bi, G. Q. & Zhuang, X. Super-resolution fluorescence imaging of organelles in live cells with photoswitchable membrane probes. *Proc. Natl. Acad. Sci. U. S. A.* **109,** 13978-13983 (2012).

Chapter 2: Transforming rhodamine dyes for (d)STORM super-resolution microscopy via 1,3-disubstituted imidazolium substitution

The work in this chapter was conducted in collaboration with Michael Xiong, Josephine Susanto, Xue Li, Wai-Yee Leung, Ke Xu. It is reproduced in part here from Wang et al. with permission from all co-authors. Copyright 2022 *Angew. Chem. Int. Ed.*

Introduction

The recent rise of super-resolution microscopy methods based on single-molecule localization has revolutionized how we study biology and beyond.[1-7] Through stochastic on-off switching of single-molecule fluorescence emission in the wide-field, the positions of millions of molecules are individually localized over many camera frames to construct super-resolution images that achieve ~10 nm spatial resolutions. Methods based on the photoswitching of synthetic dyes,[8-15] often known as (d)STORM [(direct) stochastic optical reconstruction microscopy], have remained popular for the high single-molecule brightness and thus resolution.

The identification and development of suitable photoswitchable dyes are central to (d)STORM.[15-20] Whereas multiple dyes excited by red (*e.g.*, 647 nm) lasers, *e.g.*, derivatives of the cyanine dye Cy5, perform optimally for (d)STORM, it remains challenging to obtain comparable performances for other color channels, especially in buffers already optimized for the red-excited dyes, namely oxygen-removed buffers containing thiols. Thus, high-quality multicolor (d)STORM remains difficult. Although alternative approaches have been developed to circumvent the lack of an ideal dye outside the red excitation, *e.g.*, color identification through activation,[9] distinguishing different red-excited dyes via split-plane or spectral imaging,[21,22] and reusing the same dye through sequential labeling,[23] they incur different complications and limitations.

An earlier study[15] has systematically examined the (d)STORM performance of 26 common fluorescent dyes across the visible spectrum, and concludes that "the red dyes Alexa Fluor 647, Cy5 and Dyomics 654 performed considerably better than even the best-performing dyes in other spectral regions". It then identifies Cy3B as a workable dye for green (*e.g.*, 560 nm) excitation, although noting inferior photoswitching behaviors. From our experience, although Cy3B allows two-color (d)STORM with red-excited dyes,[24,25] a major fraction of the labeled molecules do not efficiently photoswitch but are instead photobleached, thus creating problems for lowly labeled samples or when complex structures need to be resolved. We and others have since moved to a newer dye, CF568, for (d)STORM in the non-red channel.[26,27] However, together with other dyes that have been used in (d)STORM, *e.g.*, rhodamine derivatives as Alexa Fluor 532 (AF532) and Atto 565,[13,15] the achieved photoswitching efficiency and (d)STORM performance are still far from ideal.

Here we introduce a strategy to improve the photoswitching behavior of rhodamines for optimal (d)STORM performance. Consequently, we report two green-excited dyes that perform on par with red-excited dyes, and achieve high-quality two-color (d)STORM with red-excited dyes.

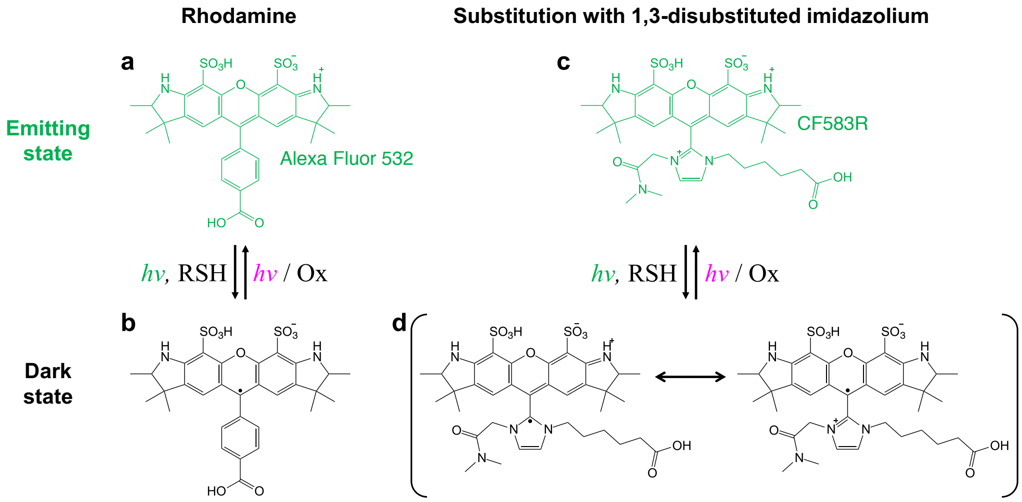

Scheme 1. Sensitizing rhodamine for photoswitching. (a) Structure of Alexa Fluor 532, a representative fluorescent rhodamine dye. (b) In a deoxygenated buffer containing thiol reductants, the excited molecule gains one electron to form a stable radical dark state. This dark state can be reverted to the original fluorescent state using violet light or an oxidant. (c) Structure of CF583R, in which the benzene ring in the rhodamine core is substituted by a positively charged 1,3-disubstituted imidazolium. (d) The permanent positive charge on the imidazolium ring facilitates electron capture to form a stable radical with a resonance structure.

Result and Discussion

The photoswitching mechanisms of rhodamines (*e.g.*, Scheme 1a for AF532) under (d)STORM conditions have been previously examined in detail.[14] In a deoxygenated buffer, the excited rhodamine is reduced by thiols to generate a long-lived radical as the dark state (Scheme 1b), whereas the application of violet light or an oxidant (*e.g.*, oxygen) removes the added lone electron and revert the molecule to the emitting state.

We reason that replacing the benzene ring in the rhodamine core with a positively charged 1,3-disubstituted imidazolium (*e.g.*, Scheme 1c for CF583R) may "sensitize" the dye for the photoswitching process: The permanent positive charge on the imidazolium ring may facilitate electron capture, and the resultant radical may be stabilized by a resonance structure (Scheme 1d).

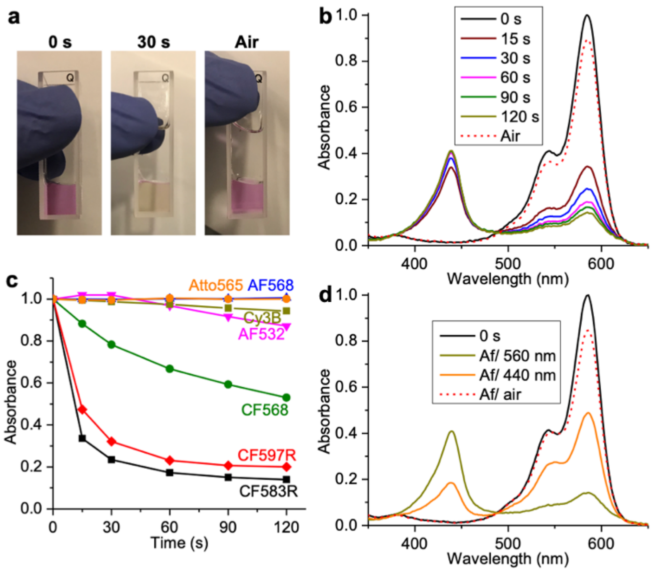

Figure 1.**CF583R and CF597R are highly sensitized for photoswitching**. (a) CF583R in a typical Tris-based (d)STORM buffer containing 100 mM cysteamine and an oxygen scavenger, before (left) and after (middle) 30 s illumination with the white LED light of a cellphone, and then after 30 s air bubbling (right). (b) Normalized absorption spectra of 10 μM CF583R in the same buffer, before and after 560 nm illumination at ~10 mW/cm^2 for different durations (solid lines), and then after the sample was infused with air (red dashed line). Curves are normalized to the peak height of the initial spectrum. (c) Normalized absorption peak heights for different dyes in the same buffer, after the same 560 nm illumination for different durations, except for AF532, for which ~10 mW/cm^2 illumination at 532 nm was used instead to match the absorption peak. (d) Normalized absorption spectra of 10 μM CF583R in the (d)STORM buffer, before (black) and after (yellow) 560 nm illumination at ~10 mW/cm^2 for 120 s, after 440 nm illumination at ~10 mW/cm^2 for 240 s (orange), and then after infused with air (red dashed line).

Indeed, we found that CF583R, as well as CF597R, another dye based on the same imidazolium-substitution design but with further spectral redshift through modification to the xanthene structure, were highly sensitized toward photoswitching. Illuminating both dyes in the typical cysteamine-containing, oxygen-removed (d)STORM buffer with the white LED light of a common cellphone induced fast decoloration (Fig. 1a), whereas under the same condition, AF532 and other green-excited (d)STORM dyes showed no visible color changes (not shown). The photoswitching was highly reversible. Bubbling the sample with air fully recovered the dye color (Fig. 1a), reminiscent of previous observations that for rhodamines, the radical dark state is readily oxidized by air to recover the fluorescent state (Scheme 1).[14]

Spectroscopic characterizations quantified the above dramatic photoswitching behaviors (Fig. 1b). For CF583R, the imidazolium substitution redshifted the dye absorption peak to 586 nm. Illuminating the sample with a modest power of ~10 mW/cm^2 at 560 nm led to a quick drop of the 586 nm peak in seconds, accompanied by the rise of a new peak at 439 nm attributed to the dark radical state.[14,28] The 586 nm peak rapidly dropped to the baseline at ~>30 s (Fig. 1bc); the ~14% residual absorption is comparable to that is previously reported in the photoswitching of rhodamines, and may be attributed to disturbances during the experiment that reverted a fraction of the radical.[14,28] Infusing the sample with air led to an ~90% recovery of the original 586 nm peak. CF597R based on the same imidazolium-substitution design exhibited similar photoswitching behaviors (Fig. 1c and Fig. 2).

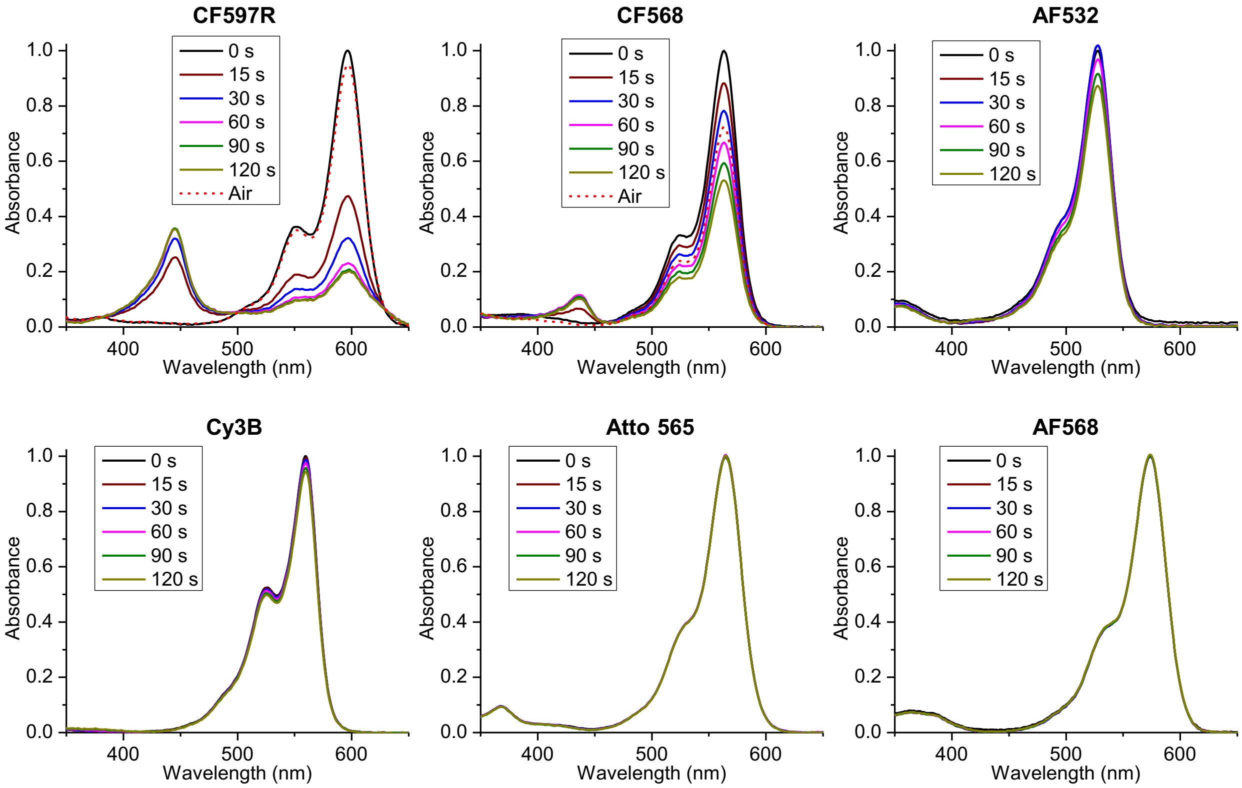

Figure 2. **Photoswitching effects of green excitation light on different dyes**, similar to that shown for CF583R in Figure 1b. Normalized absorption spectra are shown for the different dyes in the same Tris-based, oxygen-removed (d)STORM buffer containing 100 mM cysteamine, before and after 532 nm (for AF532) or 560 nm (for other dyes) illuminations at ~10 mW/cm^2 for different durations (solid lines). For CF597R and CF568, which exhibited noticeable photoswitching, the sample was next infused with air, which led to the near-complete recovery of the original absorption spectrum for CF597R and partial recovery for CF568 (red dashed lines).

As we compared the spectral behavior of other green-excited (d)STORM dyes, we found that AF532, Cy3B, Atto 565, and AF568 all exhibited very limited photoswitching under the same excitation power, with the latter two yielding no discernable spectral changes (Fig. 1c and Fig. 2). CF568, in which the benzene ring in the rhodamine core is substituted with an 1-monosubstituted imidazole, showed more noticeable, yet still substantially slower photoswitching when compared to CF583R and CF597R (Fig. 1c and Fig. 2). Thus, substitution with the permanently charged 1,3-disubstituted imidazolium was instrumental in sensitizing rhodamine toward photoswitching.

The radical dark states of CF583R and CF597R were also readily reverted with violet (440 and 405 nm) illuminations (Fig. 1d, Fig. 3, and Fig. 4), a behavior similar to that of rhodamines.[14] Curiously, the photoactivation stabilized to ~50% recovery, so that the solution became a mixture of the initial and photoswitched forms. This steady state was converted to the initial form upon air infusion (Fig. 1d). These results were explained by our observation that directly applying violet illuminations to the initial CF583R and CF597R solutions also generated comparable mixtures of the two forms (Fig. 3 and Fig. 4). Thus, the highly sensitized CF583R and CF597R were photoswitched in both directions by violet illuminations.

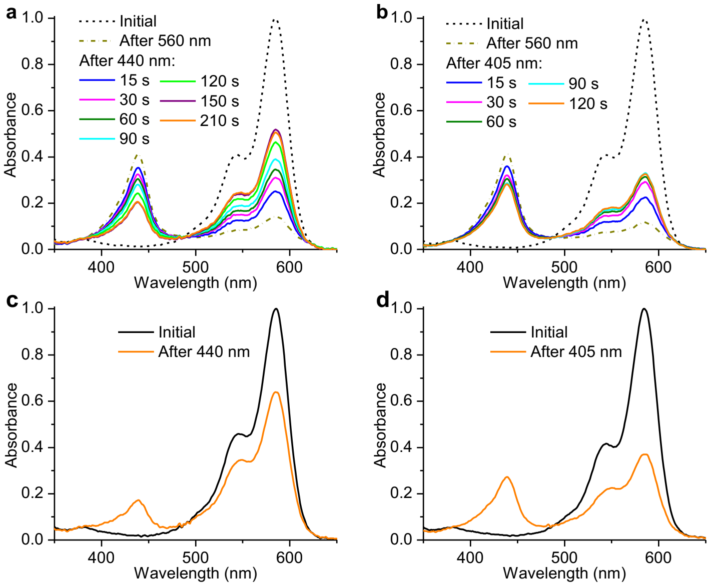

Figure 3**. Photoswitching effects of violet illuminations on CF583R.** (a) Normalized absorption spectra of 10 μM CF583R in the (d)STORM buffer. Black dashed line: spectrum of the initial solution. Yellow dot-dash line: after 560 nm illumination at ~10 mW/cm^2 for 120 s. Solid lines: next after 440 nm illumination at ~10 mW/cm^2 for different durations. Curves are normalized to the peak height of the initial spectrum. (b) Similar to (a), but with ~10 mW/cm^2 405 nm illumination of different durations for the solid lines. (c) Normalized absorption spectra of 10 μM CF583R in the (d)STORM buffer, before (black) and directly after (orange) 440 nm illumination at ~10 mW/cm^2 for 240 s. (d) Similar to (c), but with ~10 mW/cm^2 405 nm illumination.

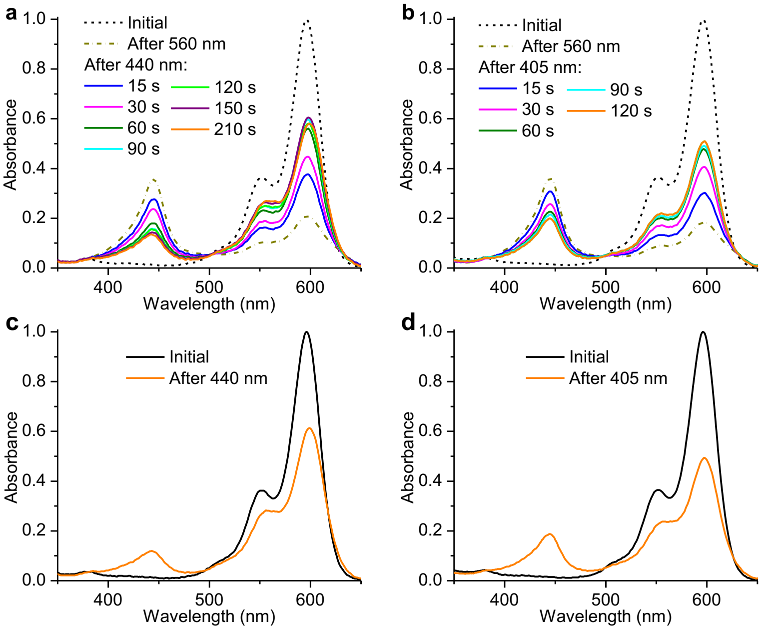

Figure 4. **Photoswitching effects of violet illuminations on CF597R**. Panels (a)-(d) are arranged the same way as Figure 3.

With the above demonstrated highly sensitized photoswitching capacity of CF583R and CF597R, we next examined the (d)STORM performance of the two dyes. Here, we immunolabeled microtubules in fixed COS-7 cells using secondary antibodies conjugated with different green-excited dyes. The samples were mounted with the typical cysteamine-containing, oxygen-removed (d)STORM imaging buffer above, and illuminated at ~1.5 kW/cm^2 at 532 nm (for AF532) and 560 nm (for other dyes) on a typical three-dimensional (3D) (d)STORM setup.[29] An EM-CCD camera recorded the resultant fluorescence at 110 frames per second (FPS) for ~100,000 frames. A 405 nm illumination was further applied at 0-5 W/cm^2 with gradually increasing power during the process, as needed, to sustain single molecules in the view.

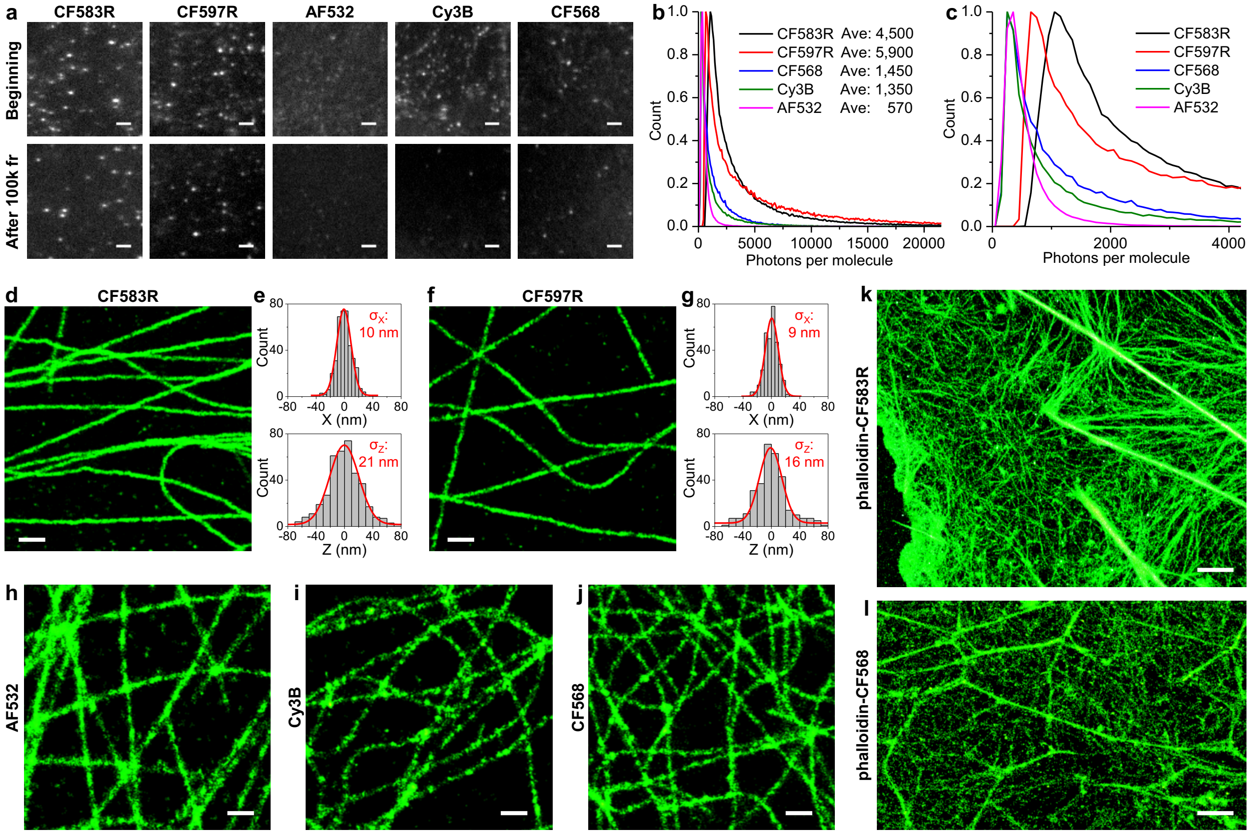

Figure 5. **Comparison of (d)STORM performance for different green-excited dyes.** (a) Typical single-molecule images recorded in (d)STORM, at the beginning of the experiment (top row) and after continuous recording of 100,000 frames at 110 fps (bottom row). Results from five dyes are shown on the same brightness scale. (b) Distributions of single-molecule photon counts for the five dyes in (d)STORM, with their average values labeled in the legend. (c) Zoom-in of (b) for the lower photon counts. (d) A typical (d)STORM image of CF583R-labeled microtubules in a fixed COS-7 cell. (e) Localization distributions of single CF583R molecules in the sample, in the X (in-plane; top) and Z (depth; bottom) directions, respectively. Gaussian fits (red curves) give standard deviations of 10 and 21 nm, respectively. (f,g) Similar to (d,e), but for CF597R. Gaussian fits give standard deviations of 9 and 16 nm for the in-plane and in-depth directions, respectively. (h-j) Typical (d)STORM image of microtubules in fixed COS-7 cells labeled by AF532 (h), Cy3B (i), and CF568 (j). (k,l) Typical (d)STORM images of the actin cytoskeleton in fixed COS-7 cells labeled by phalloidin-CF583R (k) and phalloidin-CF568 (l). All experiments were performed in the typical Tris-based (d)STORM buffer containing 100 mM cysteamine and an oxygen scavenger. Scale bars: 2 μm (a,k,l), 500 nm (d,f,h-j).

CF583R and CF597R both performed excellently under these typical (d)STORM settings, so that single molecules rapidly blinked on and off in successive frames with high brightness over low backgrounds (Fig. 5a). The blinking of single molecules was well-maintained over continuous illumination and recording over >100,000 frames (Fig. 5a). In comparison (Fig. 5a), AF532 showed markedly lower single-molecule brightness; Cy3B showed acceptable brightness, but blinked poorly by staying in the emitting state for multiple frames and exhibiting big drops in the count of blinking molecules after prolonged imaging; CF568 exhibited workable brightness and blinking, but was noticeably subpar in both aspects when compared to CF583R and CF597R.

Quantification of single-molecule photon counts showed exponential-like distributions with mean values of 4,500 and 5,900 for CF583R and CF597R, respectively (Fig. 5bc). These results are similar to the optimal results obtained for the red-excited dyes in the same imaging buffer (*e.g.*, AF647).[15,30] In comparison, CF568 and Cy3B showed lower single-molecule photon counts at 1,450 and 1,350 (Fig. 5bc), with the additional caveat that they also photo-switched less well, as discussed above. AF532 yielded low single-molecule photon counts with a mean value of 570 (Fig. 5bc).

The above contrasting single-molecule performances translated into substantial differences in the final 3D-STORM images. With bright single-molecule blinking well-maintained over >100,000 frames, CF583R and CF597R both yielded high-resolution images with good continuity and uniformity along the microtubules (Fig 5df). The achieved single-molecule localization precisions[29,30] (as standard deviations) for CF583R were 10 nm and 21 nm for the in-plane and in-depth directions, respectively (Fig. 5e), comparable to that is achieved with the "optimal" red-excited dyes.[9,29] CF597R yielded yet slightly tighter distributions of 9 nm in-plane and 16 nm in-depth (Fig. 5g).

In contrast, visibly blurrier STORM images were obtained with AF532 (Fig. 5f) due to its dim single-molecule signals. Cy3B showed acceptable localization precisions, but yielded uneven brightness along the microtubules (Fig. 5g) owing to its poor photo-switching. CF568 performed better than Cy3B, yet the result was still noticeably inferior to CF583R and CF597R (Fig. 5h). Together, these results demonstrated substantially improved (d)STORM performance *via* imidazolium substitution for CF583R and CF597R, with trends well correlated with the photoswitching capability (Fig. 1c).

For a more challenging target, we examined phalloidin-labeled actin cytoskeleton in mammalian cells. Due to the small sizes and high densities of actin filaments, good (d)STORM images are previously limited to high-performance red-excited dyes,[30,31] while less optimal results have been obtained with the blue-excited dye Atto 488.[5,32] CF583R-phalloidin performed well in (d)STORM, resolving individual actin filaments with good continuity (Fig. 5k). In comparison, CF568, which we showed above as the next-best green-excited dye after CF583R and CF597R, yielded smeared and discontinuous images when labeling the actin cytoskeleton through phalloidin (Fig. 5l), as expected owing to its lower single-molecule brightness and less optimal photoswitching capabilities.

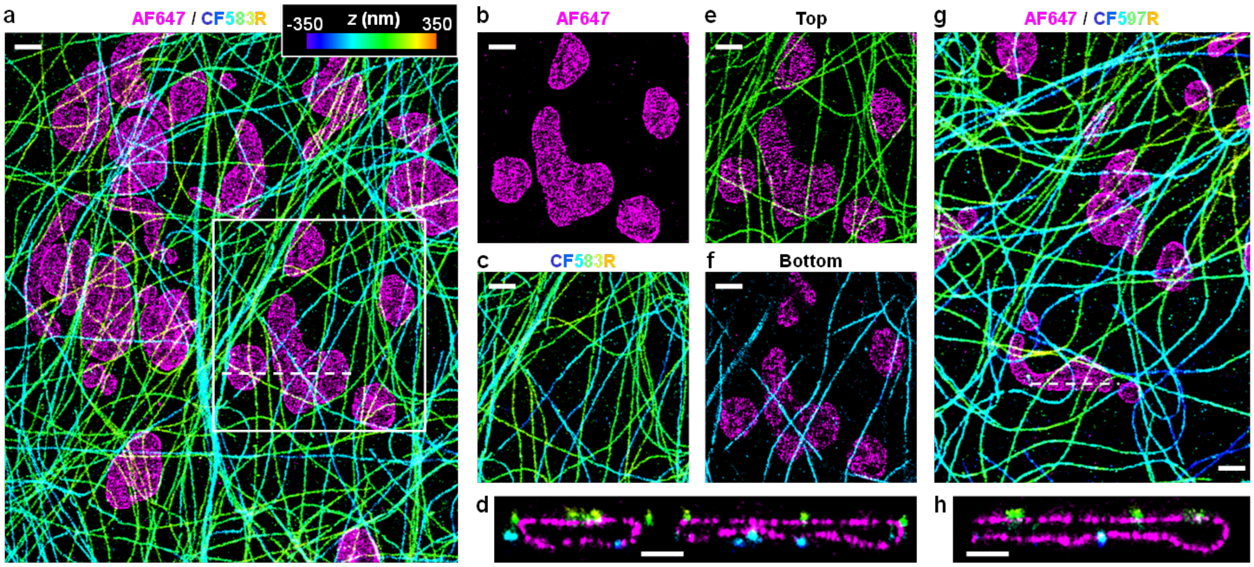

Figure 6. **Two-color 3D-(d)STORM of CF583R or CF597R with AF647**. (a) Overlaid 3D-(d)STORM images of CF583R-labeled tubulin (color-coded for depth Z) and AF647-labled mitochondrial outer membrane marker Tom20 (magenta) in a fixed COS-7 cell. (b,c) The separated CF583R and AF647 channels for the boxed region in (a). (d) Vertical cross-section along the dashed line in (a). (e,f) In-plane sections for the same boxed region in (a), for two depths at the top (e) and bottom (f) of the mitochondrial surface, respectively. (g) Overlaid 3D-(d)STORM images of CF597R-labeled tubulin (colored for z depth) and AF647-labeled Tom20 (magenta). (h) Vertical cross-section along the dashed line in (g). Scale bars: 1 μm (a-c, e-g); 500 nm (d, h).

As our above good (d)STORM performances under green excitation were attained in a medium that was already optimized for red-excited dyes, we next readily achieved high-quality two-color 3D-(d)STORM. To this end, we double-labeled mitochondria and microtubules in fixed cells using AF647 and CF583R/CF597R. 3D-(d)STORM was then sequentially performed for the two targets using 647 and 560 nm excitations, respectively. As expected, good images were obtained for both color channels for both the AF647-CF583R (Fig. 6a-f) and AF647-CF597R (Fig. 6gh) combinations, with no crosstalk observed between the 647-nm and 560-nm excited channels (Fig. 6bc) thanks to the large spectral differences. Virtual vertical cross-sections clearly resolved the hollow mitochondrial membrane, while also showing microtubules abutting the mitochondrial surface from the outside (Fig. 6dh). In-plane virtual sections thus visualized different layers of microtubules running below and above the mitochondria (Fig. 6ef).

Conclusion

In conclusion, we demonstrated that replacing the benzene ring in the rhodamine core with the permanently charged 1,3-disubstituted imidazolium substantially sensitized rhodamines toward photoswitching in the typical thiol-containing (d)STORM buffer. The resultant CF583R and CF597R exhibited outstanding (d)STORM performance with fast on-off switching, long-lasting blinking, and bright single-molecule emission. High-quality (d)STORM images on par with that of the “ideal” red-excited dyes were thus achieved under green excitation, including for the challenging structure of the actin cytoskeleton, and we further demonstrated high-quality two-color 3D-(d)STORM. We thus identified a new pathway toward the optimization of (d)STORM dyes. Generalizing the concept and approach developed in this work to other rhodamines and dye structures for an extended palette represents an exciting future direction.

Material and Methods

Fluorescent dyes and antibodies. CF583R succinimidyl ester (96084) and phalloidin (00064), CF597R succinimidyl ester (96092), and CF568 succinimidyl ester (92131) and phalloidin (00044) are commercially available from Biotium. Cy3B succinimidyl ester was from Cytiva (PA63101). Atto 565 was from Sigma (75784). AF532 succinimidyl ester was from Fluoroprobes (1041-1). AF568 carboxylic acid was from Lumiprobe (15890). Primary antibodies: Mouse monoclonal (IgG1) anti-α-tubulin (Sigma, T6199) and rabbit anti-Tom20 (Proteintech, 11802-1-AP). Secondary antibodies: Goat anti-mouse IgG1 from Jackson Immuno Research (115-005-205) was conjugated with the above succinimidyl esters to label ~2 dyes per antibody. AF647-conjugated goat anti-rabbit IgG was from ThermoFisher (A-21245).

Spectral characterizations. Dyes were hydrolyzed in Dulbecco's Phosphate-Buffered Saline (DPBS), and then added at ~10 μM into the (d)STORM imaging buffer: 100 mM Tris-HCl (pH 7.5) with the addition of 100 mM cysteamine (Sigma-Aldrich, 30070), 5% (w/v) glucose, 0.8 mg/mL glucose oxidase (Sigma-Aldrich, G2133), and 40 μg/mL catalase (Sigma-Aldrich, C30). Absorption spectra were recorded using a NanoDrop 2000c spectrometer (Thermo Fisher) in the cuvette mode, with the top of the cuvette oil-sealed. For photoswitching of the initial dye solutions, green lasers at 532 and 560 nm were expanded to achieve homogeneous illumination of the cuvette at ~10 mW/cm^2. For back-converting the photoswitched dyes, light-emitting diodes at 405 and 440 nm were used to illuminate the sample at ~10 mW/cm^2. Air infusion is performed by pipetting ~1 mL air bubbles into the solution.

Cell samples. COS-7 cells (University of California Berkeley Cell Culture Facility) were cultured on #1.5 coverslips in Dulbecco's Modified Eagle Media (DMEM) supplemented with 10% fetal bovine serum. For labeling of the actin cytoskeleton, cells were first fixed with 0.3% glutaraldehyde (Electron Microscopy Sciences, #16365) and 0.25% Triton X-100 in the cytoskeleton buffer (10 mM MES buffer, 150 mM NaCl, 5 mM EGTA, 5 mM glucose, 5 mM $MgCl_2$, pH 6.1) for 1 min, and then fixed with 2% glutaraldehyde in the cytoskeleton buffer for 30 min.[30] The sample was then treated twice with freshly prepared 0.1% (w/w) $NaBH_4$ solutions followed by three additional washes with DPBS. Actin was labeled with a 0.5-μM CF583-phalloidin or CF568-phalloidin solution in DPBS for 30 min, and then washed with DPBS for 5 min for two times. Other samples were fixed with 3% (v/v) paraformaldehyde (Electron Microscopy Sciences, #15714) and 0.1% (v/v) glutaraldehyde in DPBS for 20 min, and then washed twice with 0.1% (w/w) $NaBH_4$ followed by three additional washes with DPBS. Samples were then blocked and permeabilized using a DPBS-based blocking buffer containing 0.1% (w/w) saponin (Sigma-Aldrich, S4521) and 3% (w/w) BSA (Sigma-Aldrich, A3059) for 30 min. Samples were next incubated with diluted primary antibodies in the blocking buffer overnight at 4 °C, and washed three times with washing buffer (0.1x blocking buffer diluted with DPBS). Samples were then incubated with diluted dye-labeled secondary antibodies in the blocking buffer for 30 min, followed by three additional washes with the washing buffer.

(d)STORM super-resolution microscopy. (d)STORM was performed on a homebuilt inverted microscope using a Nikon CFI Plan Apo λ 100x oil-immersion objective (NA = 1.45), as described previously.[26,33] The dye-labeled samples on coverslips were mounted onto microscope slides with the same imaging buffer as described above, and sealed at the edge with Cytoseal. Lasers of 647 nm (for AF647), 532 nm (for AF532), or 560 nm (for other dyes) excited the sample at ~1.5 kW/cm^2. The angle of incidence was slightly below the critical angle of total internal reflection, thus illuminating a few micrometers into the sample. A 405-nm activation laser was applied at 0-5 W/cm^2 with gradually increasing power during the experiment, as needed, to sustain single molecules in the view. The resulting stochastic photoswitching of single-molecule fluorescence was recorded using an Andor iXon Ultra 897 EM-CCD camera at 110 frames per second, for a total of ~100,000 frames per image. For 3D localization, a cylindrical lens was inserted to create astigmatism for encoding the single-molecule depth (Z) information.[29] The raw STORM data were analyzed using previously described methods.[8,9,29] Single-molecule localization distributions were obtained using well-isolated clusters in the analyzed STORM data,[29,30] which were due to the repeated activation and hence detection of the same molecule in different frames. For each dye, single-molecule localizations from ~25 such clusters, each containing >10 localizations, were aligned by their center of mass to generate the localization distributions and histograms.

Conflict of interest: Biotium holds patents on heterocycle-based rhodamines and markets CF dyes.

Acknowledgements. K.X. is a Chan Zuckerberg Biohub investigator and acknowledges support by National Science Foundation (CHE-1554717) and the Packard Fellowships for Science and Engineering.

References

1. Xu, K., Shim, S.-H. & Zhuang, X. Super-resolution imaging through stochastic switching and localization of single molecules: an overview, in *Far-Field Optical Nanoscopy*, edited by P. Tinnefeld, C. Eggeling & S. W. Hell (Springer, Berlin, 2015), pp. 27-64.
2. Sauer, M. & Heilemann, M. Single-molecule localization microscopy in eukaryotes. *Chem. Rev.* **117,** 7478-7509 (2017).
3. Baddeley, D. & Bewersdorf, J. Biological insight from super-resolution microscopy: what we can learn from localization-based images. *Annu. Rev. Biochem.* **87,** 965-989 (2018).
4. Möckl, L. & Moerner, W. E. Super-resolution microscopy with single molecules in biology and beyond-essentials, current trends, and future challenges. *J. Am. Chem. Soc.* **142,** 17828-17844 (2020).
5. Jimenez, A., Friedl, K. & Leterrier, C. About samples, giving examples: optimized single molecule localization microscopy. *Methods* **174,** 100-114 (2020).
6. Lelek, M., Gyparaki, M. T., Beliu, G., Schueder, F., Griffié, J., Manley, S., Jungmann, R., Sauer, M., Lakadamyali, M. & Zimmer, C. Single-molecule localization microscopy. *Nat. Rev. Methods Primers* **1,** 39 (2021).
7. Xiang, L., Chen, K. & Xu, K. Single molecules are your quanta: A bottom-up approach toward multidimensional super-resolution microscopy. *ACS Nano* **15,** 12483-12496 (2021).
8. Rust, M. J., Bates, M. & Zhuang, X. Sub-diffraction-limit imaging by stochastic optical reconstruction microscopy (STORM). *Nat. Methods* **3,** 793-795 (2006).

9. Bates, M., Huang, B., Dempsey, G. T. & Zhuang, X. W. Multicolor super-resolution imaging with photo-switchable fluorescent probes. *Science* **317,** 1749-1753 (2007).
10. Bock, H., Geisler, C., Wurm, C. A., Von Middendorff, C., Jakobs, S., Schonle, A., Egner, A., Hell, S. W. & Eggeling, C. Two-color far-field fluorescence nanoscopy based on photoswitchable emitters. *Appl. Phys. B-Lasers Opt.* **88,** 161-165 (2007).
11. Heilemann, M., van de Linde, S., Schuttpelz, M., Kasper, R., Seefeldt, B., Mukherjee, A., Tinnefeld, P. & Sauer, M. Subdiffraction-resolution fluorescence imaging with conventional fluorescent probes. *Angew. Chem.-Int. Edit.* **47,** 6172-6176 (2008).
12. Folling, J., Bossi, M., Bock, H., Medda, R., Wurm, C. A., Hein, B., Jakobs, S., Eggeling, C. & Hell, S. W. Fluorescence nanoscopy by ground-state depletion and single-molecule return. *Nat. Methods* **5,** 943-945 (2008).
13. Heilemann, M., van de Linde, S., Mukherjee, A. & Sauer, M. Super-resolution imaging with small organic fluorophores. *Angew. Chem.-Int. Edit.* **48,** 6903-8 (2009).
14. van de Linde, S., Krstic, I., Prisner, T., Doose, S., Heilemann, M. & Sauer, M. Photoinduced formation of reversible dye radicals and their impact on super-resolution imaging. *Photochem Photobiol Sci* **10,** 499-506 (2011).
15. Dempsey, G. T., Vaughan, J. C., Chen, K. H., Bates, M. & Zhuang, X. Evaluation of fluorophores for optimal performance in localization-based super-resolution imaging. *Nat. Methods* **8,** 1027-1036 (2011).
16. Vogelsang, J., Steinhauer, C., Forthmann, C., Stein, I. H., Person-Skegro, B., Cordes, T. & Tinnefeld, P. Make them blink: probes for super-resolution microscopy. *ChemPhysChem* **11,** 2475-2490 (2010).
17. Chozinski, T. J., Gagnon, L. A. & Vaughan, J. C. Twinkle, twinkle little star: Photoswitchable fluorophores for super-resolution imaging. *FEBS Lett.* **588,** 3603-3612 (2014).
18. Li, H. L. & Vaughan, J. C. Switchable fluorophores for single-molecule localization microscopy. *Chem. Rev.* **118,** 9412-9454 (2018).
19. Jradi, F. M. & Lavis, L. D. Chemistry of photosensitive fluorophores for single-molecule localization microscopy. *ACS Chem. Biol.* **14,** 1077-1090 (2019).
20. Wang, L., Frei, M. S., Salim, A. & Johnsson, K. Small-molecule fluorescent probes for live-cell super-resolution microscopy. *J. Am. Chem. Soc.* **141,** 2770-2781 (2019).
21. Bossi, M., Folling, J., Belov, V. N., Boyarskiy, V. P., Medda, R., Egner, A., Eggeling, C., Schonle, A. & Hell, S. W. Multicolor far-field fluorescence nanoscopy through isolated detection of distinct molecular species. *Nano Lett.* **8,** 2463-2468 (2008).
22. Zhang, Z., Kenny, S. J., Hauser, M., Li, W. & Xu, K. Ultrahigh-throughput single-molecule spectroscopy and spectrally resolved super-resolution microscopy. *Nat. Methods* **12,** 935-938 (2015).
23. Tam, J., Cordier, G. A., Borbely, J. S., Alvarez, A. S. & Lakadamyali, M. Cross-talk-free multi-color STORM imaging using a single fluorophore. *PLoS One* **9,** e101772 (2014).
24. Xu, K., Zhong, G. S. & Zhuang, X. W. Actin, spectrin, and associated proteins form a periodic cytoskeletal structure in axons. *Science* **339,** 452-456 (2013).
25. Wojcik, M., Hauser, M., Li, W., Moon, S. & Xu, K. Graphene-enabled electron microscopy and correlated super-resolution microscopy of wet cells. *Nat. Commun.* **6,** 7384 (2015).
26. Zhang, M., Kenny, S. J., Ge, L., Xu, K. & Schekman, R. Translocation of interleukin-1β into a vesicle intermediate in autophagy-mediated secretion. *eLife* **4,** e11205 (2015).

27. Lehmann, M., Lichtner, G., Klenz, H. & Schmoranzer, J. Novel organic dyes for multicolor localization-based super-resolution microscopy. *J. Biophotonics* **9,** 161-170 (2016).
28. Slanina, T. & Oberschmid, T. Rhodamine 6G radical: a spectro (fluoro) electrochemical and transient spectroscopic study. *ChemCatChem* **10,** 4182-4190 (2018).
29. Huang, B., Wang, W., Bates, M. & Zhuang, X. Three-dimensional super-resolution imaging by stochastic optical reconstruction microscopy. *Science* **319,** 810-813 (2008).
30. Xu, K., Babcock, H. P. & Zhuang, X. Dual-objective STORM reveals three-dimensional filament organization in the actin cytoskeleton. *Nat. Methods* **9,** 185-188 (2012).
31. Grimm, J. B., Klein, T., Kopek, B. G., Shtengel, G., Hess, H. F., Sauer, M. & Lavis, L. D. Synthesis of a far-red photoactivatable silicon-containing rhodamine for super-resolution microscopy. *Angew. Chem.-Int. Edit.* **55,** 1723-1727 (2016).
32. Nanguneri, S., Flottmann, B., Herrmannsdorfer, F., Thomas, K. & Heilemann, M. Single-molecule super-resolution imaging by tryptophan-quenching-induced photoswitching of phalloidin-fluorophore conjugates. *Microsc. Res. Tech.* **77,** 510-516 (2014).
33. Wojcik, M., Hauser, M., Li, W., Moon, S. & Xu, K. Graphene-enabled electron microscopy and correlated super-resolution microscopy of wet cells. *Nat Commun* **6,** 7384 (2015).

Chapter 3: The Endoplasmic Reticulum Adopts Two Distinct Tubule Forms

The work in this chapter was conducted in collaboration with Bowen Wang, Zhiheng Zhao, Michael Xiong, Rui Yan, Ke Xu*. It is reproduced in part here from Wang et al[38] with permission from all co-authors. Copyright 2022 *PNAS.*

Introduction

Being the largest and most expansive organelle in the cell, the endoplasmic reticulum (ER) carries diverse key functions from protein and lipid synthesis, protein folding and modification, transport, calcium storage, to organelle interactions[1-6]. The shaping mechanism of this complex, membrane-bounded organelle is thus of fundamental significance[7-21].

The fully connected ER system is classically subdivided into three distinct domains, namely the nuclear envelope, ER sheets, and ER tubules. The latter two structures, collectively known as the peripheral ER, interweave into a dynamic, interconvertible network, yet are differently maintained and regulated by ER-shaping proteins. In mammalian cells, the two-dimensional ER sheets consist of two flat lipid bilayers at an ~50 nm separation[3,4,11]; this conserved luminal spacing is maintained by Climp63 (CKAP4), a transmembrane protein that forms intraluminal bridges between the opposing membranes via its extended coiled-coil domain[11,20]. Meanwhile, the highly curved edges of the ER sheets are stabilized by curvature-promoting proteins including the reticulons (Rtns) and REEPs[8,11], which, with their hairpin-like topology, insert into the outer leaflet of the lipid bilayer as wedges[9,10,12,21]. The same curvature-promoting proteins also stabilize the high curvatures in the one-dimensional ER tubules[9,10], which in mammalian cells are often taken as cylindrical tubules of ~50-100 nm diameter[2,7]. Notably, the intracellular overexpression of the reticulon Rtn4 (Nogo) substantially reduces the ER tubule diameter to ~20 nm, highlighting its ability to shape high-curvature tubules[10].

The rise of super-resolution microscopy (SRM) over the past decade offers new means to discover cellular structures[22-24]. When applied to the ER[14,17-19,25,26], new perspectives have emerged to challenge the traditional division between ER sheets and tubules, *e.g.*, whether the peripheral ER sheets should be viewed as a matrix of tubules or sheets with many nanoscale holes[17,19]. Here, we instead focus on the ER tubules, and, unexpectedly, suggest that a substantial fraction of the ER tubules should be recognized as thinned and elongated sheets of fixed widths defined by Climp63-Rtn interactions.

Results and Discussion

STORM unveils an ER-tubule dichotomy

We started by applying stochastic optical reconstruction microscopy (STORM) SRM[27,28], which routinely achieves ~20 nm spatial resolution, to immunolabeled endogenous Rtn4 in untransfected COS-7 cells. Rtn4 is one of the most studied ER-membrane curvature-promoting proteins in the mammalian cell, and quantitative proteomics of a human cell line has indicated it as the most abundant member of the group[29]. Similar results were obtained using two different antibodies (Fig.

7), and immunoblotting indicated that Rtn4b and Rtn4b2 were the dominant Rtn4 forms detected in our experiments (Fig. 8).

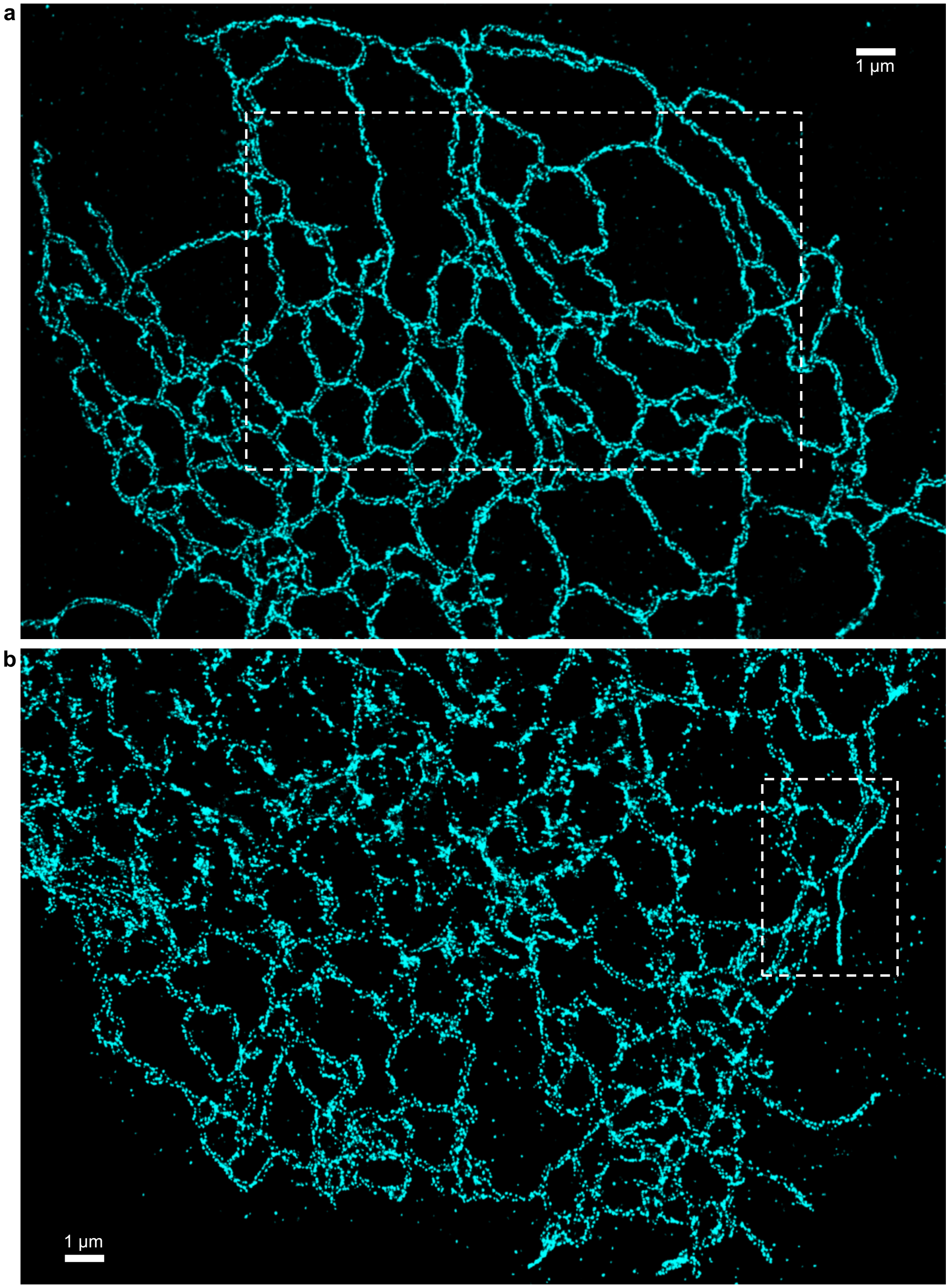

Figure 7 **Representative STORM results of the native COS-7 cell using two anti-Rtn4 antibodies.** (**a**) Cell immunolabeled with the sheep anti-Rtn4b antibody. (**b**) Cell immunolabeled with the rabbit anti-Rtn4a/b antibody. The boxed areas in (a,b) correspond to Fig. 1a and Fig. 1b, respectively.

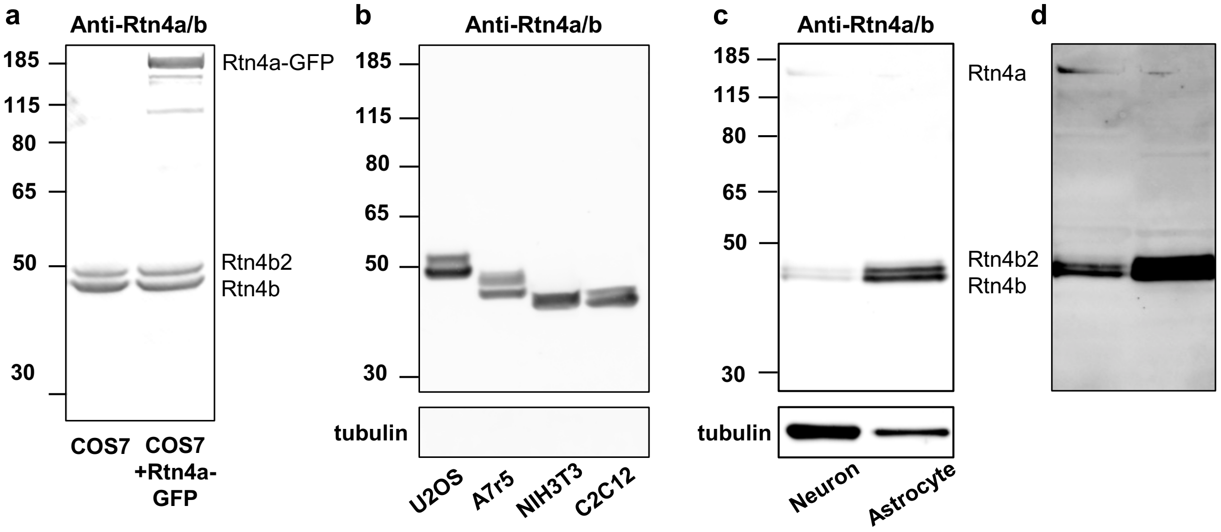

Figure 8 **Immunoblotting results.** (**a**) Immunoblotting with the rabbit anti-Rtn4a/b antibody for lysates of the native COS-7 cells (left lane) and COS-7 cells expressing Rtn4a-GFP (right lane). This showed that although the antibody also detects Rtn4a, the major forms in the native COS-7 cell are Rtn4b and Rtn4b2. (**b**) Immunoblotting with the same antibody, for lysates of untransfected U2OS, A7r5, NIH-3T3, and C2C12 cells, showing that Rtn4b and Rtn4b2 are the major forms. (**c**) Immunoblotting with the same antibody, for lysates of cultured primary neurons and astrocytes from the rat hippocampus. (**d**) Enhanced contrast for (c) to visualize the weak signal of Rtn4a, which is presumably present at the neuron plasma membrane.

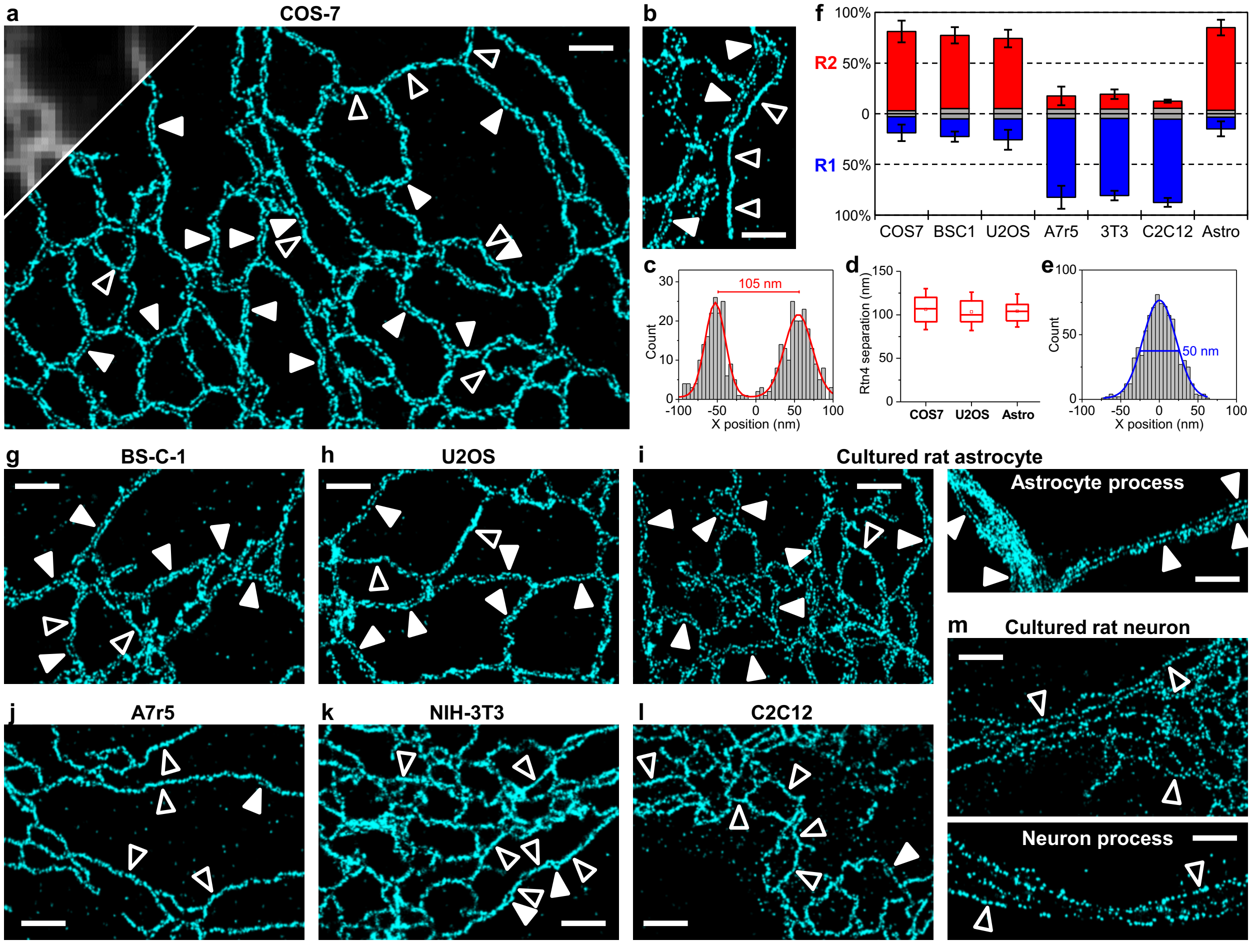

Figure 9 **STORM SRM of endogenous Rtn4 unveils a structural dichotomy for ER tubules.** (a) Representative STORM image of immunolabeled Rtn4 in the untransfected COS-7 cell, compared to diffraction-limited fluorescence image (upper-left corner). Filled and hollow arrowheads point to examples of R2 (Rtn double-line) and R1 (Rtn single-line) tubules, respectively. (b) Result from another COS-7 cell, highlighting a long R1 tubule at the extremity of the ER network. (c) Representative STORM image intensity (as single-molecule counts) across an R2 tubule. (d) Distribution of the STORM-determined center-to-center separations between opposing Rtn4 lines in the R2 tubules in the native COS-7 cells, U2OS cells, and cultured rat astrocytes. Whiskers and boxes show 10%, 25%, 50%, 75%, and 90% quantiles. For each data point, n = 200 local distances pooled from 5 cells. (e) Representative STORM image intensity across an R1 tubule. Blue curve: fit to a gaussian distribution of 50 nm FWHM. (f) The fractions of R1 and R2 tubules by length, observed in different cell types. Blue: R1; red: R2; gray: ambiguous. Error bars: standard deviations between n = 5 cells of each type. (g-m) Representative STORM images of the immunolabeled endogenous Rtn4 in different cell lines: BS-C-1 (monkey epithelial; g), U2OS (human epithelial; h), A7r5 (rat fibroblast; j), NIH-3T3 (mouse fibroblast; k), and C2C12 (mouse myoblast; l), as well as in cultured primary astrocytes (i) and neurons (m) from the rat hippocampus. Scale bars: 1 μm.

Unexpectedly, we found that in a major fraction of the ER tubules, Rtn4 showed up as two parallel lines over long ranges (filled arrowheads in Fig. 9ab). The typical center-to-center distance between the two lines was ~105 nm (Fig. 9c), and statistics showed a conserved narrow distribution of 106±18 nm between different cell types (Fig. 9d). This well-defined separation suggests a distinct structural arrangement and hence classification, which we hereby designate as R2 (Rtn double-line).

Meanwhile, we also observed a second class of ER tubules in which Rtn4 appeared as a thin single line (henceforth R1) of ~50 nm FWHM (full width at half maximum) (Fig. 9e). In COS-7 cells, they existed as short segments connecting the R2 tubules (hollow arrowheads in Fig. 7a), but also as longer tubules, often at the cell periphery, as the extremities of the ER network (hollow arrowheads in Fig. 9b). Together, ~75% and ~15% of the total ER tubule lengths in COS-7 cells were classified as the R2 and R1 forms, respectively, with the remaining ~10% being ambiguous (Fig. 9f). Thus, STORM unveiled an R1-R2 dichotomy of ER tubules, with R2 being the dominating form in COS-7 cells.

As we next examined seven other cell types, we found two epithelial cell lines, BS-C-1 (Fig. 9g) and U2OS (Fig. 9h), similarly exhibited an R2-dominant R1-R2 dichotomy (Fig. 9f). In contrast, two fibroblast cell lines (A7r5 and NIH-3T3; Fig. 7jk) and a myoblast cell line (C2C12; Fig. 7l) had >75% of the ER tubules in the R1 form and ~10% in the R2 form as sporadic, short segments (filled arrowheads in Fig. 9j-l). A drastic contrast was further noted between the cultured primary astrocytes and neurons from the rat hippocampus: whereas in the astrocytes the ER tubules were predominantly (~80%) R2, and this form was maintained along the thin, elongated processes (Fig. 9i), most ER tubules in the neurons appeared R1 (Fig. 9m).

Regulation of the R1-R2 dichotomy

Our unexpected observation of two distinct ER tubule forms begs structural explanations. For the R1 tubules, the STORM-measured ~50 nm apparent FWHM is comparable to that found (51 nm) for the ~25 nm-diameter microtubules under similar experimental conditions[28] given the antibody sizes and localization precisions. To simplify the discussion and consider the ~4 nm lipid-bilayer thickness, we take the outer, inner (luminal), and mean diameters of the R1 tubule as 24, 16, and 20 nm, respectively. These very small diameters and hence high membrane curvatures may be maintained by a consistent coverage of the curvature-promoting Rtn4 along the circumference. Indeed, as we overexpressed Rtn4b-GFP in COS-7 cells, STORM showed that accompanying the reduction of ER sheets and enhanced presence of ER tubules[9], most ER tubules turned into the ultrathin R1 form (Fig. 10bc and Fig. 11), in stark contrast to the ~75% R2 fraction in the untransfected cells (Fig. 9af). Nonetheless, sporadic R2 segments were occasionally spotted along the predominantly R1 tubules (filled arrowhead in Fig. 10c), and some cells retained more R2 tubules (Fig. 11), suggesting that the R1-R2 dichotomy is still the preferred configuration under Rtn4-overexpression.

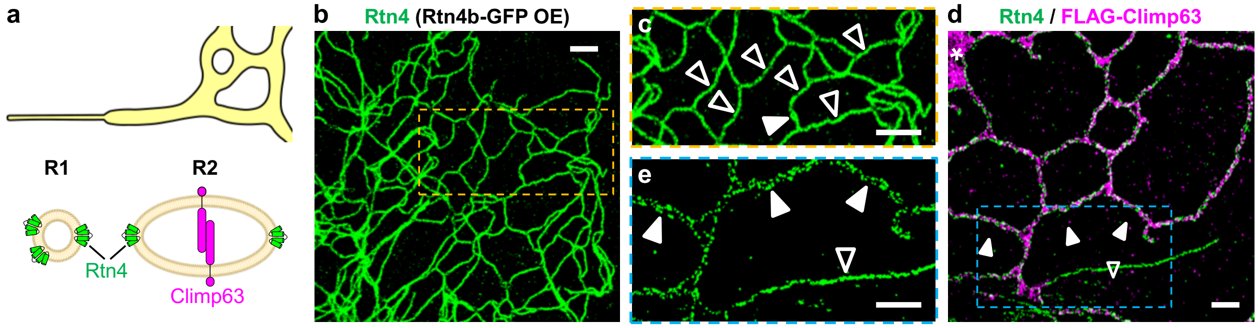

Figure 10 **Rtn4 and Climp63 co-regulate the R1-R2 dichotomy.** (**a**) Model: In the R1 tubules, high membrane curvatures are stabilized by a consistent Rtn4 coverage. In the R2 tubules, Rtn4 stabilizes the two highly curved edges of ribbon-like ER sheets, whereas Climp63 defines the luminal height. (**b**) Representative STORM image of immunolabeled Rtn4 in a COS-7 cell overexpressing Rtn4b-GFP. (**c**) Closeup of the box in (b). (**d**) Representative two-color STORM image of the immunolabeled endogenous Rtn4 (green) and overexpressed FLAG-Climp63 (magenta) in a COS-7 cell. Asterisk: ER sheet. (**e**) Closeup of the Rtn4 channel of the box in (d). Filled and hollow arrowheads point to examples of R2 and R1 tubules, respectively. Scale bars: 1 μm.

For the R2 tubules, the restriction of Rtn4 to two parallel lines raises a possibility that here Rtn4 stabilizes the edges of elongated, ribbon-like ER sheets (or compressed tubes) with two highly curved sides but relatively flat tops and bottoms (Fig. 10a). If that were the case, ER-sheet-maintaining proteins as Climp63 would likely regulate the luminal height of the R2 tubules as in typical ER sheets[11,20]. Indeed, fluorescence microscopy has shown the presence of Climp63 in ER tubules[11,17,18,30], and a recent SRM study discusses the possible roles of Climp63 in regulating luminal compartmentalization and heterogeneity as “nanodomains”[18]. Two-color STORM showed that whereas Climp63 and Rtn4 respectively filled the ER sheets and delineated the sheet edges (asterisks in Fig. 10d and Fig. 12), as expected, a relatable structural arrangement further extended into the R2 tubules (filled arrowheads in Fig. 10de). In contrast, the R1 tubules were devoid of Climp63 (hollow arrowheads in Fig. 10de). High-level overexpression of Climp63 led to the expansion of ER sheets (Fig. 12)[11], as well as an increased presence of R2 tubules in the otherwise R1-dominating NIH-3T3 cells (Fig. 12). Conversely, Climp63 siRNA markedly reduced R2 tubules in COS-7 cells (Fig. 13). Together, these results suggest Climp63 and Rtn4 co-regulate the R1-R2 dichotomy.

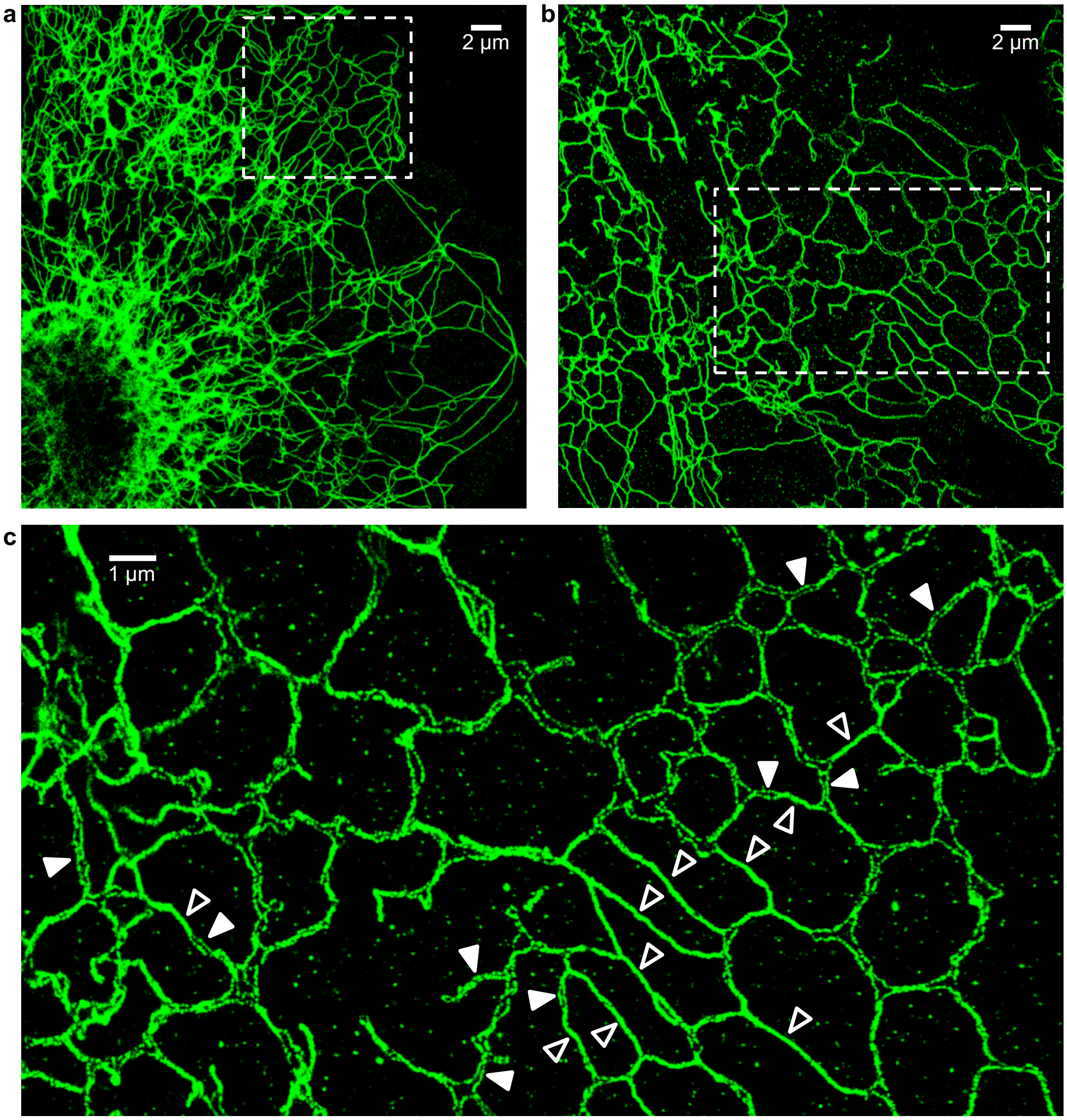

Figure 11.**Additional results on Rtn4 overexpression.** (**a**) STORM image of immunolabeled Rtn4 in a COS-7 cell overexpressing Rtn4b-GFP, showing the formation of extensive ER tubules in the R1 form. The boxed area corresponds to the magnified view in Fig. 10b. (**b,c**) The same conditions, but showing a cell that formed fewer ER tubules and retained more R2 tubules. (c) is a zoom-in of the box in (b). Filled and hollow arrowheads point to examples of R2 and R1 tubules, respectively.

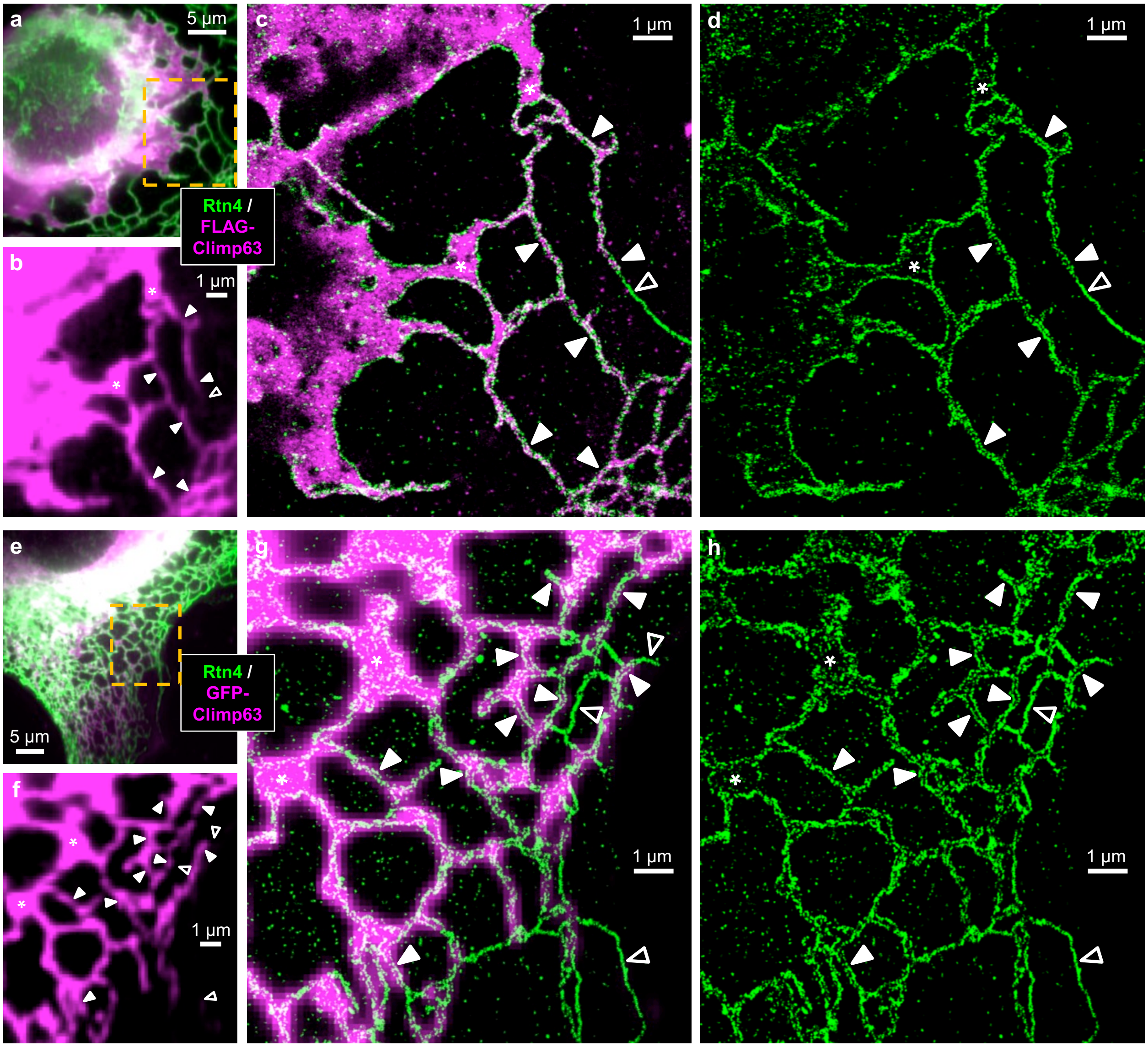

Figure 12 **Additional results on Climp63 overexpression in COS-7 and NIH-3T3 cells.** (**a-d**) A FLAG-Climp63-expressing COS-7 cell that exhibited notable expansion of ER sheets. (**a**) Two-color fluorescence image of immunolabeled Rtn4 (green) and FLAG-Climp63 (magenta). (**b**) Zoom-in of the FLAG-Climp63 channel for the boxed region in (a). (**c**) Two-color STORM image of the two channels for the same region. (**d**) The Rtn4 channel of (c). (**e-h**) An NIH-3T3 cell expressing GFP-Climp63. (**e**) Two-color fluorescence image of GFP-Climp63 (magenta) and immunolabeled Rtn4 (green). (**f**) Zoom-in of the GFP-Climp63 channel for the boxed region in (e). (**g**) The same region, overlaid with STORM image of Rtn4 (green). (**h**) The Rtn4 STORM channel of (g), showing abundant R2 tubules. Asterisks: ER sheets. Filled and hollow arrowheads point to examples of R2 and R1 tubules, respectively.

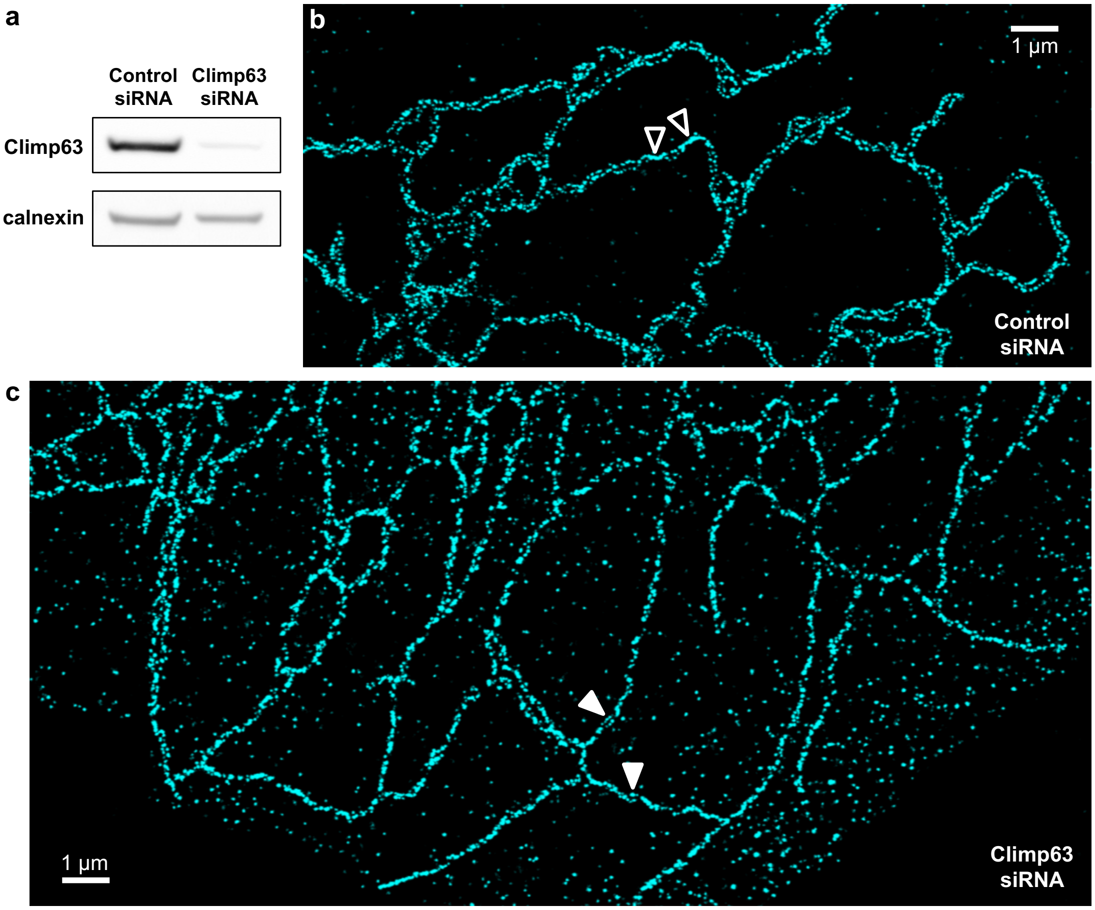

Figure 13 **Climp63 siRNA results.** (**a**) Immunoblot of Climp63 for lysates of COS-7 cells treated with control and Climp63 siRNA. Calnexin: loading control. (**b**) Representative STORM image of immunolabeled Rtn4 in a COS-7 cell treated with the control siRNA. Hollow arrowhead points to small R1 segments, whereas most other tubules in the view are R2. (**c**) Representative STORM image of immunolabeled Rtn4 in a COS-7 cell treated with the Climp63 siRNA. Filled arrowhead points to small R2 segments, whereas most other tubules in the view are R1.

Defining the R2 tubule width

To rationalize the remarkably conserved ~105 nm distance between the opposing Rtn4 lines in the R2 tubules, we consider a simple model in which Climp63 sets the R2 tubule height h to the typical lumen height of ER sheets (~50 nm)[11,20], whereas Rtn4 holds the membrane radii of curvature at the two edges at some preferred value of r_e. If the tubule adopts a smooth, elliptical cross-section, r_e may be inferred from the simple ellipse geometry as $r_e = h^2/2w$, where w ~100 nm is the ellipse width (~105 nm Rtn4-Rtn4 separation minus lipid-bilayer thickness). For h ~50 nm, r_e is thus estimated as ~12.5 nm, slightly larger than the assumed ~10 nm radius of curvature of the ultrathin R1 tubules above, yet slightly smaller than the ~15 nm value used in previous models for ER-sheet edges[11].

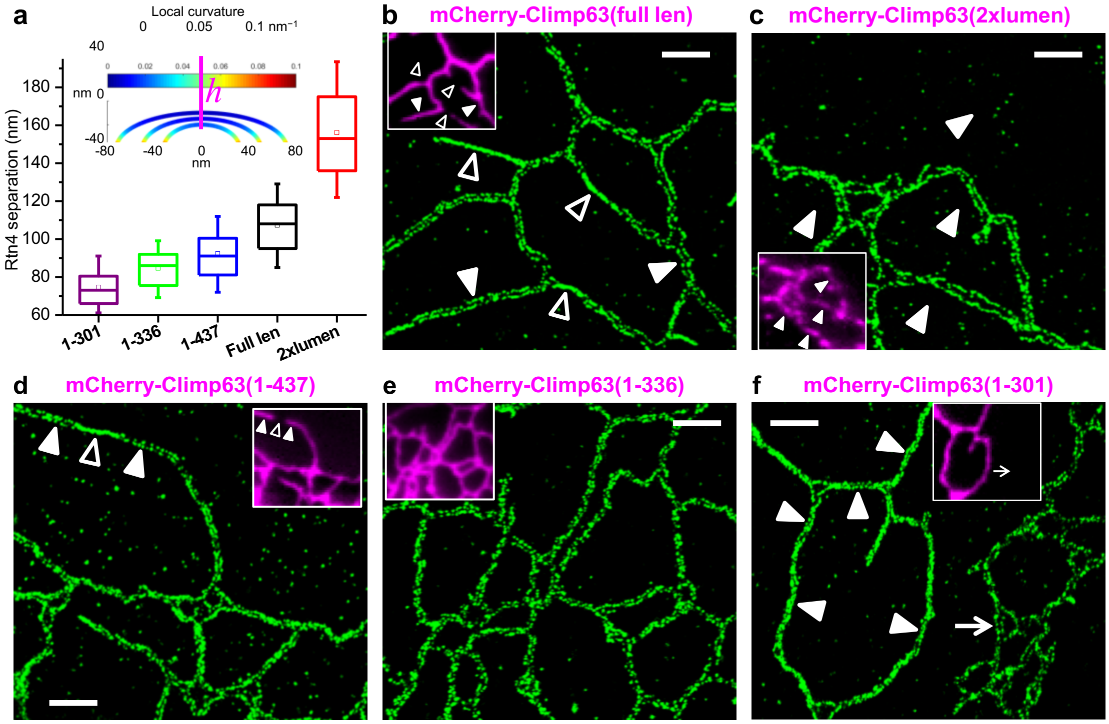

Figure 14**. Rtn4 and Climp63 jointly define the R2 tubule width.** (**a**) Distribution of center-to-center separations between opposing Rtn4 lines in R2 tubules, for COS-7 cells expressing mCherry-tagged Climp63 mutants of different intraluminal sizes. Whiskers and boxes show 10%, 25%, 50%, 75%, and 90% quantiles. For each data point, n = 200 local distances pooled from 5 cells. Inset: a simple model of the R2 tubule based on an elliptical cross section, in which the luminal height h is varied as the membrane curvature at the two edges is held at $1/r_e$ = 0.08 nm^{-1}. Color presents the local curvature. (**b-f**) Representative STORM images of the immunolabeled endogenous Rtn4 in COS-7 cells expressing mCherry-tagged full-length (1-575) (b), 2x lumen (c), 1-437 (d), 1-336 (e), and 1-301 (f) mutants of mouse Climp63. Insets: epifluorescence images of the mCherry channel. Filled and hollow arrowheads point to examples of R2 and R1 tubules, respectively. In (f), the arrow points to an untransfected cell in the same view, which facilitates a direct comparison. Scale bars: 1 μm.

Under the above simple model of fixed curvatures at the ribbon edges, the R2 tubule width $w \sim h^2/2r_e$ would correlate positively with the lumen height h (Fig. 14a inset). Recent experiments have shown that for ER sheets, h can be altered by varying the length of the intraluminal coiled-coil domain of Climp63[20]. We utilized this strategy and STORM-imaged Rtn4 in COS-7 cells expressing different mCherry-tagged Climp63 variants. Expression of the full-length mouse Climp63(1-575) reaffirmed the respective presence and absence of Climp63 in the R2 and R1 tubules (Fig. 14b), with the STORM-determined Rtn4-Rtn4 separation in the former unchanged (107±17 nm; Fig. 14a). In contrast, the expression of a mutant that doubled the intraluminal domain, Climp63(2xlumen), which may raise h to ~70 nm (ref [20]), substantially increased the Rtn4-Rtn4 separation in R2 tubules to ~155 nm (Fig. 14ac). Conversely, the expression of mutants with shortened intraluminal domains, Climp63(1-437), Climp63(1-336), and Climp63(1-301), led to progressive reductions of the Rtn4-Rtn4 separation (Fig. 14a,d-f), down to ~75 nm for the shortest version (Fig. 14af). Together, our results indicate that Climp63 and Rtn4 jointly define the R2 tubule width.

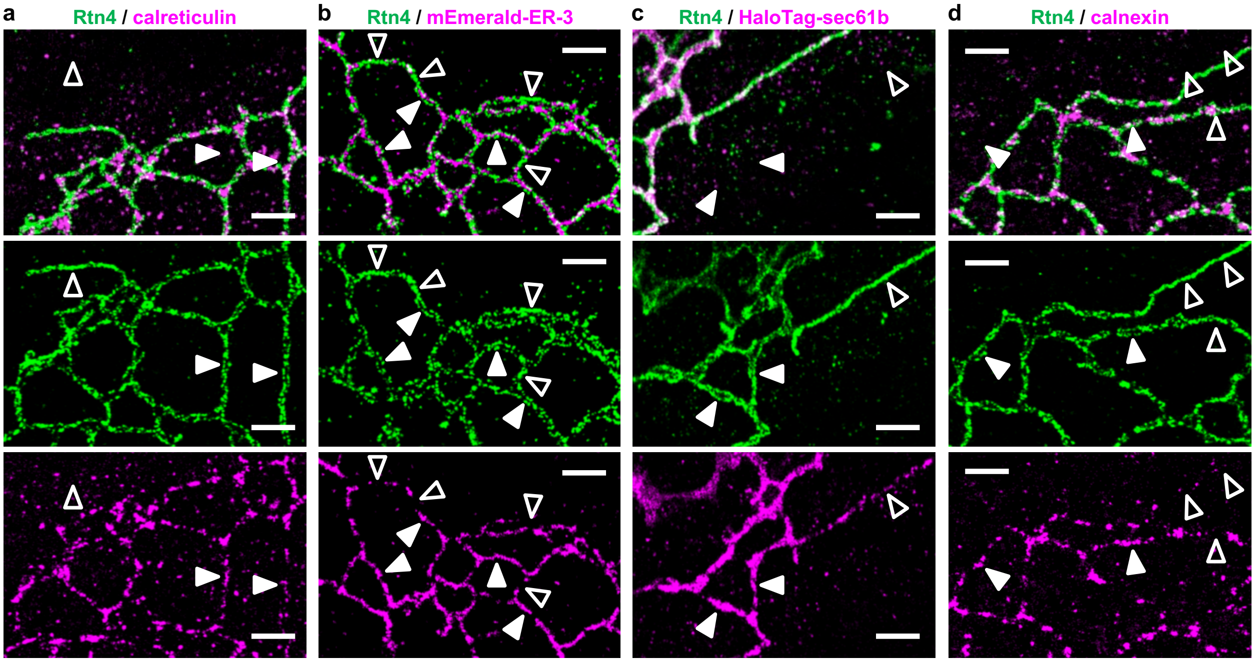

Figure 15. **R1 and R2 tubules differentially accommodate ER proteins.** (**a**) Representative two-color STORM image of the immunolabeled endogenous Rtn4 (green) and calreticulin (magenta) in an untransfected COS-7 cell. (**b**,**c**) Representative two-color STORM images of the immunolabeled endogenous Rtn4 (green) and expressed ER-luminal protein mEmerald-ER-3 [magenta in (b)] and ER-membrane protein HaloTag-sec61b [magenta in (c)] in COS-7 cells. (**d**) Representative two-color STORM image of the immunolabeled endogenous Rtn4 (green) and calnexin (magenta) in an untransfected COS-7 cell. Filled and hollow arrowheads point to examples of R2 and R1 tubules, respectively. Scale bars: 1 μm.

The R1 and R2 tubules differentially accommodate ER proteins

The above contrasting structures of R1 and R2 tubules may differentially regulate the distributions of ER proteins. With R1 tubules of ~16 nm luminal diameter and R2 tubules of elliptical width and height of ~100 and ~50 nm, the luminal cross-sectional areas of the two tubule types differ by ~20 folds. Further considering the protein exclusion volume, for a protein 5 nm in size, the accessible luminal volume per unit length is ~35-fold different between the two tubule types. Indeed, two-color STORM of immunolabeled Rtn4 versus the endogenous calreticulin (Fig. 15a) and the expressed ER-residing fluorescent protein (FP) mEmerald-ER-3 (Fig. 15b) showed that both ER-luminal proteins were abundant in the R2 tubules (filled arrowheads) but absent from the R1 tubules (hollow arrowheads). Our model also predicts a ~4-fold difference in the cross-sectional circumference, and hence the membrane surface area per unit length, between the R2 and R1 tubules. Accordingly, two-color STORM showed reduced, yet not eliminated, presence of overexpressed sec61b, a common ER-membrane marker, in the R1 tubules when compared to the R2 tubules (Fig. 15c). Interestingly, we next found that calnexin, an ER transmembrane protein with a large intraluminal domain[31], was largely excluded from the R1 tubules (Fig. 15d). To examine the role of the intraluminal domain, we expressed in COS-7 cells two constructs with the transmembrane domain of calnexin (canxTM) linked to the 27 kDa GFP mEmerald at the intraluminal and extraluminal (cytosolic) sides, respectively. Two-color STORM with Rtn4 showed that the former was more excluded from the R1 tubules than the latter (Fig. 16). Together, our results suggest that intraluminal crowding prevents both ER-luminal proteins and ER-membrane proteins with large intraluminal domains from entering the R1 tubules. The dynamics of this regulating mechanism is further examined below with live-cell experiments.

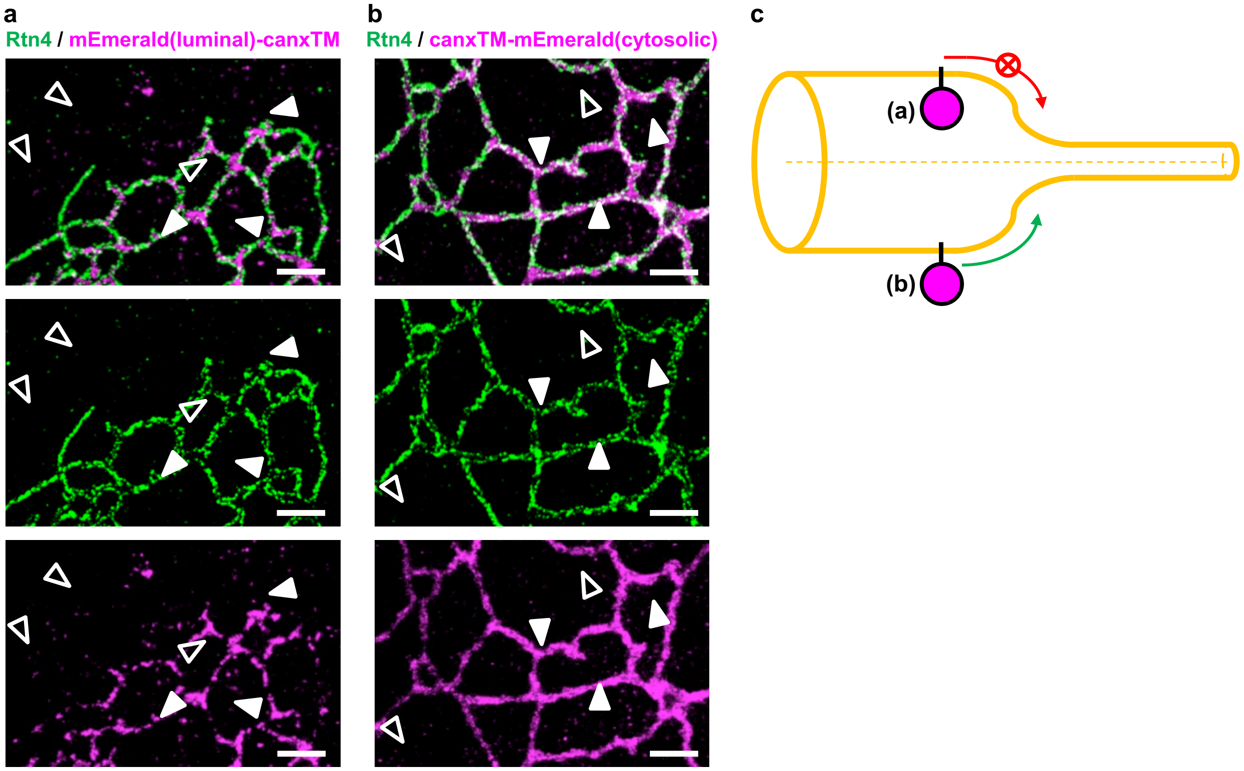

Figure 16 **R1 and R2 tubules differentially accommodate ER transmembrane proteins with and without large intraluminal domains.** (**a**,**b**) Representative two-color STORM images of the immunolabeled endogenous Rtn4 (green) and expressed calnexin transmembrane domain (canxTM) linked to mEmerald at the intraluminal (**a**) and extraluminal (cytosolic; **b**) sides, respectively, in COS-7 cells. Filled and hollow arrowheads point to examples of R2 and R1 tubules, respectively. Scale bars: 1 μm. (**c**) Model: Proteins with large intraluminal domains do not easily enter the ultrathin R1 tubule.

R1-R2 dynamics in live cells

To probe the R1-R2 tubule dynamics in live cells, we co-expressed Rtn4b-GFP and mCherry-Climp63 in COS-7 cells. Although the single overexpression of Rtn4 and Climp63 respectively biased ER tubules toward R1 and R2 (Fig. 10bc, 11, and 12), we reasoned that the co-expression of both proteins may counterbalance the two tubule forms. Previous work has noted normal ER morphologies in cells co-overexpressing Rtn4 and Climp63[11]. We observed a mixed population of both mCherry-Climp63-positive and -negative ER-tubule segments (filled and open arrowheads in Fig. 17a). Correlating the same view with STORM of immunolabeled Rtn4 (Fig. 17b and Fig. 18) showed that the two segment forms scrupulously corresponded to R2 and R1, respectively, consistent with our model above. Thus, by tracking in the wide-field micrographs which tubule segments were Climp63-positive, we followed the R1-R2 tubule dynamics in live cells at high temporal resolutions.

Both the R1 and R2 tubules were highly dynamic, with extensive restructuring constantly occurring at the second/sub-second time scales. For the fast-extending ER tubules, we found that the outgrowing tips were often in the Climp63-free R1 form (o1 in Fig. 17c). Climp63 then gradually extended into the tubules (e1 in Fig. 17c) to establish the R2 form, and interestingly, may do so in consecutive segments (e1-e3 in Fig. 17c).

A trove of intriguing R1-R2 dynamics was further observed in the tubule networks (Fig. 17de). Besides the above-noted extension of Climp63 into R1 tubules (e1-e4 in Fig. 17e), we often observed the splitting of Climp63-positive R2 tubules into multiple R2 segments connected by Climp63-free R1 segments (s1-s2 in Fig. 17e), the fusion between R2 segments (f1-f2 in Fig. 17e), the translational motion of R2 segments (t1-t2 in Fig. 17e), the entering of R2 segments into new branches (b1-b3 in Fig. 17e), and the quick withdrawn (w1-w2 in Fig. 17e) of newly extended tubules (o2 and o4).

Three-color live-cell imaging next showed that the ER-luminal protein HaloTag-ER-3 stayed exclusively in the R2 tubules (filled arrowheads in Fig. 17f) and so co-traveled with the Climp63-positive segments throughout the R1-R2 rearrangements (Fig. 17gh). In contrast, the ER-membrane protein mEmerald-sec61b exhibited reduced, yet still substantial, presence in the R1 tubules (hollow arrowheads in Fig. 17i), and this distribution was also preserved as the R1-R2 tubules dynamically rearranged in the cell (Fig. 17jk). Comparison with STORM results on fixed cells reaffirmed the above observations (Fig. 19). Thus, consistent with our two-color STORM results above (Fig. 15), the R1 tubules excluded ER-luminal proteins but accommodated low levels of ER-membrane proteins during the fast R1-R2 remodeling.

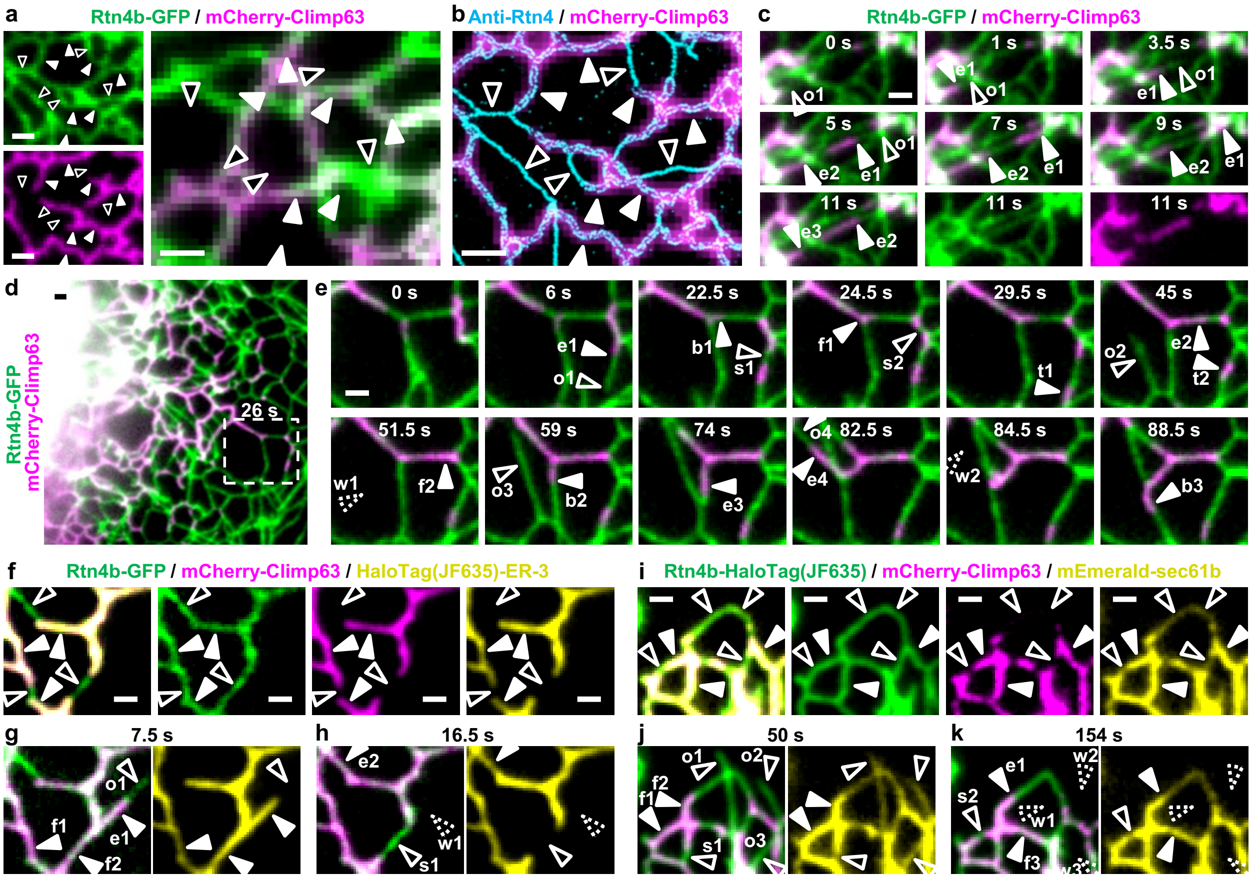

Figure 17 **Live-cell imaging unveils fast R1-R2 remodeling and associated co-traveling of ER proteins.** (**a**) Two-color fluorescence micrographs of Rtn4b-GFP (green) and mCherry-Climp63 (magenta) co-expressed in a COS-7 cell, shown as separate channels (left) and an overlay (right). (**b**) STORM of immunolabeled Rtn4 of the same view (cyan), overlayed with the mCherry-Climp63 micrograph (magenta). Filled and hollow arrowheads point to R2 and R1 examples, respectively. (**c**) Two-color micrographs of Rtn4b-GFP (green) and mCherry-Climp63 (magenta) for a small region in a living COS-7 cell at selected time points, highlighting ER-tubule outgrowth with a Climp63-free R1 tip (o1) and the ensuing extension of Climp63 into the tubule in segments (e1-e3). The two separated color channels are shown for the final image. See full series in Movie S1. (**d**) Another two-color live-cell dataset. (**e**) Selected time points for the boxed region. Arrowheads point to major structural changes vs. the preceding image. o1-o4: tubule outgrowths with Climp63-free R1 tips. e1-e4: extension of Climp63 into R1 tubules. s1-s2: the sequential splitting of a Climp63-positive R2 segment into three R2 segments connected by Climp63-negative R1 segments. f1-f2: fusion of an R2 tubule with two small R2 segments. t1-t2: translational motions of two R2 segments along tubules. b1-b3: Climp63 entering new tubule branches. w1-w2: withdrawal of newly extended tubules. See full series with separated color channels in Movies S3 and S4. (**f**) Live-cell three-color imaging of Rtn4b-GFP (green), mCherry-Climp63 (magenta), and JF635-labeled HaloTag-ER-3 (yellow) in a COS-7 cell, shown as merged and separated channels. (**g,h**) The same region after 7.5 s (g) and 16.5 s (h), shown as merged Rtn4b-GFP/mCherry-Climp63 (left) and HaloTag-ER-3 alone (right). See full series in Movie S5. (**i**) Live-cell three-color imaging of JF635-labeled Rtn4b-HaloTag (green), mCherry-Climp63 (magenta), and mEmerald-sec61b (yellow) in a COS-7 cell, shown as merged and separated channels. (**j,k**) The same region after 50 s (j) and 154 s (k), shown as merged Rtn4b-HaloTag/mCherry-Climp63 (left) and mEmerald-sec61b alone (right). See full series in Movie S6. Filled and hollow arrowheads in (f,i) point to R2 and R1 examples, respectively. Arrowheads in (g,h,j,k) point to major structural changes annotated similarly as (e). Scale bars: 1 µm.

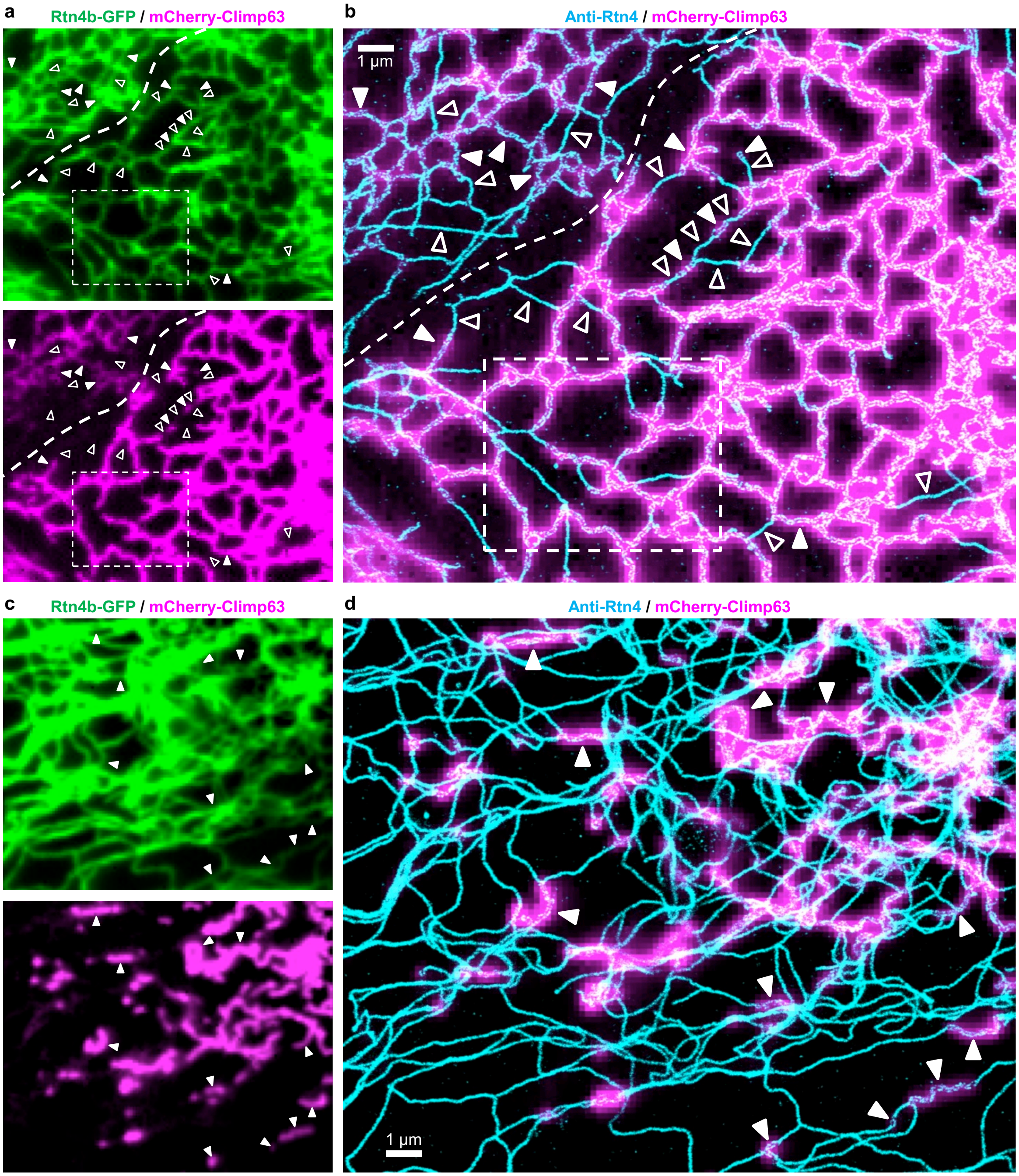

Figure 18 **Additional results confirming that the mCherry-Climp63-positive and -negative ER-tubule segments respectively correspond to the R2 and R1 forms.** (**a**) Diffraction-limited fluorescence micrographs of Rtn4b-GFP (top, green) and mCherry-Climp63 (bottom, magenta) in a co-expressing COS-7 cell. (**b**) STORM of immunolabeled Rtn4 of the same view (cyan), overlayed with the mCherry-Climp63 micrograph (magenta). The dotted curve demarcates the boundary between two cells expressing different levels of mCherry-Climp63. The boxed area corresponds to Fig. 5ab, with enhanced mCherry-Climp63 brightness to better visualize the lowly expressing cell in the upper-left corner. Both cells showed that the mCherry-Climp63-positive tubules were R2 (filled arrowheads) whereas the mCherry-Climp63-negative tubules were R1 (hollow arrowheads). (**c,d**) Results on another cell in which most ER tubules became R1, presumably due to the high expression level of Rtn4b-GFP. Nonetheless, the sporadic mCherry-Climp63-positive segments still correspond well to R2 (filled arrowheads).

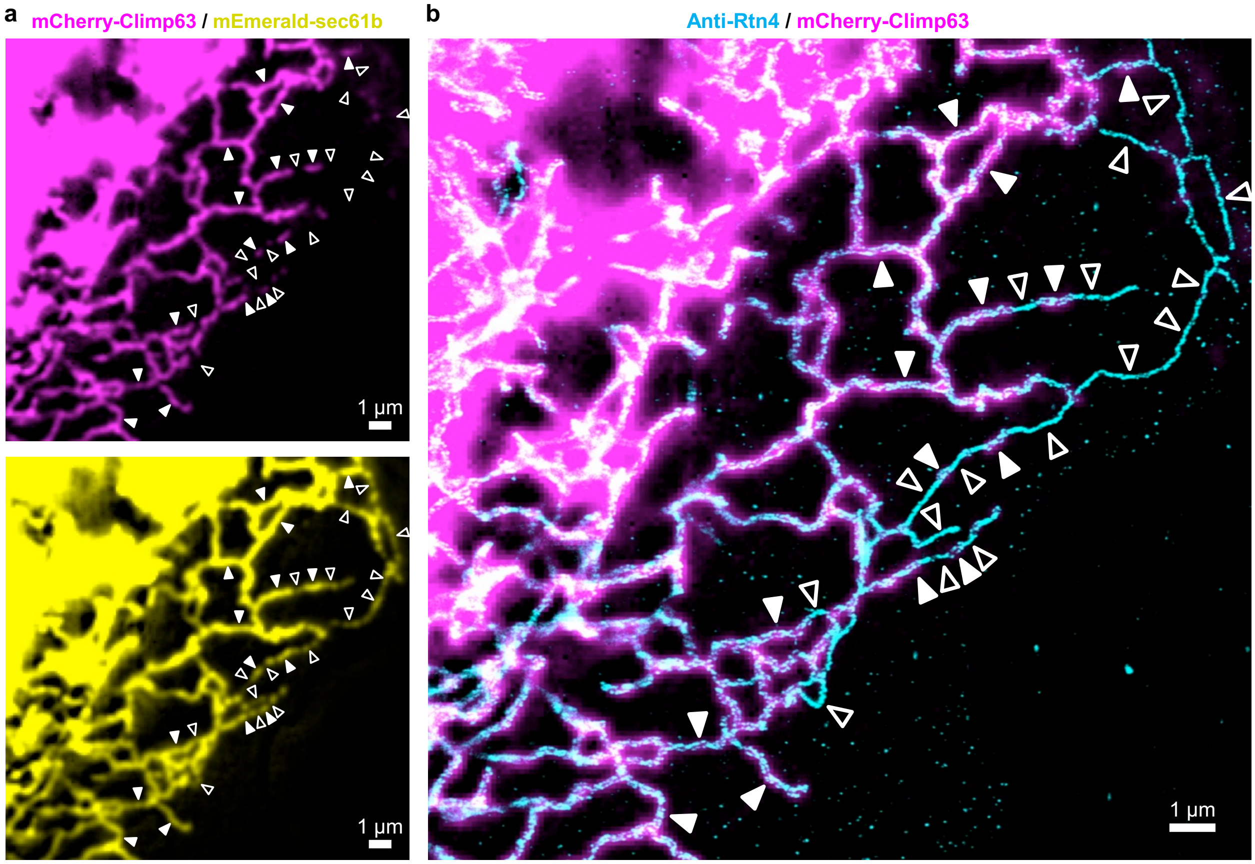

Figure 19 **STORM of a fixed COS-7 cell co-expressing mCherry-Climp63, mEmerald-sec61b, and Rtn4b-HaloTag.** (**a**) Diffraction-limited fluorescence micrographs of mCherry-Climp63 (top, magenta) and mEmerald-sec61b (bottom, yellow). (**b**) STORM of immunolabeled Rtn4 of the same view (cyan), overlayed with the mCherry-Climp63 micrograph (magenta). Filled and hollow arrowheads point to examples of R2 and R1 tubules, respectively.

The R1-R2 dichotomy also applies to other ER membrane curvature proteins

Our above results with the ubiquitously abundant Rtn4 prompt the question of whether other ER-membrane curvature-promoting proteins may behave similarly. To address this issue, we expressed in COS-7 cells mEmerald-tagged Rtn3c, REEP5 (DP1), and Arl6IP1. STORM showed that when overexpressed individually, the three Rtn4-like proteins consistently covered the ER tubules in the ultrathin R1 form, with short R2 segments only sporadically spotted (Fig. 20a). These results are similar to what we observed above with Rtn4 (Fig. 10bc and Fig. 11). When co-expressed with mCherry-Climp63, all three proteins displayed R1-R2 dichotomies, so that they showed up as two parallel lines for the Climp63-positive tubule segments (filled arrowheads in Fig. 20b) but remained in the R1 form for segments devoid of Climp63 (hollow arrowheads in Fig. 20b), again mimicking the behavior of Rtn4 (Fig. 17b). These observations suggest that the R1-R2 dichotomy is a general structural arrangement for ER tubules. Different curvature-preferring membrane proteins may thus work together to both promote/stabilize the ultrathin R1 tubules and cooperate with Climp63 to stabilize the two high-curvature edges of the ribbon-like R2 tubules.

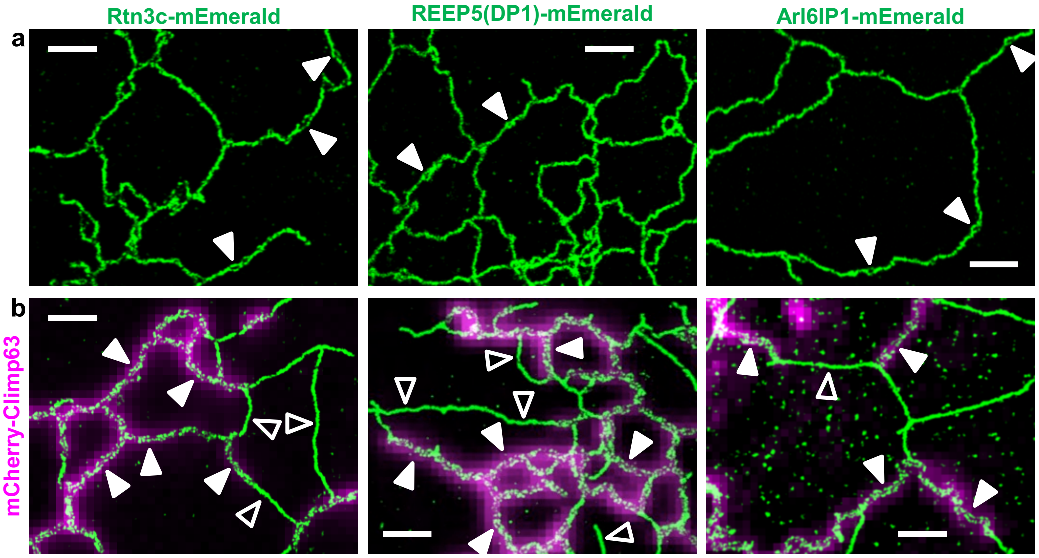

Figure 20 **The R1-R2 dichotomy also applies to other ER membrane curvature proteins.** (**a**) Representative STORM images of Rtn3c-mEmerald, REEP5(DP1)-mEmerald, and Arl6IP1-mEmerald expressed in COS-7 cells. Filled arrowhead points to small R2 segments, whereas most other tubules appear R1. (**b**) Representative STORM images of Rtn3c-mEmerald, REEP5(DP1)-mEmerald, and Arl6IP1-mEmerald (green) overlaid with epifluorescence images of mCherry-Climp63 (magenta) co-expressed in the same COS-7 cells. Filled and hollow arrowheads point to R2 and R1 examples, respectively. Scale bars: 1 µm.

Conclusion

Together, our super-resolution and live-cell microscopy results introduced an R1-R2 dichotomy for ER tubules and unveiled their dynamics and functional implications. Though our R1-R2 model is unexpected, it explains and connects several recent findings.

Live-cell STORM experiments with a membrane dye have noted that in BS-C-1 cells, the newly extended ER tubules are substantially thinner[25]. However, the origin of this phenomenon has not been elucidated. We showed that the extending "new" tubule tips were often of the thinner R1 form, yet the established "old" tubule networks were also characterized by dynamic R1-R2 rearrangements. Meanwhile, electron microscopy (EM) has visualized ~20 nm-sized "ultrathin" ER tubules in COS cells upon Rtn4-overexpression[10]. Fluorescence microscopy notes that the overexpression of Rtn4, Rtn3c, REEP5 (DP1), Arl6IP1, and like proteins tend to "squeeze out" luminal proteins from the ER tubules[10,12,32-34]. These observations may be understood under our R1-R2 framework as that raised levels of curvature-promoting proteins drive ER tubules into the luminal-protein-excluding R1 form. Yet, our results emphasized the coexistence and dichotomy of two well-defined tubule forms in both the native and overexpressed cells. rather than continuously evolving tubule widths. Interestingly, different cell types were dominated by either of the two tubule forms, and the R1 and R2 abundances varied as we altered the intracellular levels of Climp63 and Rtn4 (and analogs). Among these results, we found that the ER tubules in the rat primary astrocytes and neurons were predominately in the R2 and R1 forms, respectively. The latter finding echoes recent EM observations that the neuronal ER tubules are curiously thin at ~20 nm diameter[35].

Advances in electron tomography and FIB-SEM offer more holistic pictures of the ER structure. Examination of the resultant three-dimensional models identified ribbon-like tubules[13,16,17], including cases in which immunogold-labeled Rtn4 may have decorated the ribbon edges[16], potentially consistent with our R2 tubule model. However, immunogold yields sparse labeling and does not readily accommodate multi-target imaging, and EM generally offers limited fields of view. STORM readily resolved Rtn4 (and analogs) throughout the cell to establish the R1-R2 dichotomy, and its multicolor capabilities further facilitated mechanistic investigations. The observed good correspondence of the Climp63-positive and -negative tubules to the R2 and R1 forms thus enabled us to employ multicolor live-cell imaging to unveil the rich second/sub-second dynamics of the two tubule forms as they differently accommodated luminal and membrane proteins.

Our results underscore how the intricate interactions between ER-shaping proteins give rise to molecularly related, yet structurally and functionally distinct ER forms. Notably, in addition to identifying a conserved R2 tubule width across different cell types, we further established a positive correlation between this width and the Climp63 intraluminal size, thus emphasizing the co-regulation of both the R1-R2 dichotomy and the final tubule geometry by Climp63 and membrane curvature-promoting proteins. How the Climp63-Rtn4 (and analog) interplays highlighted here further cooperate with other ER-shaping proteins, as well as how the R1 and R2 tubules, with their contrasting accommodation of luminal and membrane proteins, respectively participate in the diverse ER functions, present pressing questions for future experimental and theoretical efforts.

Materials and methods

Plasmids. FLAG-Climp63, GFP-Climp63, GFP-Rtn3c(mouse), and HA-REEP5(mouse) were gifts from Tom Rapoport[10,11]. Rtn4a-GFP (Addgene plasmid #61807) and mCherry-Climp63(mouse) (Addgene plasmid #136293) were gifts from Gia Voeltz[36]. mEmerald-sec61b (Addgene plasmid #54249), mEmerald-ER-3 (Addgene plasmid #54082), and calnexin-mEmerlad (Addgene plasmid #54021) were gifts from Michael Davidson. pcDNA3.1(+) backbone was prepared by digesting the pcDNA3.1(+) IRES GFP plasmid (Addgene plasmid #51406; a gift from Kathleen Collins) using the restriction enzymes EcoRI (ThermoFisher, FD0274) and XbaI (ThermoFisher, FD0684). Rtn4b-GFP was generated by inserting two PCR-amplified fragments from the initial part (RTN4 AA1-AA185) and the later part (RTN4 AA1005-AA1192 plus AcGFP1) of Rtn4a-GFP into the pcDNA3.1(+) backbone using Gibson Assembly (New England Biolabs, #E2611S). Rtn4b-HaloTag was generated by inserting PCR-amplified Rtn4b from Rtn4b-GFP and PCR-amplified HaloTag from pSEMS-Tom20-HaloTag (Addgene plasmid #111135; a gift from Karin Busch) into the pcDNA3.1(+) backbone using Gibson Assembly. mCherry-Climp63(2xlumen) was prepared by assembling the full-length mCherry-Climp63(mouse) with the luminal part of mouse Climp63 (AA110-AA575). The two fragments were both PCR amplified from mCherry-Climp63(mouse) and assembled by Gibson Assembly onto the pcDNA3.1(+) backbone. The codons for the first 5 amino acid of the second luminal domain was changed from ctGgaGgaGgtCcaG to ctAgaAgaAgtAcaA, which did not alter the encoded amino acids (LEEVQ). mCherry-Climp63(1-301), mCherry-Climp63(1-336), and mCherry-Climp63(1-437) were generated by inserting the PCR-amplified corresponding front parts of mCherry-Climp63(mouse) into the pcDNA3.1(+) backbone using Gibson Assembly. HaloTag-sec61b was prepared by inserting PCR-amplified HaloTag from pSEMS-Tom20-HaloTag and sec61b fragment from mEmerald-sec61b into the pcDNA3.1(+) backbone using Gibson Assembly. HaloTag-ER-3 was generated by inserting PCR-amplified calreticulin signal peptide plus the 3AA linker from mEmerald-ER-3 and HaloTag from pSEMS-Tom20-HaloTag, plus a C-terminus KDEL ER retention signal included in the primer during the PCR amplification, into the pcDNA3.1(+) backbone. mEmerald(luminal)-canxTM was prepared by inserting the PCR-amplified calreticulin signal peptide, 3AA linker, and mEmerald from mEmerald-ER-3 and the PCR-amplified calnexin transmembrane domain plus cytosolic residues (canxTM, AA482-AA592 from human calnexin) from calnexin-mEmerald into the pcDNA3.1(+) backbone using Gibson Assembly. canxTM-mEmerald(cytosolic) was generated by inserting the PCR-amplified calnexin signal peptide plus a 7AA linker from mEmerald-calnexin and the later part of calnexin-mEmerald (canxTM-14AA linker-mEmerald) into the pcDNA3.1 backbone using Gibson Assembly. Rtn3c-mEmerald, REEP5-mEmerald, and Arl6IP1-mEmerald were generated by inserting PCR-amplified Rtn3c from GFP-Rtn3c(mouse), REEP5 from HA-REEP5(mouse), and Arl6IP1 from Myc-DDK-Arl6IP1 (OriGene #RC201681), respectively, and mEmerald from mEmerald-ER-3 into the pcDNA3.1(+) backbone using Gibson Assembly. Protein-coding sequences were verified by Sanger sequencing at the UC-Berkeley DNA Sequencing Facility.

Antibodies. Primary antibodies used: rabbit polyclonal anti-Rtn4a/b (ThermoFisher, PA1-41220), sheep polyclonal anti-Rtn4b (R&D Systems, AF6034), rabbit polyclonal anti-calreticulin (Abcam, ab2907), rabbit polyclonal anti-calnexin (ProteinTech, 10427-2-AP), rabbit monoclonal anti-sec61b (Cell Signaling Technology, 14648S), mouse monoclonal anti-α-tubulin (Sigma, T6199, DM1A), mouse monoclonal anti-Climp63 (Enzo Life Sciences, ENZ-ABS669-0100, G1/296), mouse monoclonal anti-FLAG (Sigma-Aldrich, F1804, M2), mouse monoclonal anti-GFP (ThermoFisher, A11120), rabbit polyclonal anti-GFP (ThermoFisher, A11122), and Alexa Fluor 647-conjugated rabbit polyclonal anti-GFP (ThermoFisher, A31852). For both single-color and two-color STORM, Alexa Fluor 647-conjugated secondary antibodies (Invitrogen, goat anti-rabbit IgG, A21245; donkey anti-sheep IgG, A21448) were used to label the target for imaging under 647 nm excitation. For two-color STORM, the second target was labeled by a secondary antibody (Jackson ImmunoResearch) conjugated with CF568 succinimidyl ester (Biotium, 92131) for imaging under 560 nm excitation.

Cell culture and transfection. COS-7, BSC-1, U2OS, A7r5, NIH-3T3, and C2C12 cells (UC-Berkeley Cell Culture Facility) were maintained in Dulbecco's Modified Eagle Media (DMEM) supplemented with 10% fetal bovine serum (FBS) at 37 ˚C with 5% CO_2. Cells were cultured on #1.5 coverslips for 2~3 days until reaching ~70% confluency. Rat astrocytes and neurons from the E18 hippocampus (BrainBits) were plated on poly-D-lysine-coated #1.5 coverslips. Astrocytes were cultured in the NbAstro medium (BrainBits). Neurons were cultured in the NbActiv1 medium (BrainBits) for ~14 days. Plasmid transfection was performed using Lipofectamine 3000 (Invitrogen, L3000-008) according to the manufacturer's specifications, using ~0.5-1 µg per well in 24-well plates (Corning, CLS3527) or Lab Teck II chambered coverglass. Transfected cells were incubated for 1-2 days before subsequent experiments. Silencer Select siRNA against Climp63 (ThermoFisher, 4392420-s21594) and scrambled Silencer Select control siRNA (GUACCAAUUCGUAAGUGUUTT; AACACUUACGAAUUGGUACTT) were transfected using Lipofectamine RNAiMAX (ThermoFisher, 13778100) according to the manufacturer's specifications. About 50 pmol siRNA was transfected into each well in 6-well plates. The siRNA-transfected cells were cultured for 3 days before subsequent experiments.

Immunoblotting. Suspensions of cultured cells were centrifuged at 4,200 rpm, resuspended, and washed with Dulbecco's Phosphate-Buffered Saline (DPBS) twice before lysis. Cells were then lysed in a lysis buffer (150 mM NaCl, 50 mM Tris, 5 mM EDTA, 1% Triton-X, pH=7.5) at 4 ˚C for 30 min. Neurons were directly lysed in the cell culture flask with the lysis buffer and then transferred to a microcentrifuge tube. Cell lysates were centrifuged for 20 min at 12,000 rpm. The supernatant was aspirated, and Halt Protease Inhibitor (ThermoFisher, 1862209) was added. Protein concentration was determined using Pierce Rapid BCA Protein Assay Kit (ThermoFisher, A53226). 1x lithium dodecyl sulfate (LDS) loading buffer (ThermoFisher, NP0007) and 70 mM dithiothreitol were added to 20-30 µg protein sample. The sample was then incubated at 75 ˚C for 15 min. Electrophoresis was performed on NuPAGE 4-12% or 10% Bis-Tris Gel (Invitrogen, NP0302BOX and NP0315BOX) in 1x MOPS SDS running buffer (Invitrogen, NP0001) for ~2 h at 90 V. Sample was then transferred to a methanol-activated polyvinylidene difluoride (PVDF) membrane (ThermoFisher, 22860) in the transfer buffer at 18 V for 50 min. The transfer buffer was prepared as 25 mM Tris base (Acros Organics, 42457-1000), 192 mM glycine (Sigma-Aldrich, G8898), and 10% v/v methanol in water. The PVDF membrane was blocked with 5% bovine serum albumin (BSA) in TBST (20 mM Tris, 150 mM NaCl, 0.1% Tween 20, pH~7.5) for 30min at room temperature (RT). The membrane was incubated with diluted primary antibodies (1:1000, rabbit polyclonal anti-Rtn4a/b; 1:2000 mouse anti-alpha tubulin) in 5% BSA in TBST at 4 ˚C overnight and then washed three times with TBST buffer. The membrane was then incubated with the corresponding Alexa Fluor 647-conjugated secondary antibody or Alexa Fluor 555-conjugated anti-mouse IgG1 secondary antibody (Sigma-Aldrich, SAB4600301-50UL) at RT for 1 hour followed by 3 additional wash with TBST buffer. The membrane was then imaged with a GE Typhoon FLA 9500 Variable Mode Laser Scanner Image Analyzer.

Immunofluorescence. Cells were fixed with 3% (v/v) paraformaldehyde (Electron Microscopy Sciences, #15714) and 0.1% (v/v) glutaraldehyde (Electron Microscopy Sciences, #16365) in DPBS at RT for 20 min, and then washed twice with a freshly prepared 0.1% (w/w) $NaBH_4$ solution followed by three additional washes with DPBS. Samples were then blocked and permeabilized using a DPBS-based blocking buffer containing 0.1% (w/w) saponin (Sigma-Aldrich, S4521) and 5% (v/v) donkey serum (Jackson ImmunoResearch, 017000121) for sheep antibodies or 3% (w/w) BSA (Sigma-Aldrich, A3059) for other antibodies, for 30 min at RT. Samples were next incubated with diluted primary antibodies (1:200, sheep anti-Rtn4b; 1:100, rabbit anti-Rtn4a/b; 1:100, rabbit anti-calreticulin; 1:100, rabbit anti-calnexin; 1:100, rabbit anti-sec61b; 1:200, mouse anti-FLAG; 1:400, mouse anti-GFP; 1:200, rabbit anti-GFP) in the blocking buffer overnight at 4 ˚C. Samples were washed three times with washing buffer (0.1x blocking buffer diluted with DPBS) after primary labeling. Samples were then incubated with diluted dye-labeled secondary antibodies (1:400 for commercial antibodies, 1:50 for homemade antibodies) in the blocking buffer for 30 min at RT, followed by three additional washes with the washing buffer.

STORM super-resolution microscopy. STORM imaging was performed on a homebuilt inverted microscope using a Nikon CFI Plan Apo λ 100x oil-immersion objective (NA = 1.45), as described previously[37,38]. The dye-labeled samples were mounted with a Tris-HCl-based imaging buffer containing 5% (w/v) glucose, 100 mM cysteamine (Sigma-Aldrich, 30070), 0.8 mg/mL glucose oxidase (Sigma-Aldrich, G2133), and 40 µg/mL catalase (Sigma-Aldrich, C30). Diffraction-limited wide-field images were first sequentially recorded for the different color channels using weak (~50 mW/cm^2) laser excitations at 647 nm (for Alexa Fluor 647), 560 nm (for mCherry and

CF568), and 488 nm (for GFP) using matching bandpass filters. For STORM imaging of targets labeled by Alexa Fluor 647 and CF568, the sample was sequentially imaged using strong 647-nm and 560-nm lasers at ~2 kW/cm^2. The angle of incidence was slightly smaller than the critical angle of total internal reflection, thus illuminating a few micrometers into the sample. A weak (0-1 W/cm^2) 405-nm laser was applied to assist photo-switching. The resulting stochastic photo-switching of single-molecule fluorescence was recorded using an Andor iXon Ultra 897 EM-CCD camera at 110 frames per second (fps), for a total of ~80,000 frames per image. The raw STORM data were analyzed according to previously described methods[27,28,39].

Live-cell fluorescence microscopy. Cells were plated in Lab-Tek II chambered coverglass and transfected as described above. For imaging of HaloTag-labeled targets, 0.25 μM of JF635 HaloTag ligand (a gift from Luke Lavis) was added to the cell culture medium for 30 min and then rinsed off with the imaging medium. The imaging medium was DMEM containing HEPES (ThermoFisher, 21063029). Live-cell fluorescence microscopy was performed on a Nikon Eclipse Ti-E inverted fluorescence microscope using a CFI Plan Apo λ 100x oil-immersion objective (NA=1.45) with the additional 1.5x magnification on the microscope body. A multi-bandpass filter cube (Semrock Di01-R405/488/561/635 as the dichroic mirror and Chroma ZET405/488/561/640m as the emission filter) was used. Two-color imaging of GFP and mCherry was achieved by alternating the excitation laser between 488 and 560 nm in successive frames as an Andor iXon Ultra 897 EM-CCD camera recorded at 4 fps, hence an effective time resolution of 0.5 s for two-color wide-field images. Three-color imaging of GFP, mCherry, and JF635 was achieved by alternating the excitation laser between 488 nm, 560 nm, and 647 nm in successive frames at camera framerates of 4 or 3 fps, hence effective time resolutions of 0.75 s or 1 s for three-color wide-field images.

Acknowledgements

We acknowledge support by the National Institute Of General Medical Sciences of the National Institutes of Health (DP2GM132681), the Packard Fellowships for Science and Engineering, and the Pew Charitable Trusts, to K.X. K.X. is a Chan Zuckerberg Biohub investigator.

References

1. English, A. R. & Voeltz, G. K. Endoplasmic reticulum structure and interconnections with other organelles. *Cold Spring Harb. Perspect. Biol.* **5,** a013227 (2013).
2. Goyal, U. & Blackstone, C. Untangling the web: mechanisms underlying ER network formation. *Biochim. Biophys. Acta* **1833,** 2492-2498 (2013).
3. Westrate, L. M., Lee, J. E., Prinz, W. A. & Voeltz, G. K. Form follows function: the importance of endoplasmic reticulum shape. *Annu. Rev. Biochem.* **84,** 791-811 (2015).
4. Schwarz, D. S. & Blower, M. D. The endoplasmic reticulum: structure, function and response to cellular signaling. *Cell Mol. Life Sci.* **73,** 79-94 (2016).
5. Zhang, H. & Hu, J. Shaping the endoplasmic reticulum into a social network. *Trends Cell Biol.* **26,** 934-943 (2016).
6. Wu, H., Carvalho, P. & Voeltz, G. K. Here, there, and everywhere: The importance of ER membrane contact sites. *Science* **361,** eaan5835 (2018).
7. Shibata, Y., Voeltz, G. K. & Rapoport, T. A. Rough sheets and smooth tubules. *Cell* **126,** 435-439 (2006).

8. Shibata, Y., Hu, J., Kozlov, M. M. & Rapoport, T. A. Mechanisms shaping the membranes of cellular organelles. *Annu. Rev. Cell Dev. Biol.* **25,** 329-354 (2009).
9. Voeltz, G. K., Prinz, W. A., Shibata, Y., Rist, J. M. & Rapoport, T. A. A class of membrane proteins shaping the tubular endoplasmic reticulum. *Cell* **124,** 573-586 (2006).
10. Hu, J. J., Shibata, Y., Voss, C., Shemesh, T., Li, Z. L., Coughlin, M., Kozlov, M. M., Rapoport, T. A. & Prinz, W. A. Membrane proteins of the endoplasmic reticulum induce high-curvature tubules. *Science* **319,** 1247-1250 (2008).
11. Shibata, Y., Shemesh, T., Prinz, W. A., Palazzo, A. F., Kozlov, M. M. & Rapoport, T. A. Mechanisms determining the morphology of the peripheral ER. *Cell* **143,** 774-788 (2010).
12. Zurek, N., Sparks, L. & Voeltz, G. Reticulon short hairpin transmembrane domains are used to shape ER tubules. *Traffic* **12,** 28-41 (2011).
13. Puhka, M., Joensuu, M., Vihinen, H., Belevich, I. & Jokitalo, E. Progressive sheet-to-tubule transformation is a general mechanism for endoplasmic reticulum partitioning in dividing mammalian cells. *Mol. Biol. Cell* **23,** 2424-2432 (2012).
14. Shemesh, T., Klemm, R. W., Romano, F. B., Wang, S. Y., Vaughan, J., Zhuang, X. W., Tukachinsky, H., Kozlov, M. M. & Rapoport, T. A. A model for the generation and interconversion of ER morphologies. *Proc. Natl. Acad. Sci. U. S. A.* **111,** E5243-E5251 (2014).
15. Wang, S., Tukachinsky, H., Romano, F. B. & Rapoport, T. A. Cooperation of the ER-shaping proteins atlastin, lunapark, and reticulons to generate a tubular membrane network. *eLife* **5,** e18605 (2016).
16. Ramo, O., Kumar, D., Gucciardo, E., Joensuu, M., Saarekas, M., Vihinen, H., Belevich, I., Smolander, O. P., Qian, K., Auvinen, P. & Jokitalo, E. NOGO-A/RTN4A and NOGO-B/RTN4B are simultaneously expressed in epithelial, fibroblast and neuronal cells and maintain ER morphology. *Sci. Rep.* **6,** 35969 (2016).
17. Nixon-Abell, J., Obara, C. J., Weigel, A. V., Li, D., Legant, W. R., Xu, C. S., Pasolli, H. A., Harvey, K., Hess, H. F., Betzig, E., Blackstone, C. & Lippincott-Schwartz, J. Increased spatiotemporal resolution reveals highly dynamic dense tubular matrices in the peripheral ER. *Science* **354,** aaf3928 (2016).
18. Gao, G., Zhu, C., Liu, E. & Nabi, I. R. Reticulon and CLIMP-63 regulate nanodomain organization of peripheral ER tubules. *PLoS Biol.* **17,** e3000355 (2019).
19. Schroeder, L. K., Barentine, A. E. S., Merta, H., Schweighofer, S., Zhang, Y., Baddeley, D., Bewersdorf, J. & Bahmanyar, S. Dynamic nanoscale morphology of the ER surveyed by STED microscopy. *J. Cell Biol.* **218,** 83-96 (2019).
20. Shen, B., Zheng, P., Qian, N., Chen, Q., Zhou, X., Hu, J., Chen, J. & Teng, J. Calumenin-1 interacts with climp63 to cooperatively determine the luminal width and distribution of endoplasmic reticulum sheets. *iScience* **22,** 70-80 (2019).
21. Wang, N., Clark, L. D., Gao, Y., Kozlov, M. M., Shemesh, T. & Rapoport, T. A. Mechanism of membrane-curvature generation by ER-tubule shaping proteins. *Nat. Commun.* **12,** 568 (2021).
22. Xu, K., Zhong, G. & Zhuang, X. Actin, spectrin, and associated proteins form a periodic cytoskeletal structure in axons. *Science* **339,** 452-456 (2013).
23. Sahl, S. J., Hell, S. W. & Jakobs, S. Fluorescence nanoscopy in cell biology. *Nat. Rev. Mol. Cell Biol.* **18,** 685-701 (2017).

24. Sigal, Y. M., Zhou, R. & Zhuang, X. Visualizing and discovering cellular structures with super-resolution microscopy. *Science* **361,** 880-887 (2018).
25. Shim, S. H., Xia, C., Zhong, G., Babcock, H. P., Vaughan, J. C., Huang, B., Wang, X., Xu, C., Bi, G. Q. & Zhuang, X. Super-resolution fluorescence imaging of organelles in live cells with photoswitchable membrane probes. *Proc. Natl. Acad. Sci. U. S. A.* **109,** 13978-13983 (2012).
26. Bottanelli, F., Kromann, E. B., Allgeyer, E. S., Erdmann, R. S., Wood Baguley, S., Sirinakis, G., Schepartz, A., Baddeley, D., Toomre, D. K., Rothman, J. E. & Bewersdorf, J. Two-colour live-cell nanoscale imaging of intracellular targets. *Nat. Commun.* **7,** 10778 (2016).
27. Rust, M. J., Bates, M. & Zhuang, X. Sub-diffraction-limit imaging by stochastic optical reconstruction microscopy (STORM). *Nat. Methods* **3,** 793-795 (2006).
28. Bates, M., Huang, B., Dempsey, G. T. & Zhuang, X. W. Multicolor super-resolution imaging with photo-switchable fluorescent probes. *Science* **317,** 1749-1753 (2007).
29. Beck, M., Schmidt, A., Malmstroem, J., Claassen, M., Ori, A., Szymborska, A., Herzog, F., Rinner, O., Ellenberg, J. & Aebersold, R. The quantitative proteome of a human cell line. *Mol. Syst. Biol.* **7,** 549 (2011).
30. Schweizer, A., Rohrer, J., Slot, J. W., Geuze, H. J. & Kornfeld, S. Reassessment of the subcellular localization of p63. *J. Cell Sci.* **108,** 2477-2485 (1995).
31. Schrag, J. D., Bergeron, J. J. M., Li, Y., Borisova, S., Hahn, M., Thomas, D. Y. & Cygler, M. The structure of calnexin, an ER chaperone involved in quality control of protein folding. *Mol. Cell* **8,** 633-644 (2001).
32. Tolley, N., Sparkes, I. A., Hunter, P. R., Craddock, C. P., Nuttall, J., Roberts, L. M., Hawes, C., Pedrazzini, E. & Frigerio, L. Overexpression of a plant reticulon remodels the lumen of the cortical endoplasmic reticulum but does not perturb protein transport. *Traffic* **9,** 94-102 (2008).
33. Yang, Y. S., Harel, N. Y. & Strittmatter, S. M. Reticulon-4A (Nogo-A) redistributes protein disulfide isomerase to protect mice from SOD1-dependent amyotrophic lateral sclerosis. *J. Neurosci.* **29,** 13850-13859 (2009).
34. Yamamoto, Y., Yoshida, A., Miyazaki, N., Iwasaki, K. & Sakisaka, T. Arl6IP1 has the ability to shape the mammalian ER membrane in a reticulon-like fashion. *Biochem. J.* **458,** 69-79 (2014).
35. Terasaki, M. Axonal endoplasmic reticulum is very narrow. *J. Cell Sci.* **131,** jcs210450 (2018).
36. Shibata, Y., Voss, C., Rist, J. M., Hu, J., Rapoport, T. A., Prinz, W. A. & Voeltz, G. K. The reticulon and DP1/Yop1p proteins form immobile oligomers in the tubular endoplasmic reticulum. *J. Biol. Chem.* **283,** 18892-18904 (2008).
37. Wojcik, M., Hauser, M., Li, W., Moon, S. & Xu, K. Graphene-enabled electron microscopy and correlated super-resolution microscopy of wet cells. *Nat Commun* **6,** 7384 (2015).
38. Zhang, M., Kenny, S. J., Ge, L., Xu, K. & Schekman, R. Translocation of interleukin-1β into a vesicle intermediate in autophagy-mediated secretion. *eLife* **4,** e11205 (2015).
39. Huang, B., Wang, W., Bates, M. & Zhuang, X. Three-dimensional super-resolution imaging by stochastic optical reconstruction microscopy. *Science* **319,** 810-813 (2008).

Chapter 4: Branched Actin Networks are Organized for Asymmetric Force Production During Clathrin-Mediated Endocytosis in Mammalian Cells

The work in this chapter was conducted in collaboration with Meiyan Jin[1*], Cyna Shirazinejad[1*], Bowen Wang, Amy Yan[1], Johannes Schöneberg, Srigokul Upadhyayula, Ke Xu, David G. Drubin[1#]. It is reproduced in part here from Jin et al. with permission from all co-authors. Copyright 2022 *Nat. Comm.*.

Introduction

Actin filament assembly facilitates vesicle formation in several trafficking pathways including clathrin-mediated endocytosis (CME)[1,2]. However, how actin assembly forces are harnessed has not been fully revealed for any vesicle forming process. In this study, live-cell imaging of triple-genome-edited, induced pluripotent stem cells (iPSCs), and newly developed machine-learning-based computational analysis tools, were used to comprehensively analyze assembly dynamics and geometry of proteins representing three different CME functional modules. When hundreds of CME events with and without associated Arp2/3-dependent actin network assembly were compared, sites with actin assembly showed a distinct delay between completion of endocytic coat assembly and vesicle scission, consistent with the notion that these were stalled sites requiring actin assembly forces to complete vesicle formation. Importantly, our analysis showed that N-WASP is preferentially recruited to one side of CME sites, where it stimulates actin assembly asymmetrically. These results indicate that in mammalian cells actin assembly is induced at stalled CME sites, where asymmetric forces pull the plasma membrane into the cell much like a bottle opener pulls off a bottle cap.

Formation of clathrin-coated vesicles requires forces to first bend the membrane into a sphere or tube, and to then break the thin neck that connects the vesicle to the plasma membrane. These forces are generated through the combined actions of proteins that directly bend the membrane and actin filament assembly[3–5] (Fig. 1a). A detailed understanding of how actin forces are harnessed to aid vesicle formation and scission, and whether and how actin assembly might mediate an adaptive response to the opposing forces such as membrane tension and turgor pressure, depends on understanding where filament assembly occurs around the endocytic membrane and when. In yeast cells, where turgor pressure is particularly high, super-resolution data suggest that actin assembles symmetrically around CME sites and indicate that actin regulators including Las17, yeast WASP, is present in a ring surrounding the base of the clathrin coat[6]. However, studies on mammalian cells raised the possibility that actin assembly may at least in some cases be initiated asymmetrically at clathrin coats[7–9]. Which CME sites assemble actin, and how actin networks are organized with respect to CME sites, has not been determined systematically, in a large-scale, unbiased manner, particularly in live mammalian cells. This information is essential to understanding how and why actin assembly forces are harnessed for CME.

Result and Discussion

To investigate the physiological roles and spatiotemporal regulation of actin assembly at CME sites in mammalian cells, we applied genome-editing techniques to generate a human iPSC line (hereafter referred to as ADA cells) that co-expresses a TagRFP-T fusion of the mu1 subunit of the AP2 adaptor complex (AP2M1), a TagGFP2 fusion of dynamin2 (DNM2), and a HaloTag fusion of the ARPC3 subunit of the Arp2/3 complex as representatives of the CME coat, scission and actin modules respectively[3,10,11] (Fig. 21a, 22ab). Our previous studies showed that endogenously tagged AP2M1, DNM2 and ARPC3 can serve as reliable markers of these CME functional modules that avoid disruption of physiological spatiotemporal organization of the process as might be caused by overexpression of fluorescently labeled proteins[12–15]. We observed dynamic CME events on the basal plasma membrane of the genome-edited cells using Total Internal Reflection Fluorescence (TIRF) microscopy (Fig. 22b). Consistent with previous studies, AP2 is recruited at early CME stages while DNM2 is recruited in two phases[10,12,13,16]. At the early stage of CME, a relatively small amount of DNM2 is recruited to CME sites. Shortly before the end of a CME event, the DNM2 recruitment rate increases rapidly with DNM2 levels reaching a peak concomitant with vesicle scission[10] (Fig. 22b). This later rapid-recruitment phase represents the assembly of dynamin helix on the highly curved neck of the budding vesicle after the U to Ω shape transition of the endocytic membrane[17–21].

We analyzed how actin networks are organized at CME sites in both fixed and live cells. First, we performed two-color 3D Stochastic Optical Reconstruction Microscopy (STORM) imaging on fixed ADA cells, localizing either AF647 phalloidin-labeled actin filaments or HaloTag-fused ARPC3 at CME sites. Due to the dense phalloidin labelling of cortical actin filaments under plasma membrane, it was often challenging to unambiguously identify the CME-specific actin structures in iPSCs. However, in regions with thinner cortical actin layers, we observed that actin was typically distributed asymmetrically around CME sites (Fig. 21b and Fig. 22c). Antibody labeling of ARPC3-Halotag in the ADA cells had the advantage of a less complex staining pattern. Besides being highly concentrated in lamellipodia, ARPC3 was associated with CME sites asymmetrically, like the actin (Fig 21c and Fig 22d). These data indicate that ARPC3 can be used to study Arp2/3-mediated actin assembly at CME sites as a more specific maker of branched actin networks than a general actin label.

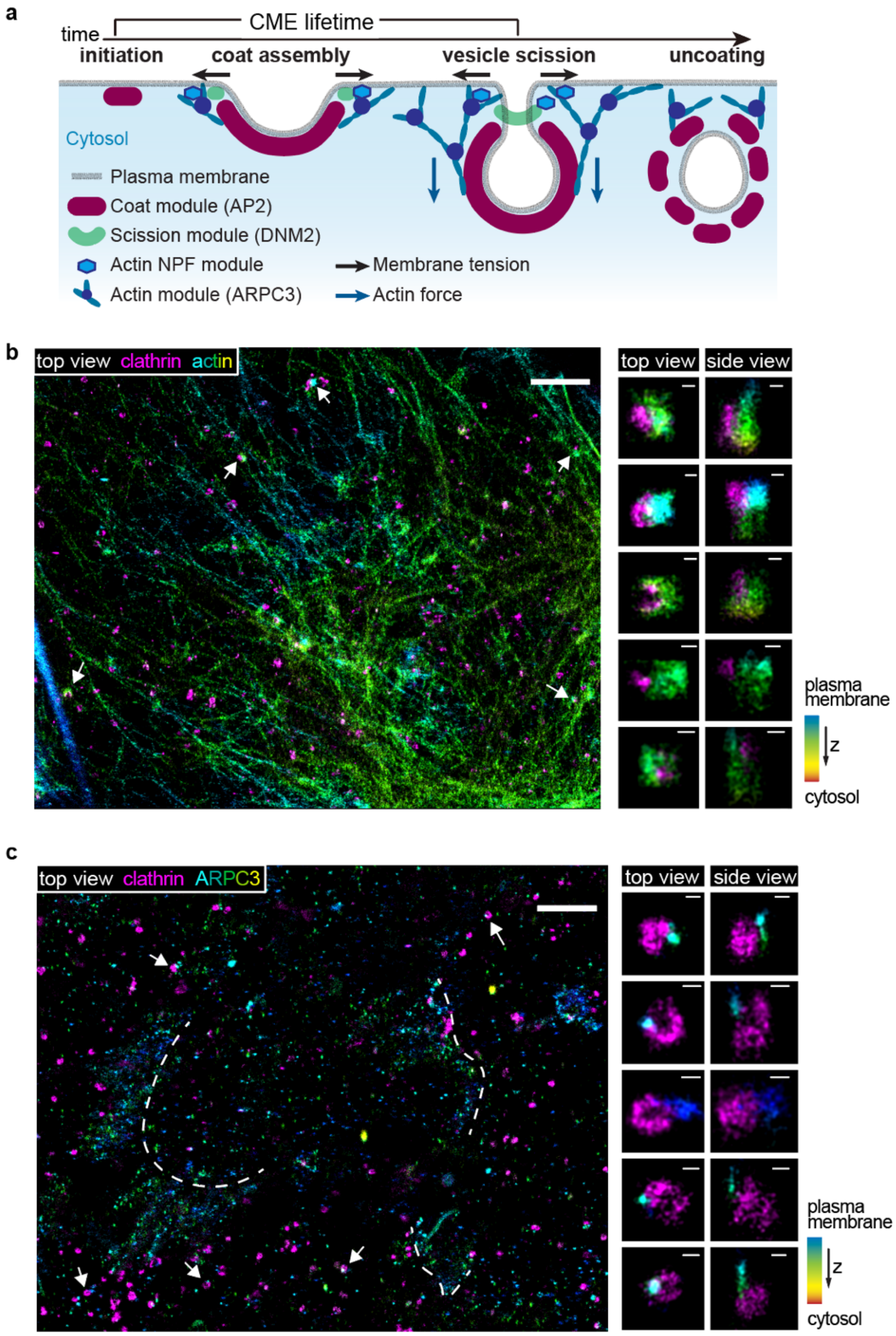

Figure 21 **Two-color, 3D stochastic optical reconstruction microscopy (STORM) shows that actin structures are off-centered with respect to clathrin coats. a,** Schematic model of CME. Mammalian CME proteins can be grouped into several modules, including the coat, WASP and Myosin / actin nucleation promoting factor (NPF), actin and scission modules[5]. Actin networks provide pulling forces to invaginate the membrane against membrane tension[5,15,23]. **b,** Two-color 3D STORM image of bottom membrane of ADA cells immunolabeled with clathrin light chain antibody (clathrin, CF-680, magenta) and phalloidin (actin, AF647, rainbow). **c,** Two color 3D STORM image of bottom membrane of ADA cells immunolabeled with clathrin light chain antibody (clathrin, AF647, magenta) and HaloTag antibody (ARPC3-HaloTag, CF-680, rainbow). Dotted lines label lamellipodia. **b, c,** The highlighted CME sites are labeled by white arrows and are shown in magnified top view and side view projections. Color bar shows the z position of ARPC3-HaloTag. Scale bars: 2μm, 100nm.

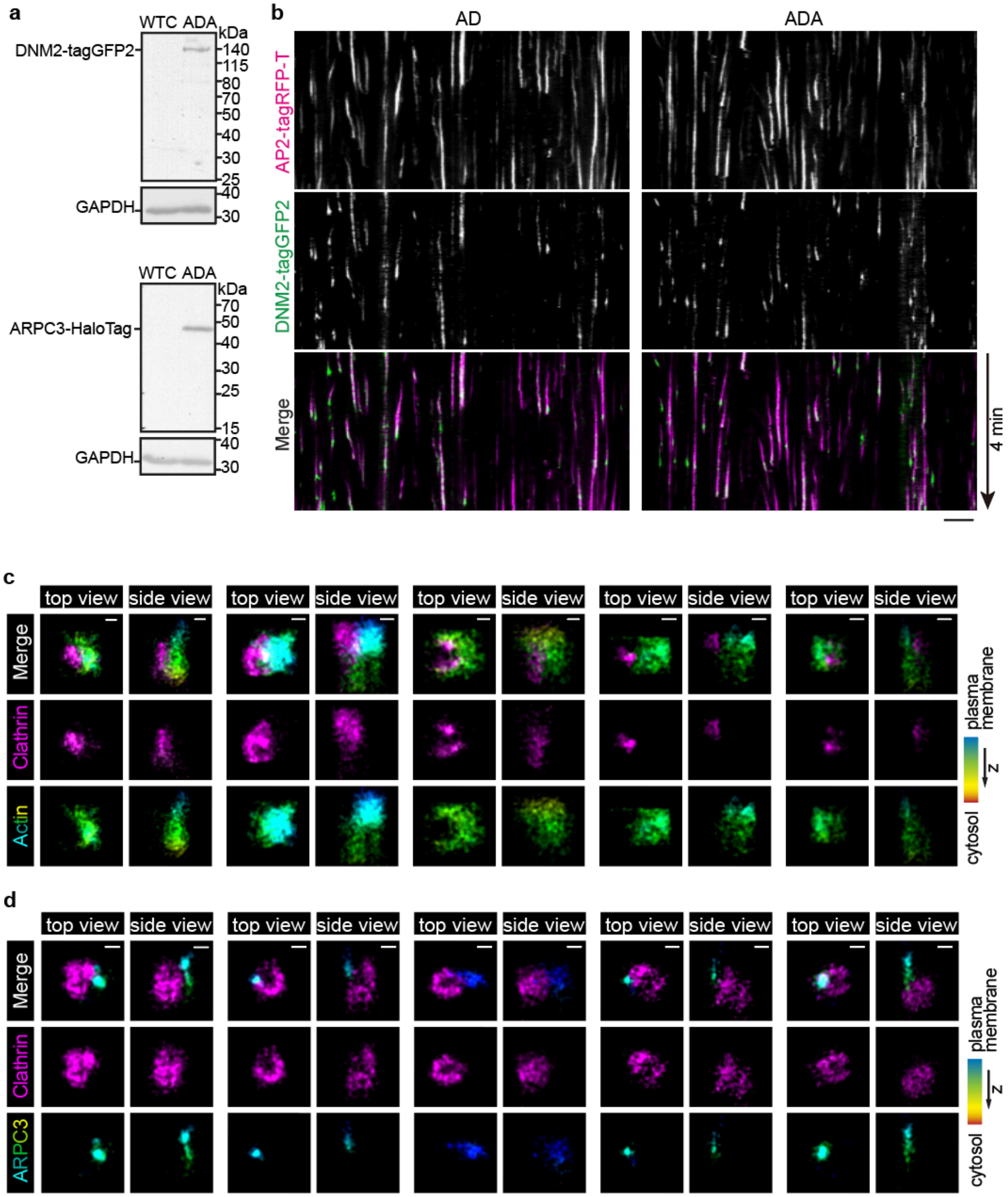

Figure 22 **Two-color, 3D stochastic optical reconstruction microscopy (STORM) shows asymmetric actin structures adjacent to the clathrin coats. a,** Immunoblot analysis of cell extracts from the WT (WTC) and genome-edited (AP2M1-tagRFP-T/DNM2-tagGFP2/ARPC3-HaloTag; ADA) human iPSCs. The labeled proteins were detected with tag(CGY)FP, HaloTag, and GAPDH (loading control) antisera respectively. **b,** Kymograph of representative CME sites of double-edited (AP2M1-tagRFP-T/DNM2-tagGFP2; AD) and triple-edited (AP2M1-tagRFP-T/DNM2-tagGFP2/ARPC3-HaloTag; ADA) cells. The cells showed dynamic CME sites. **c,** Two-color 3D STORM of clathrin light chain (magenta) and actin (rainbow) for the highlighted CME sites from Fig. 1b. Scale bar: 100 nm. **d,** Two color 3D STORM of clathrin light chain (magenta) and ARPC3-HaloTag (rainbow) of highlighted CME sites from Fig. 1c. Scale bars: 100 nm.

We next used ADA cells to investigate actin assembly at CME sites in live cells, which has several advantages over studies in fixed cells. During the fixation and subsequent sample preparation, actin structures may not be faithfully preserved. In addition, in fixed cells it is very difficult to identify the stage of the CME, so the timing, geometry and dynamics of actin assembly cannot be related to the endocytic stage. More importantly, only by using live cells is it possible to trace a single CME event from start to finish, and to therefore identify those CME events wherein no detectable actin is ever assembled to compare key parameters between events with and without associated actin assembly.

By visualizing endogenously tagged AP2M1 to mark the initiation of CME, and DNM2 to mark scission, together with ARPC3 to specifically label Arp2/3-nucleated, branched actin filaments (Fig. 21a and 24b), we were able to precisely study the spatial and temporal regulation of actin assembly during CME. Using TIRF live-cell imaging, we observed ARPC3-labeled branched actin networks at lamellipodia and a subpopulation of CME sites (Fig. 23a, b). Dynamic actin assembly and disassembly occurred at CME sites with different spatio-temporal characteristics, including discrete CME sites, clathrin plaques and at clathrin coat splitting sites, as previously reported[7] (Fig. 23c and 24a, b). In the analysis described below, we focus on the discrete CME events and not the more complex ones (plaques and splitting events). Quantitative analysis of these events with 1s/frame temporal resolution revealed that ARPC3 is mainly recruited during the late stages of CME with similar timing to the rapid recruitment stage of DNM2[15] (Fig. 23b, c). Interestingly, we observed clear spatial displacement between ARPC3 (actin module) and AP2 (coat module) before and after vesicle scission (Fig. 23c). Imaging fluorescent beads using the same settings indicates that the displacement is not an artifact caused by misalignment between different imaging channels (Fig. 22c).

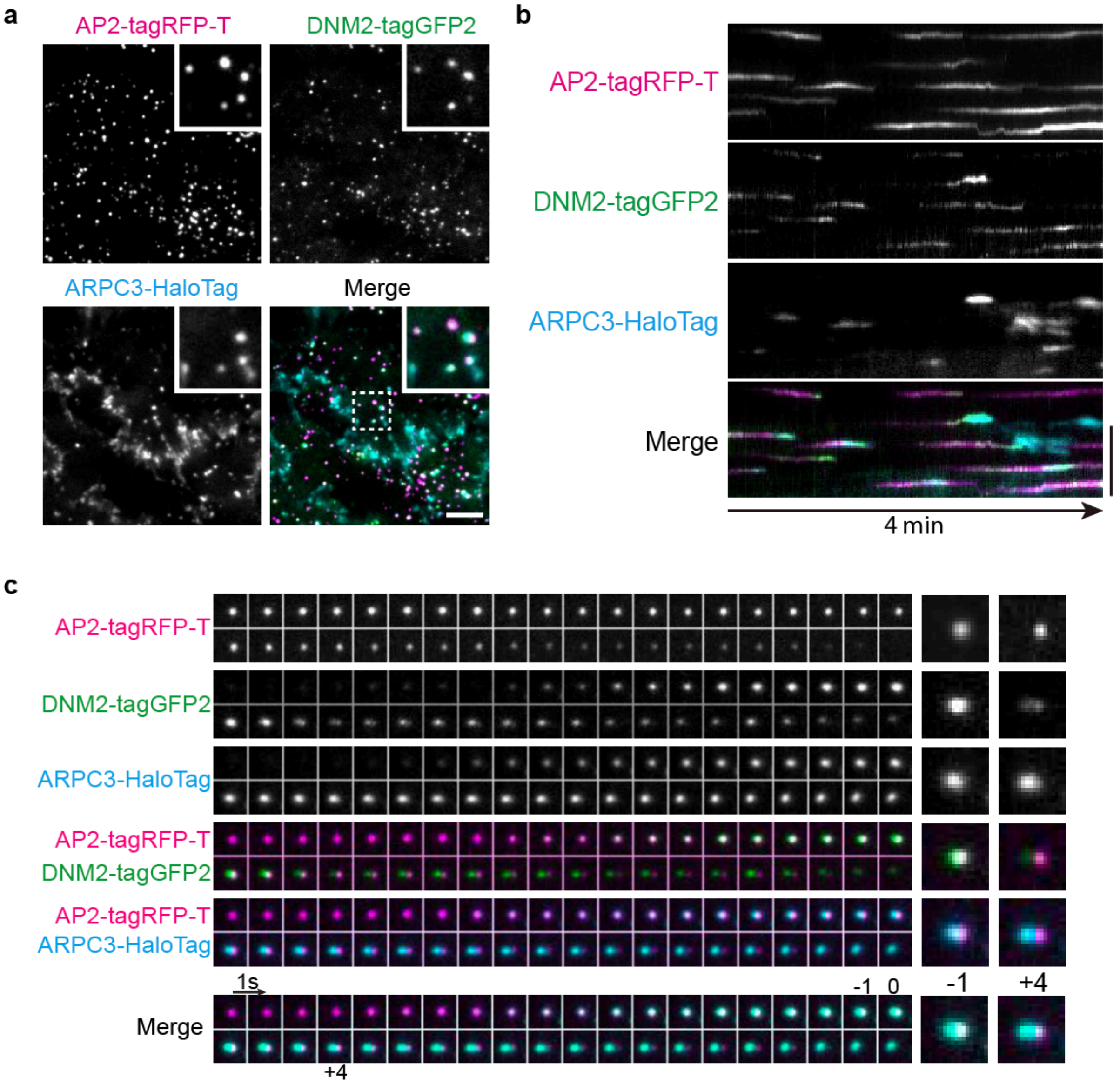

Figure 23 **Triple-genome-edited iPS cells reveal dynamic actin organization at CME sites. a,** A representative single time frame image of a TIRF movie (Supplementary Video 2) of AP2M1-tagRFP-T (magenta), DNM2-tagGFP2 (green) and JF635 ligand[38]-conjugated ARPC3-HaloTag (cyan) in ADA cells. The highlighted region is boxed by a dashed line. Scale bar: 5µm. **b,** A representative kymograph of AP2M1-tagRFP-T (magenta), DNM2-tagGFP2 (green) and JF635 ligand-conjugated ARPC3-HaloTag (cyan) at CME sites in ADA cells. Scale bar: 5µm. **c,** Montage of a representative ARPC3 positive CME site in ADA cells. Individual channels and pair-wise and triple (bottom) merges are shown. The "0" frame indicates the timing of the DNM2 peak / vesicle scission. The images of the frames 1 second before (-1) and 4 seconds after (+4) scission are highlighted. Size of field of view: 2µm x 2µm. Intervals: 1sec.

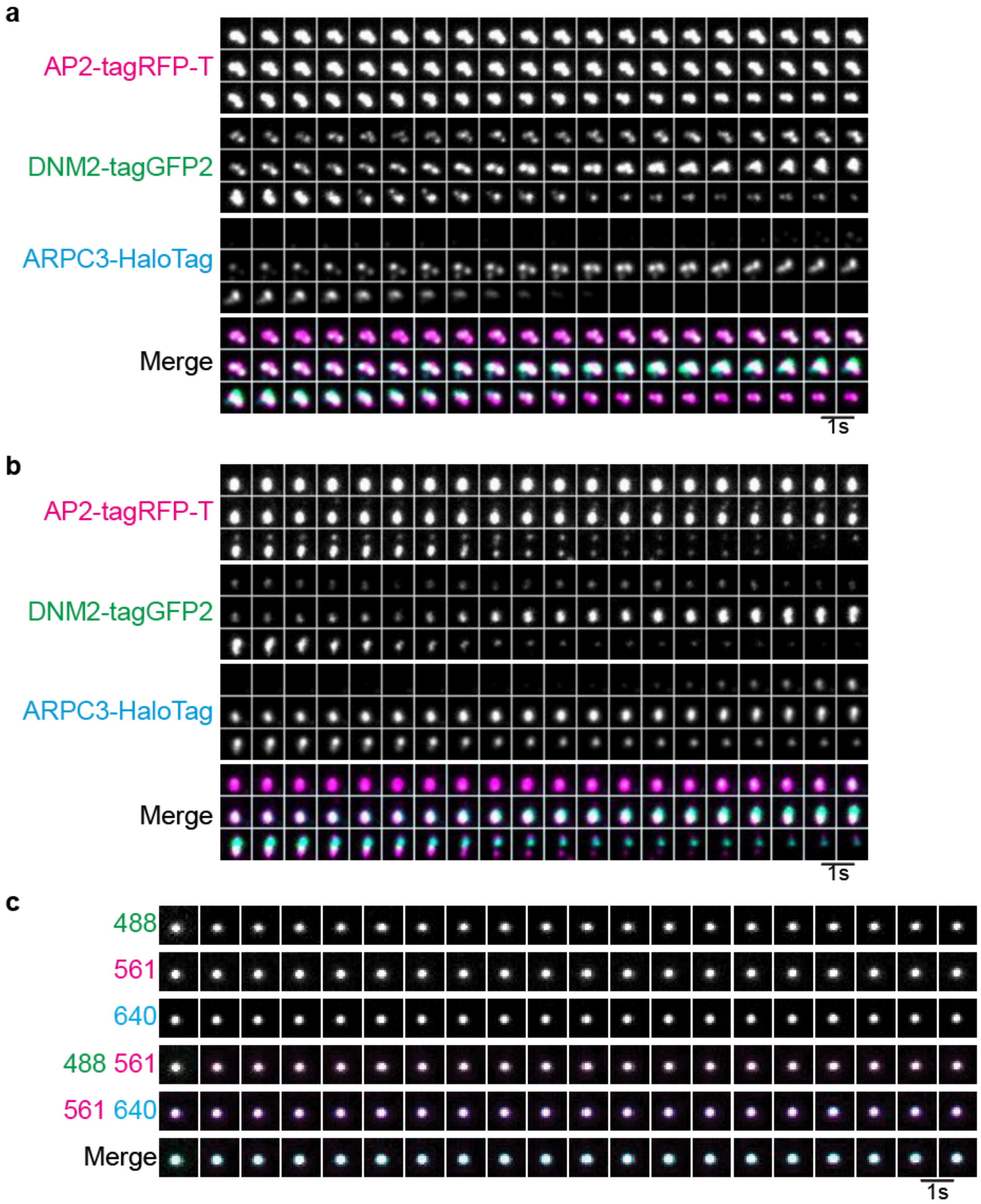

Figure 24 **Actin assembles at different types of CME sites. a,** Montage of a representative ARPC3 positive CME plaque from a TIRF movie of triple-edited (AP2M1-tagRFP-T/DNM2-tagGFP2/ARPC3-HaloTag; ADA) human iPSCs **b,** Montage of a representative ARPC3 positive splitting CME site from a TIRF movie of triple-edited (AP2M1-tagRFP-T/DNM2-tagGFP2/ARPC3-HaloTag; ADA) human iPSCs. **c,** Montage from a TIRF movie of a multi-fluorescence bead. Size of field of view: 2μm x 2μm. Intervals: 1sec.

To analyze the intrinsic recruitment order and timing for up to three endocytic proteins at CME sites quantitatively and systematically, we developed a high-throughput method that does not involve any manual selection of CME sites, which is prone to bias (see Materials and Methods). Briefly, AP2 tracks were identified using standard particle-tracking algorithms[22]. Novel filtering methods then extracted DNM2-positive events marked by one or more DNM2 burst. The AP2 and

DNM2 tracks were decomposed into dynamic features describing the events' position and brightness. These features were used for clustering via unsupervised machine learning, which enabled grouping of similarly-behaved tracks (Fig. 26a and b). DNM2-positive events were refined by a detection scheme that determined the number of DNM2 peaks using various characteristics of a single DNM2-peak: the peak height, width, and minimum peak-to-peak distance (Fig. 26c). Events with a single DNM2 peak were analyzed as described below. The method detects low signals from endogenously tagged CME proteins, such as the low-level recruitment of DNM2 at the early stages of CME, and accurately reveals the different CME stages (Fig. 26d).

Next, the timing of actin network assembly at CME sites was determined using ARPC3 as a branched actin filaments marker by analyzing over one thousand CME events. Although actin appearance early in CME has been reported[7], determining the actin assembly timing is challenging because actin dyes lack the specificity required to distinguish newly assembled branched actin at CME sites from the nearby cortical actin filaments or actin filaments attached to other vesicles or organelles. Also, whether actin functions during the early stage of CME has not yet been shown conclusively due to the potential side effects such as changes in membrane tension caused by actin inhibitors. We classified ARPC3 positive CME events into two groups: one with ARPC3 appearance early in CME and the other late in CME (Fig. 25a). We observed that in most of the events (66.7%) a sharply increasing ARPC3 signal appears with similar timing to the rapid-recruitment phase of DNM2 concomitant with the U to Ω membrane shape transition. This timing is consistent with previously proposed role for actin in membrane invagination, as studies showed that actin inhibitors block the U to Ω endocytic membrane shape transition[23]. In some cases (33.2%) we detected ARPC3 signals at early CME stages. To test whether random overlap between nearby actin structures and CME sites might be responsible for the apparent early actin recruitment, we generated a randomized data set by pairing ARPC3 images with AP2 and DNM2 images from an unrelated movie (Fig. 25b). In this data set, we detected early "assembly" of actin in the majority of ARPC3 positive CME events (73.6%), and the intensity profiles of these events resembled the early-actin CME events we observed in the real data set (Fig. 25a, b). Therefore, we conclude that the presence of actin early in CME is very likely due to unrelated nearby actin structures overlapping with CME sites.

Our live-cell analysis allowed the timing of branched actin network assembly to be compared to the scission timing, and the spatial offset between the clathrin coat and the associated actin network to be determined. Super-resolution imaging of yeast CME sites suggested that actin and actin nucleators localize symmetrically in a ring around CME sites, and computational modeling suggested that an asymmetric actin arrangement would not provide sufficient force for the membrane invagination during yeast CME[6]. In contrast, in mammalian cells, which require less actin force production during CME, imaging of fixed cells suggested that actin structures associate adjacent to apparent flat clathrin coats. However, these studies proposed that at the later CME stages the actin structures become larger and more symmetric to provide sufficient force for membrane deformation and scission[7,8]. Surprisingly, in our live cell studies designed to highlight sites of new actin assembly, we observed off-centered branched actin networks at CME sites throughout even the latest CME stages (Fig. 23c). Furthermore, most ARPC3-positive CME sites accomplish scission within 30s from the initiation of ARPC3 recruitment (Fig. 25c). The actin networks were off center from the coat signals by approximately 150nm at the time of vesicle scission (Fig. 25d). This observation is consistent with the observation that ring-shaped actin structures at clathrin coats were rarely observed in the high-resolution, live-cell imaging in a previous study[24]. In total, these live-cell data suggest that in mammalian cells, asymmetric actin network assembly can provide enough force to assist membrane deformation and scission during the late stages of CME, though recent work suggests that actin symmetry may increase at in response to elevated membrane tension[9].

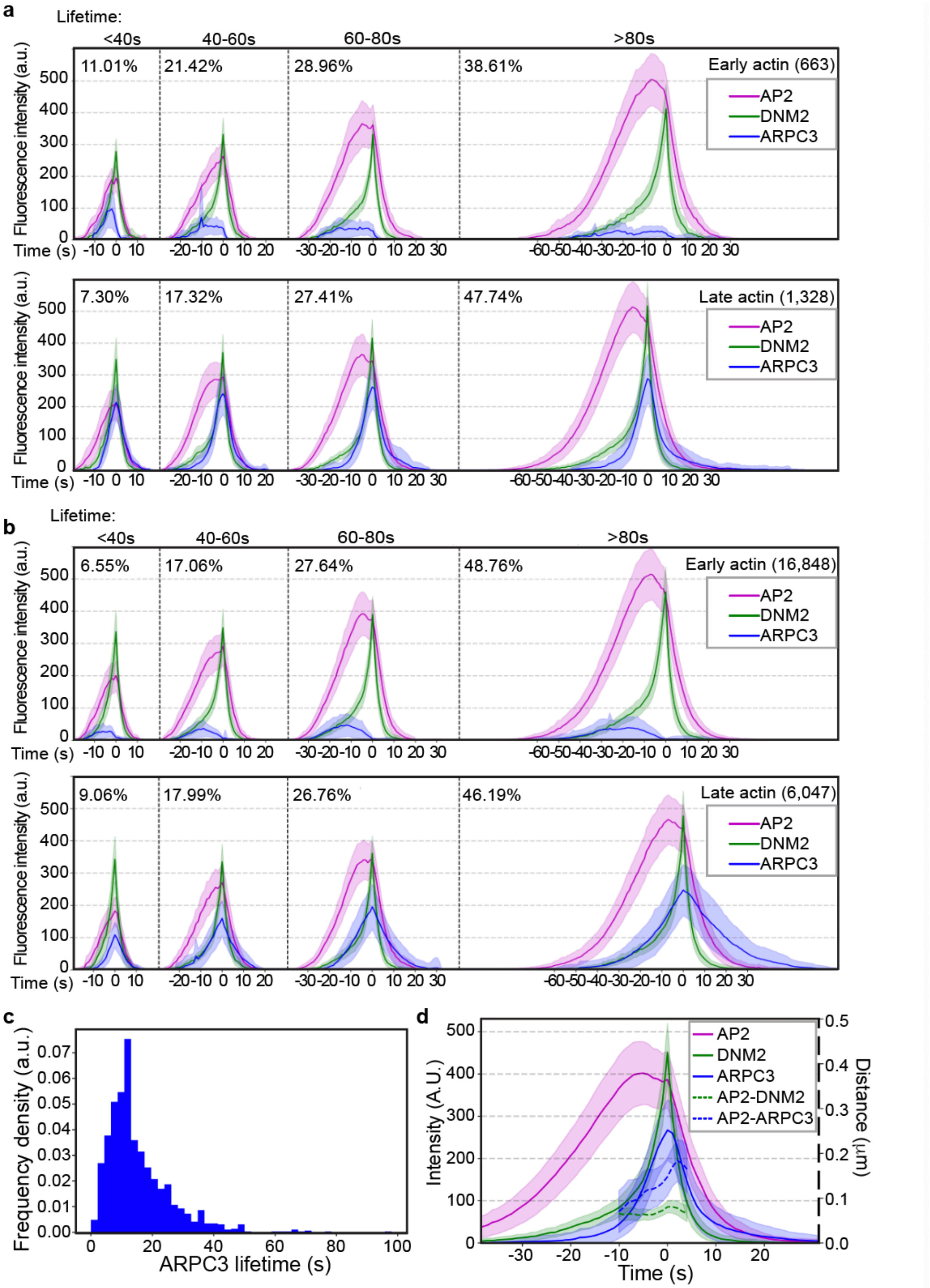

Figure 25 **Computational analysis of ARPC3 positive CME sites reveals asymmetric actin network assembly at the late stage of CME. a, b,** Averaged intensity vs time plots of cohorts of ARPC3 positive CME sites in ADA cells (**a**) and in the randomized data set (**b**). Events are grouped by the timing of ARPC3-labeled branched actin network recruitment (early: top, late: bottom), and then grouped into cohorts by the lifetimes of AP2 and aligned to the frames showing the maximum DNM2 intensity (time = 0s). Total number of CME sites in each group is shown in parentheses. Percentage of the number of the CME sites in each cohort is shown next to the plot. **c,** Histogram of ARPC3-mediated actin network assembly duration. The assembly duration is measured from the first frame of the ARPC3 signal to the presumed scission time (the peak of DNM2 signal). **d,** Averaged intensity (solid lines) and distance (dashed lines) vs time plots of ARPC3 positive CME sites in ADA cells. Events are aligned to the frames showing the maximum DNM2 intensity (time = 0s). Distance between centers of two signals are shown from -10s to 3s when DNM2 and ARPC3 signals are relatively high. N=1,328. **a, b, d,** Error bar: ¼ standard deviation.

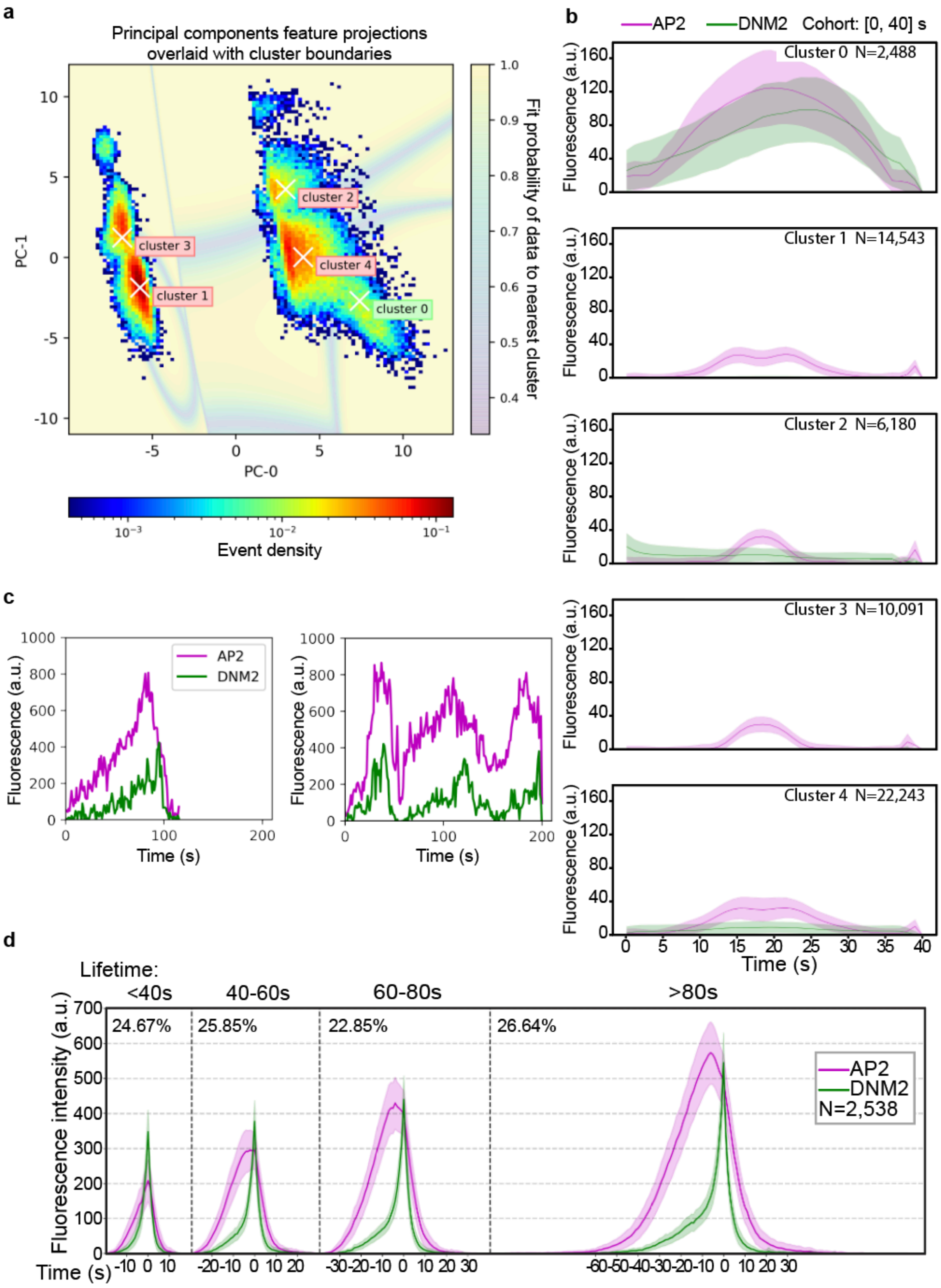
a
Principal components feature projections overlaid with cluster boundaries
PC-1
PC-0
cluster 0
cluster 1
cluster 2
cluster 3
cluster 4
Fit probability of data to nearest cluster
Event density
b
AP2
DNM2
Cohort: [0, 40] s
Cluster 0 N=2,488
Cluster 1 N=14,543
Cluster 2 N=6,180
Cluster 3 N=10,091
Cluster 4 N=22,243
Fluorescence (a.u.)
Time (s)
c
AP2
DNM2
Fluorescence (a.u.)
Time (s)
d
Lifetime:
<40s
40-60s
60-80s
>80s
24.67%
25.85%
22.85%
26.64%
AP2
DNM2
N=2,538
Fluorescence intensity (a.u.)
Time (s)

Figure 26**. Filtering methods for selection of CME sites. a,** 2-D histogram of the first two principal components (PCs) of AP2 and DNM2 dynamic features. The shaded underlay represents simulated data points in principal component space and their individual probabilities of belonging to the nearest cluster center. Cluster 0 shows data points in the DNM2-positive cluster. **b,** Cohort plots of the shortest AP2 events (<40 seconds) from each cluster. Cluster 0 represents DNM2-positive events where a strong DNM2 signal is detected. **c,** DNM2-positive events are sorted by the number of DNM2 peaks using a peak-detection scheme. Representative intensity vs time plots of a single-peaked event (left) and a multi-peaked event (right). **d,** Single-peaked DNM2 events, hereon named CME sites, are grouped into lifetime cohorts and aligned to the peak of the DNM2 channel.

To gain new insights into the function of this asymmetric actin network assembly, we quantitatively compared CME events with or without ARPC3 recruitment. We observed that about 30% of CME events are completed in the absence of detectable actin assembly, which is consistent with the hypothesis that in mammalian cells actin assembly is required for CME only under relatively high membrane tension, which can vary regionally within cells[9,23]. Consistent with the possibility that increased membrane tension stalls membrane deformation during CME[5,25,26], CME lifetimes were markedly longer for ARPC3 positive events compared to the ARPC3 negative events (Fig. 27a). In addition, when the intensity profiles for AP2M1 were compared between ARPC3 positive and negative CME sites, a plateau in the AP2M1 intensity vs time profile was observed for the ARPC3 positive events (Fig. 27b). Based on these observations and previous experimental and computational modeling data[5,9,23], we propose that this plateau in branched actin-positive CME events represents stalled membrane bending due to an unfavorable local membrane environment, such as higher membrane tension[5,25,26].

We hypothesized that the asymmetric actin network might affect the lateral movements of endocytic coats on the plasma membrane. Interestingly, the ARPC3 positive CME sites showed significantly slower, but more directional lateral movement before the scission compared to the ARPC3 negative CME sites (Fig. 27c, d). After scission both ARPC3 positive and negative vesicles showed fast, apparently random movements (Fig. 27c, d). These data suggest that the asymmetric actin can stabilize the forming endocytic coat while pushing it in the plane of the plasma membrane with a lateral directional force.

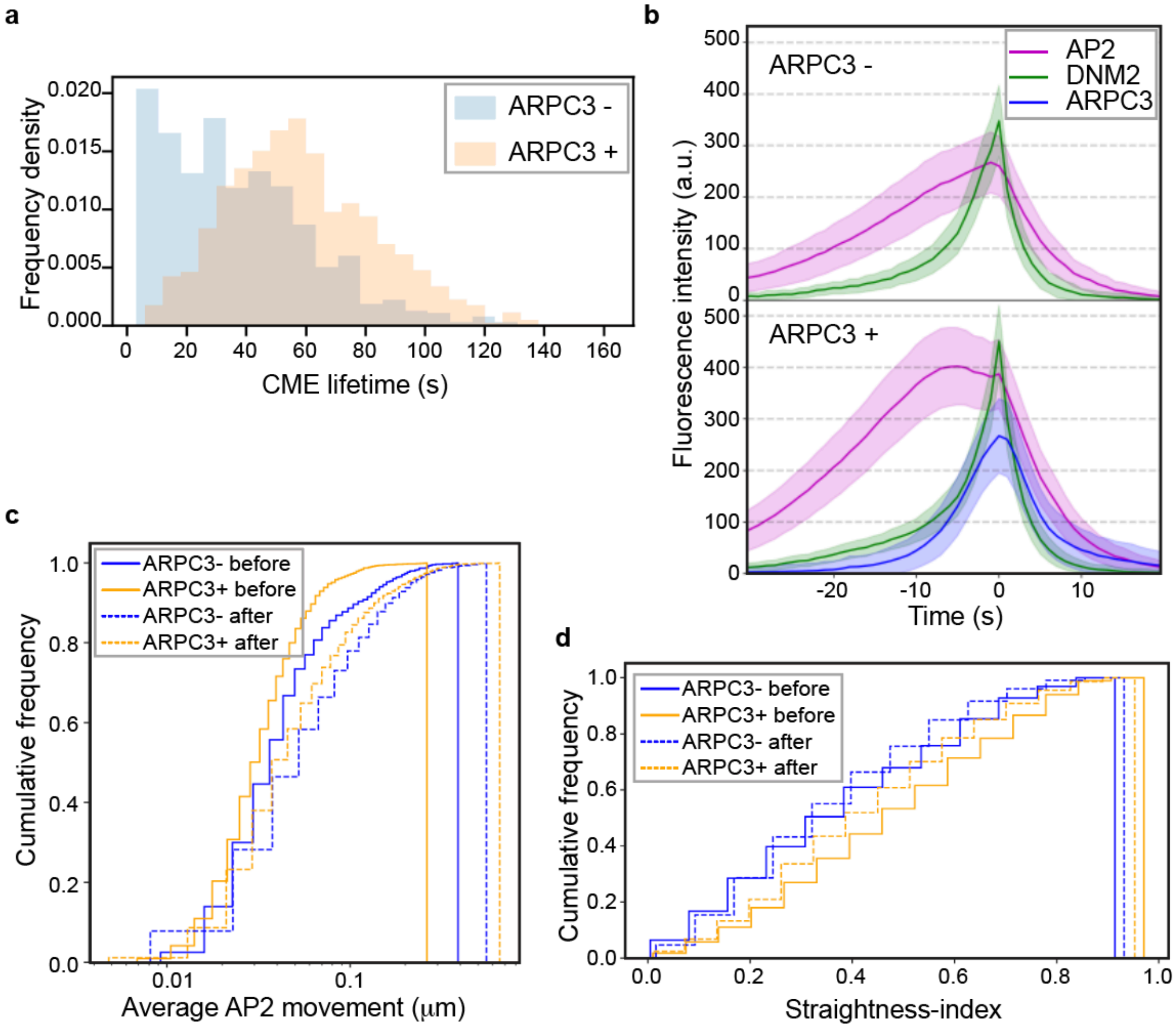

Figure 27 **Actin positive CME sites show distinct dynamics. a,** Histograms of ARPC3 negative (blue) and positive (orange) CME lifetimes. CME lifetime is measured from the first frame of the AP2 signal to the presumed scission time (the peak of DNM2 signal). ARPC3 positive CME events have longer lifetimes. **b,** Averaged intensity vs time plots of ARPC3 negative (top) and positive (bottom) CME sites in ADA cells. Events were aligned to the frames showing the maximum DNM2 intensity. Error bar: ¼ standard deviation. **c,** Lateral motility of ARPC3 negative (blue) and positive (yellow) CME sites before (solid line) and after (dashed line) vesicle scission. ARPC3 positive CME sites move slower than ARPC3 negative ones. **d,** Straightness-index of ARPC3 negative (blue) and positive (yellow) CME sites before (solid line) and after (dashed line) scission. The straightness-index is defined by the ratio between the sum of frame-to-frame distances to the end-to-end distance of a single event's trajectory, where a perfectly straight-lined trajectory would have an index of 1. APRC3 positive CME sites move with a straighter trajectory. **a-d,** ARPC3 -: N=840, ARPC3 +: N=1,328.

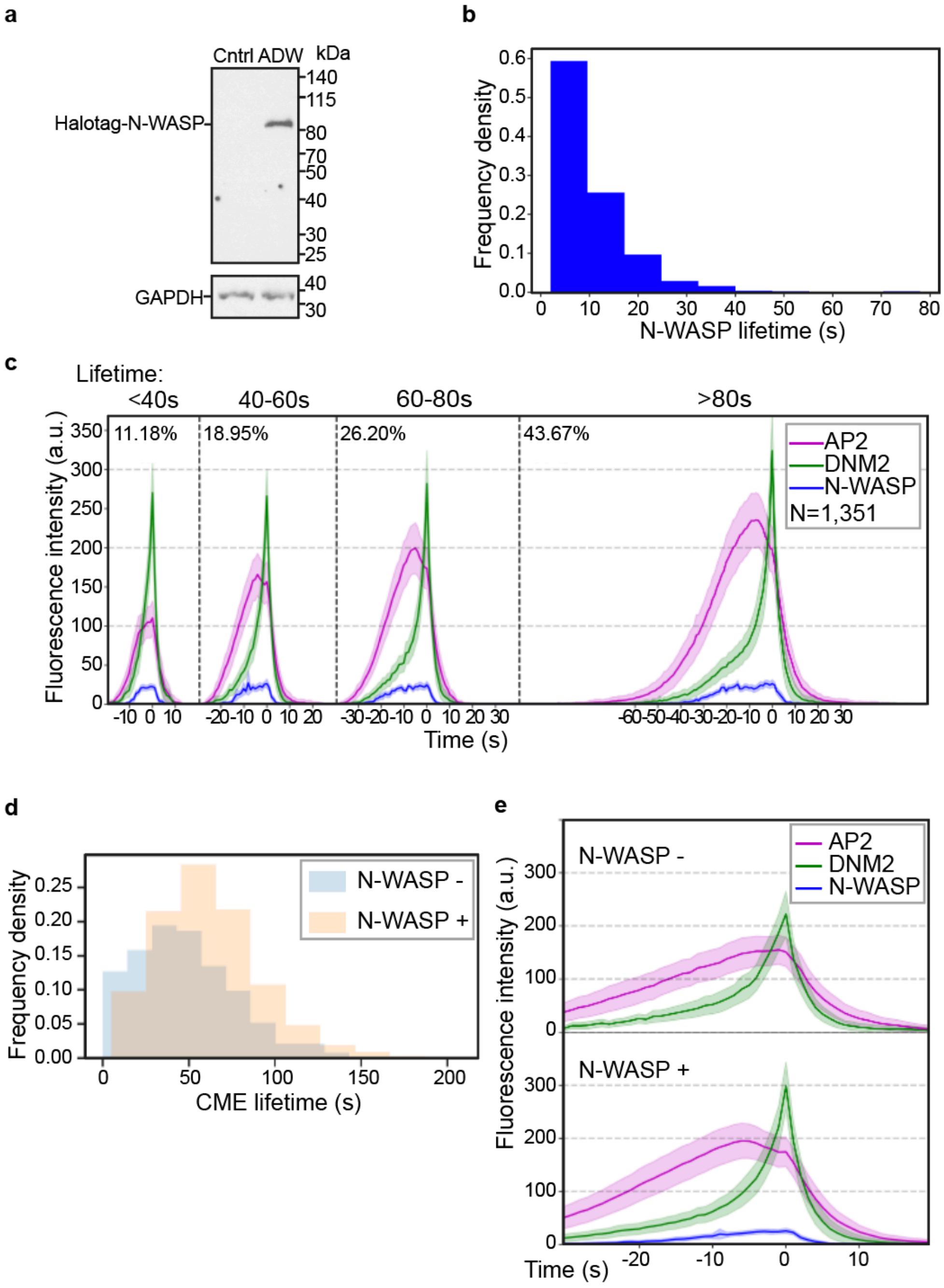

Figure 28**. Computational analysis reveals distinct dynamics of N-WASP positive CME sites. a,** Immunoblot analysis of cell extracts from the control and genome-edited (AP2M1-tagRFP-T/DNM2-tagGFP2/HaloTag-WASL; ADW) human iPSCs. The labeled proteins were detected with HaloTag and GAPDH (loading control) antisera respectively. **b,** Histogram of N-WASP lifetime at CME sites. The lifetime is measured from the first frame of the N-WASP signal to the presumed scission time (the peak of DNM2 signal). **c,** Intensity vs time plots of cohorts of N-WASP positive CME sites in ADW cells. Events are grouped into cohorts by the lifetimes of AP2 and aligned to the frames showing the maximum DNM2 intensity. **d,** N-WASP positive CME events have longer lifetimes. **e,** Intensity vs time plots of averaged N-WASP negative (top) and positive (bottom) CME sites in ADW cells. Events were aligned to the frames showing the maximum DNM2 intensity. **b-d,** N-WASP negative CME sites: N=386, N-WASP positive CME sites: N=1,351

To further explore how the asymmetrical assembly of actin networks at CME sites is regulated, we endogenously tagged N-WASP, an actin nucleation promoting factor (NPF) that plays roles in CME, in AP2M1-tagRFP-T/ DNM2-tagGFP2 genome-edited iPSCs (hereafter referred to as ADW cells, Fig. 29a and 28a). In these cells, N-WASP was recruited asymmetrically to CME sites at the late stage (Fig. 29b-d and Fig. 28b, c). Longer lifetimes and a plateau in the AP2 intensity vs time plot were observed specifically in the N-WASP positive CME events (Fig. 28d, e). These data indicate that asymmetric NPF recruitment underlies the asymmetric architecture of branched actin networks at CME sites.

Based on the data presented here, we propose an updated model of actin assembly at mammalian CME sites (Fig. 29e): (1) Where the local membrane tension is lower, (Fig. 29e upper scenario) the membrane can undergo flat-U-Ω shape transitions without actin assembly in a relatively short time. When the coat grows large enough to form a Ω-shaped bud, sufficient dynamin can be recruited to perform scission, and there is little delay between coat expansion and scission; (2) Where the local membrane tension is high and the coat protein-membrane interaction does not generate sufficient force to curve the membrane, extra force generation from actin assembly is required[5,23]. Asymmetric N-WASP recruitment activates actin nucleation mostly at one side of the clathrin coat, generating an asymmetric force that pulls the membrane into the cell with a similar action to a bottle cap opener. We speculate that this asymmetrical force may also deform the vesicle neck and twist the clathrin coat to promote scission. CME events with associated actin assembly have longer lifetimes, likely due to a delay between coat expansion and scission, requiring adaptive recruitment of actin regulators followed by actin network assembly and membrane remodeling.

Under the cell culture conditions used in this study, we observed asymmetric actin assembly at CME sites in living mammalian cells, which is different from the symmetric actin structures observed at CME sites in yeasts[6], which grow under high turgor pressure and require actin assembly for membrane invagination[27]. However, interestingly, a recent study has shown that when the membrane tension is increased artificially, larger and more symmetric actin networks form at CME sites in mammalian cells as well[9]. This observation, together with our new data, suggests that actin assembly at CME sites undergoes conserved but highly adaptive regulation in yeasts and mammalian cells. Asymmetric actin assembly is the default mode when a relatively small amount of force is sufficient to drive membrane remodeling. However, adaptive mechanisms result in assembly of larger, more symmetric actin structures that provide larger amounts of force to counter high membrane tension or turgor pressure.

Future computational modeling studies of how asymmetric actin network assembly provides forces for vesicle formation and membrane remodeling will deepen our understanding of actin's functions in a host of actin-mediated processes.

Our model provides further insights into the basis for inconsistent effects of actin drugs on CME[7,12,23,27–32]. Actin plays crucial roles in membrane shaping, cell adhesion and membrane tension. Global disruption of actin dynamics is expected to dramatically change membrane tension and therefore to have both direct and indirect effects on CME.

The results presented here also provide considerations relevant to the constant coat area vs constant coat curvature models for how the clathrin coat assembles and develops curvature. In the constant area model, flat clathrin coats grow close to their final size before becoming curved into a vesicle. In the constant curvature model, clathrin coats grow with a fixed curvature. These two models of CME are under active debate[25,33–37]. Our observations suggest that coat expansion and curvature generation may be regulated via distinct mechanisms, with different actin requirements. Our data show that at actin-positive CME sites, actin assembles at the late stage of CME when coat assembly is mostly completed (Fig. 25 and Fig. 30a). In the constant curvature model, we would find actin-associated clathrin coats in only highly curved dome and spherical shapes (Fig. 30b). However, actin-associated flat or shallow clathrin coats have been observed in multiple studies[8,9], which supports the constant area model at actin-positive CME sites (Fig. 30c). Mathematical modeling predicts that at actin-negative CME sites, where coat proteins provide sufficient force to bend the membrane[23], the membrane smoothly evolves from a flat to budded morphology as the coat area increases[5], which supports constant curvature model. Therefore, in the future studies, the constant coat area and constant coat curvature models need to be tested separately on a single type of CME event.

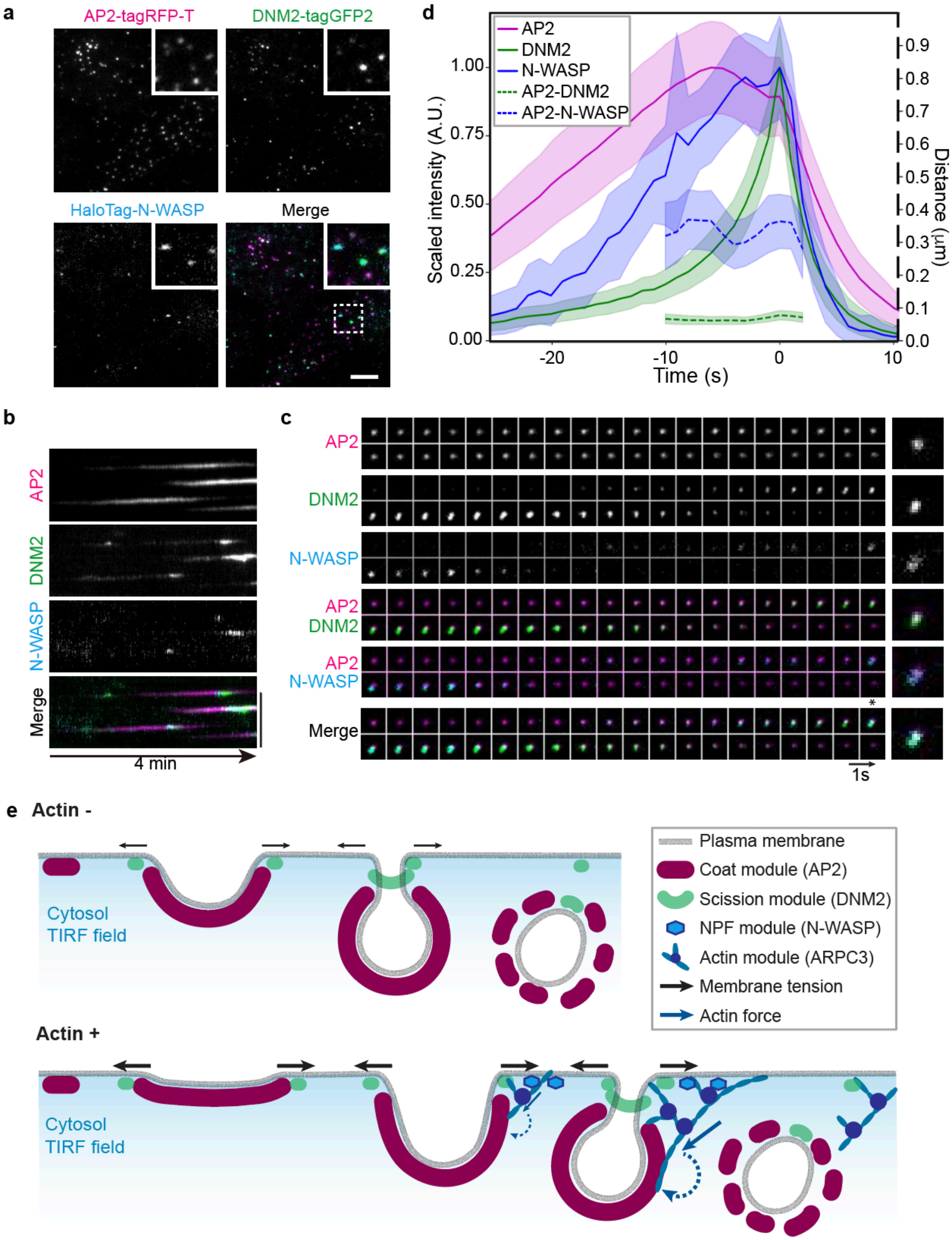
a
AP2-tagRFP-T
DNM2-tagGFP2
HaloTag-N-WASP
Merge
d
AP2
DNM2
N-WASP
AP2-DNM2
AP2-N-WASP
Scaled intensity (A.U.)
1.00
0.75
0.50
0.25
0.00
-20
-10
0
10
Time (s)
Distance (μm)
0.9
0.8
0.7
0.6
0.5
0.4
0.3
0.2
0.1
0.0
b
AP2
DNM2
N-WASP
Merge
4 min
c
AP2
DNM2
N-WASP
AP2
DNM2
AP2
N-WASP
Merge
*
1s
e Actin -
Cytosol
TIRF field
Actin +
Cytosol
TIRF field
Plasma membrane
Coat module (AP2)
Scission module (DNM2)
NPF module (N-WASP)
Actin module (ARPC3)
Membrane tension
Actin force

Figure 29 **Asymmetric N-WASP recruitment to CME sites. a,** A representative single time frame image of a TIRF movie of AP2M1-tagRFP-T (magenta), DNM2-tagGFP2 (green) and JF635 ligand-conjugated HaloTag-N-WASP (cyan) in ADW cells. The highlighted region is boxed by a dashed line. Scale bar: 5μm. **b,** A representative kymograph of CME sites in ADW cells over a 4 min movie. Scale bar: 5μm. **c,** Montages of a representative N-WASP positive CCP in ADW cells. Pair-wise and triple (bottom) merges are shown. Images from a time before the scission (*) is marked to show the displacement between the CME coat (AP2) and N-WASP. Field of the view: 2μm x 2μm. Intervals: 1s. **d,** Averaged intensity (solid line) and distance (dashed line) vs time plots of N-WASP positive CME sites in ADW cells. Events are aligned to the frames showing the maximum DNM2 intensity. Intensity is scaled to 1 at peaks for each channel. N=1,351. Error bar: ¼ standard deviation. **e,** An updated schematic model of actin negative and actin positive CCPs in human cells. Actin assembly is induced at stalled CME sites, where asymmetric forces pull, bend and possibly twist the plasma membrane against membrane tension to drive membrane invagination and vesicle scission.

a

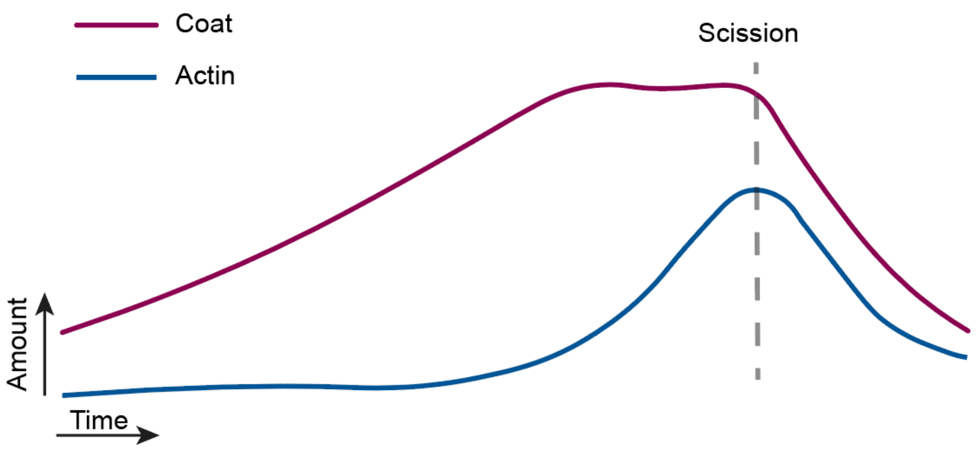

b constant curvature model

c constant area model

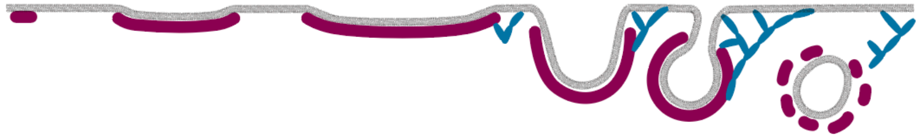

Figure 30 **Constant curvature vs constant area models for how clathrin coats assemble at actin-positive CME sites. a,** A sketch showing amounts of CME coat and actin module proteins at actin-positive CME sites as a function of time based on the data in Fig. 4b. The CME coat is assembled to its maximum area around the time of actin assembly initiation. **b,** Schematic representation of constant curvature model for CME. CME coat assembles during invagination and actin assembles only at deep invaginations. **c,** Schematic representation of constant area model for CME. The CME coat expands to its maximum area first and bends during membrane invagination. In these two different scenarios, actin assembles at CME sites with different curvatures.

Conclusion

Using large-scale and comprehensive analysis of thousands of CME sites, our study demonstrates that in mammalian cells the coat assembly dynamics predict which sites will assemble actin, and show that at those apparently stalled sites, actin assembles asymmetrically to facilitate successful vesicle formation

Material and Methods

Cell culture

The WTC10 hiPSC line was obtained from the Bruce Conklin Lab at UCSF. hiPSCs were cultured on Matrigel (hESC-Qualified Matrix, Corning) in StemFlex medium (Thermo Fisher) with Penicillin/ Streptomycin in 37°C, 5% CO2. Cultures were passaged with Gentle Cell Dissociation reagent (StemCell Technologies, Cat#: 100-0485) twice every week.

Genome-editing

The AP2M1 gene was edited in WTC10 hiPSCs as previously described using TALENs targeting exon 7 of the AP2M1 gene (1). Both alleles of AP2M1 were tagged with tagRFP-T. The Cas9-crRNAtracrRNA complex electroporation method was used sequentially to edit DNM2 and ARPC3 gene in AP2M1-tagRFP-T genome-edited hiPSCs, as previously described (2, 3). The same method was used to edit the WASL gene in AP2M1-tagRFP-T/DNM2-tagGFP2 genome edited hiPSCs. *S. pyogenes* NLS-Cas9 was purified in the University of California Berkeley QB3 MacroLab. TracrRNA and crRNA that target CCTGCTCGACTAGGCCTCGA (DNM2), CCTGGACAGTGAAGGGAGCC (ARPC3) and AGCTCATGGTTTCGCCGGCG (WASL), were purchased from IDT. Gibson assembly (New England Biolabs) was used to construct donor plasmids containing DNM2 5' homology-ggtaccagtggcggaagc-tagGFP2-DNM2 3' homology, ARPC3 5' homology-ggatccggtaccagcgatccaccggtcgccacc-HaloTag-ARPC3 3' homology, and WASL 5' homology-HaloTag-agcgatccaccggtcgccaccggatcc-WASL 3' homology sequences, respectively. Three days after electroporation (Lonza, Cat#: VPH-5012) of the Cas9-crRNA-tracrRNA complex and donor plasmid, the tagGFP2 or HaloTag positive cells were single cell sorted using a BD Bioscience Influx sorter (BD Bioscience) into Matrigel-coated 96-well plates. Clones were confirmed by PCR and Sanger sequencing of the genomic DNA locus around the insertion site. Both alleles of DNM2 and ARPC3 were tagged with tagGFP2 and HaloTag, respectively, and one allele of WASL was tagged with HaloTag in the hiPSC lines used in this study.

Western blotting

Cells were dissociated from the well using Gentle Cell Dissociation reagent (StemCell Technologies, Cat#: 100-0485). Total proteins were extracted by adding 1ml of cold 10% TCA to the cell pellets, incubated on ice for 30min, and spun down by centrifuging at 4 °C, 12000rpm for 10min. Protein pellets were dissolved in loading buffer (50 mM HEPES, pH 7.4, 150 mM NaCl, 1 mM MgCl2, 5% BME, 5mM DTT and protease inhibitor) and loaded onto an acrylamide gel for SDS-PAGE and transferred to nitrocellulose membranes for immunoblotting. Blots were incubated overnight at 4°C with primary antibodies targeting Tag(CGY)FP (1:2000 dilution in 1% milk, Evrogen, Cat#: AB121), HaloTag (1:1000 dilution in 0.5% milk, Promega, Cat#: G9211), GAPDH (1:100,000 dilution in 0.5% milk, Proteintech, Cat#: 10494-1-AP), respectively, and subsequently incubated in the dark at room temperature for 1hr with secondary antibodies.

TIRF live-cell imaging

Two days before imaging, hiPSCs were seeded onto Matrigel-coated 4-well chambered cover glasses (Cellvis). Halotag was labeled by JF635- HaloTag ligand (4). Cells were incubated in StemFlex medium with 100 mM JF635-HaloTag for 45min and the unbound ligands were washed away by three washes with 5 min incubation in prewarmed StemFlex medium. Cells were imaged on a Nikon Ti-2 inverted microscope fitted with TIRF optics and a sCMOS camera (Hamamatsu). Cells were maintained at 37 °C with a stage top incubator (OKO Lab) in StemFlex medium with 10mM HEPES. Images were acquired with Nikon Elements. Channels were acquired sequentially at a 1 sec interval and 300ms exposure time over 4 minutes.

Four generalized processing steps were applied identify of clathrin-coated pits with single DNM2 peaks: track feature abstraction, feature dimensionality reduction, event clustering, and DNM2-peak detection. First, tracks that are defined by fitted positions and intensities for single events were generated using cmeAnalysis (5). Then, AP2 and DNM2 tracks were decomposed into dynamic features describing the dynamics of the events' position and brightness. These features were clustered after feature scaling, dimensionality reduction with principal component analysis, and Gaussian mixture modeling. DNM2-positive events represented a distinct cluster of tracks containing DNM2 throughout the event, were long lived, and were below the threshold of motility expected for transient, non-CME-derived clathrin-coated vesicle "visitors" at the TIRF field. Single DNM2-peak events were found over a range of values set for the minimum DNM2 peak height, width, and peak-to-peak temporal distance. After finding single-peaked events in a fixed peak-parameter combination, the lifetime distribution of single peak events' lifetimes were fit to the expected underlying distribution, a Rayleigh distribution (6), where the best-fitting parameter combination was chosen to identify single-peaked events.

Two-color, 3D STORM imaging

12 mm round coverslips were sonicated in distilled water and sterilized 20 min in 70% ethanol, air-dried and coated with Matrigel in 24-well plates. Cells were seeded onto Matrigel coated coverslips two days before fixation. For clathrin and actin two-color imaging, cells were fixed first for 1 min in 0.3% (v/v) glutaraldehyde (GA) solution containing 0.25% (v/v) Triton in cytoskeleton buffer (CB: 10mM MES, 150mM NaCl, 5mM EGTA, 5mM Glucose, 5mM $MgCl_2$, 0.005% NaN_3, pH 6.1) and then immediately fixed for 20 min in 2% (v/v) GA solution in CB. Both solutions were prepared fresh from a 10% GA stock (Electron Microscopy Science, cat #16120). After fixation, samples were incubated twice for 5 min in freshly prepared 0.1% (w/v) NaBH4 in PBS. For clathrin and ARPC3-HaloTag imaging, cells were fixed for 20 min in 4% (v/v) PFA (Electron Microscopy Sciences, Cat#: 15710) in CB. Subsequently, both types of samples were washed 3 times for 10 min in PBS. Samples were then blocked for 20 min in blocking buffer (3% (w/v) BSA and 0.1% (w/v) Saponin in PBS). Clathrin light chain (Invitrogen, Cat#: MA5-11860, 1:200 dilution) and Halotag (Promega, Cat#: G9281, 1:200 dilution) antibodies were used in blocking solution. Primary antibody immunostaining was performed overnight at 4°C. On the next day, samples were washed three times in washing buffer (0.1x blocking buffer in PBS) for 10

min. Homemade mouse secondary antibody-CF680 (1:50) was used to stain clathrin and actin samples. Commercial mouse secondary antibody-AF647 (ThermoFisher, cat#A32787; 1:400) and homemade rabbit secondary antibody-CF680 (1:50) were used to stain the clathrin and ARPC3-HaloTag. Samples were incubated with secondary antibody in blocking buffer for 30 min at room temperature in the dark and washed three times for 10 min in washing buffer, and then three times for 10 min in PBS. Clathrin and actin samples were then stained with 0.5µM Phalloidin-AF647 (Fisher Scientific, Cat#: A22287) in PBS and kept at room temperature in the dark for 2 hours. Samples were washed three times with PBS before STORM imaging.

STORM imaging was performed as previously described (7). Samples labeled by AF647 and CF680 were excited by an 647nm laser. The emitted light for AF647 and CF680 was then split into two light paths as two channels using a dichroic mirror (Chroma, cat#T685lpxr) and each channel was projected onto one-half of an EMCCD camera (Andor iXon Ultra 897). Color assignment of each localization was based on its intensity in each channel. A Cylindrical lens was inserted into brighter channel to acquire 3D localization data (8). The 3D position of each position in the z dimension was estimated based on the ellipticity of each point spread function.

References

1. Rottner, K., Faix, J., Bogdan, S., Linder, S. & Kerkhoff, E. Actin assembly mechanisms at a glance. *J. Cell Sci.* **130**, 3427–3435 (2017).
2. Lanzetti, L. Actin in membrane trafficking. *Current Opinion in Cell Biology* (2007). doi:10.1016/j.ceb.2007.04.017
3. Lu, R., Drubin, D. G. & Sun, Y. Clathrin-mediated endocytosis in budding yeast at a glance. *J. Cell Sci.* **129**, 1531–6 (2016).
4. Lacy, M. M., Ma, R., Ravindra, N. G. & Berro, J. Molecular mechanisms of force production in clathrin-mediated endocytosis. *FEBS Letters* (2018). doi:10.1002/1873-3468.13192
5. Hassinger, J. E., Oster, G., Drubin, D. G. & Rangamani, P. Design principles for robust vesiculation in clathrin-mediated endocytosis. *Proc. Natl. Acad. Sci. U. S. A.* (2017). doi:10.1073/pnas.1617705114
6. Mund, M. *et al.* Systematic Nanoscale Analysis of Endocytosis Links Efficient Vesicle Formation to Patterned Actin Nucleation. *Cell* (2018). doi:10.1016/j.cell.2018.06.032
7. Yarar, D., Waterman-Storer, C. M. & Schmid, S. L. A dynamic actin cytoskeleton functions at multiple stages of clathrin-mediated endocytosis. *Mol. Biol. Cell* **16**, 964–975 (2005).
8. Collins, A., Warrington, A., Taylor, K. A. & Svitkina, T. Structural organization of the actin cytoskeleton at sites of clathrin-mediated endocytosis. *Curr. Biol.* (2011). doi:10.1016/j.cub.2011.05.048
9. Kaplan, C. *et al.* Adaptive actin organization buffers endocytosis against changes in membrane tension. *bioRxiv* (2021).
10. Taylor, M. J., Perrais, D. & Merrifield, C. J. A high precision survey of the molecular dynamics of mammalian clathrin-mediated endocytosis. *PLoS Biol.* **9**, e1000604 (2011).
11. Kaksonen, M., Toret, C. P. & Drubin, D. G. A modular design for the clathrin- and actin-mediated endocytosis machinery. *Cell* **123**, 305–20 (2005).
12. Dambournet, D. *et al.* Genome-edited human stem cells expressing fluorescently labeled endocytic markers allow quantitative analysis of clathrin-mediated endocytosis during

differentiation. *J. Cell Biol.* **217**, 3301–3311 (2018).

13. Doyon, J. B. *et al.* Rapid and efficient clathrin-mediated endocytosis revealed in genome-edited mammalian cells. *Nat. Cell Biol.* **13**, 331–7 (2011).
14. Gibson, T. J., Seiler, M. & Veitia, R. A. The transience of transient overexpression. *Nat. Methods* **10**, 715–21 (2013).
15. Akamatsu, M. *et al.* Principles of self-organization and load adaptation by the actin cytoskeleton during clathrin-mediated endocytosis. *Elife* (2020). doi:10.7554/eLife.49840
16. Grassart, A. *et al.* Actin and dynamin2 dynamics and interplay during clathrin-mediated endocytosis. *J. Cell Biol.* (2014). doi:10.1083/jcb.201403041
17. Merrifield, C. J., Feldman, M. E., Wan, L. & Almers, W. Imaging actin and dynamin recruitment during invagination of single clathrin-coated pits. *Nat. Cell Biol.* (2002). doi:10.1038/ncb837
18. María Cabeza, J., Acosta, J. & Alés, E. Dynamics and Regulation of Endocytotic Fission Pores: Role of Calcium and Dynamin. *Traffic* (2010). doi:10.1111/j.1600-0854.2010.01120.x
19. Ramachandran, R. & Schmid, S. L. Real-time detection reveals that effectors couple dynamin's GTP-dependent conformational changes to the membrane. *EMBO J.* (2008). doi:10.1038/sj.emboj.7601961
20. Roux, A. *et al.* Membrane curvature controls dynamin polymerization. *Proc. Natl. Acad. Sci. U. S. A.* (2010). doi:10.1073/pnas.0913734107
21. Iversen, T. G., Skretting, G., Van Deurs, B. & Sandvig, K. Clathrin-coated pits with long, dynamin-wrapped necks upon expression of a clathrin antisense RNA. *Proc. Natl. Acad. Sci. U. S. A.* (2003). doi:10.1073/pnas.0534231100
22. Aguet, F., Antonescu, C. N., Mettlen, M., Schmid, S. L. & Danuser, G. Advances in analysis of low signal-to-noise images link dynamin and AP2 to the functions of an endocytic checkpoint. *Dev. Cell* (2013). doi:10.1016/j.devcel.2013.06.019
23. Boulant, S., Kural, C., Zeeh, J. C., Ubelmann, F. & Kirchhausen, T. Actin dynamics counteract membrane tension during clathrin-mediated endocytosis. *Nat. Cell Biol.* **13**, 1124–1132 (2011).
24. Li, D. *et al.* Extended-resolution structured illumination imaging of endocytic and cytoskeletal dynamics. *Science.* (2015). doi:10.1126/science.aab3500
25. Bucher, D. *et al.* Clathrin-Adaptor ratio and membrane tension regulate the flat-To-curved transition of the clathrin coat during endocytosis. *Nat. Commun.* (2018). doi:10.1038/s41467-018-03533-0
26. Saleem, M. *et al.* A balance between membrane elasticity and polymerization energy sets the shape of spherical clathrin coats. *Nat. Commun.* (2015). doi:10.1038/ncomms7249
27. Aghamohammadzadeh, S. & Ayscough, K. R. Differential requirements for actin during yeast and mammalian endocytosis. *Nat. Cell Biol.* **11**, 1039–42 (2009).
28. Kaksonen, M., Sun, Y. & Drubin, D. G. A Pathway for Association of Receptors, Adaptors, and Actin during Endocytic Internalization. *Cell* **115**, 475–87 (2003).
29. Ferguson, S. *et al.* Coordinated Actions of Actin and BAR Proteins Upstream of Dynamin at Endocytic Clathrin-Coated Pits. *Dev. Cell* **17**, 811–22 (2009).
30. Durrbach, A., Louvard, D. & Coudrier, E. Actin filaments facilitate two steps of endocytosis. *J. Cell Sci.* **109**, 457–65 (1996).
31. Lamaze, C., Fujimoto, L. M., Yin, H. L. & Schmid, S. L. The actin cytoskeleton is required for receptor-mediated endocytosis in mammalian cells. *J. Biol. Chem.* **272**, 20332–5 (1997).

32. Miya Fujimoto, L., Roth, R., Heuser, J. E. & Schmid, S. L. Actin assembly plays a variable, but not obligatory role in receptor-mediated endocytosis in mammalian cells. *Traffic* (2000). doi:10.1034/j.1600-0854.2000.010208.x
33. Lampe, M., Vassilopoulos, S. & Merrifield, C. Clathrin coated pits, plaques and adhesion. *J. Struct. Biol.* (2016). doi:10.1016/j.jsb.2016.07.009
34. Kaksonen, M. & Roux, A. Mechanisms of clathrin-mediated endocytosis. *Nature Reviews Molecular Cell Biology* (2018). doi:10.1038/nrm.2017.132
35. Avinoam, O., Schorb, M., Beese, C. J., Briggs, J. A. G. & Kaksonen, M. Endocytic sites mature by continuous bending and remodeling of the clathrin coat. *Science.* (2015). doi:10.1126/science.aaa9555
36. Scott, B. L. *et al.* Membrane bending occurs at all stages of clathrincoat assembly and defines endocytic dynamics. *Nat. Commun.* (2018). doi:10.1038/s41467-018-02818-8
37. Sochacki, K. A. *et al.* The structure and spontaneous curvature of clathrin lattices at the plasma membrane. *bioRxiv* (2020).
38. Grimm, J. B. *et al.* A general method to fine-tune fluorophores for live-cell and in vivo imaging. *Nat. Methods* **14**, 987–994 (2017).

Acknowledgments: MJ was funded by American Heart Association Postdoctoral Fellowship (18POST34000029). DGD was funded by NIH MIRA grant R35GM118149. The authors would like to thank the Conklin Lab at UCSF for providing WTC10 human iPSC line; the Lavis Lab at Janelia Farm for providing JF635 HaloTag ligand; Dr. Sun Hae Hong for generating the AP2-tagRFP-T iPSC cell line; the UC Berkeley QB3 MacroLab for purified S. pyogenes NLS-Cas9; the UC Berkeley Cancer Research Laboratory Flow Cytometry Facility for iPSC sorting.

Supplemental References

1. Hong, S. H. *et al*. Machine-Learning-Based Analysis in Genome Edited Cells Reveals the Efficiency of Clathrin-Mediated Endocytosis. *Cell Rep*. **12**, 2121– 2130 (2015).
2. Dambournet, D. *et al.* Genome-edited human stem cells expressing fluorescently labeled endocytic markers allow quantitative analysis of clathrin-mediated endocytosis during differentiation. *J. Cell Biol*. **217**, 3301–3311 (2018).
3. Akamatsu, M. *et al.* Principles of self-organization and load adaptation by the actin cytoskeleton during clathrin-mediated endocytosis. *Elife* https://doi:10.7554/eLife.49840 (2020).
4. Grimm, J. B. *et al.* A general method to fine-tune fluorophores for live-cell and in vivo imaging. *Nat. Methods*. **14**, 987–994 (2017).
5. Aguet, F. *et al.* Advances in Analysis of Low Signal-to-Noise Images Link Dynamin and AP2 to the Functions of an Endocytic Checkpoint. *Dev. Cell* **26**, 279-291(2013).
6. Loerke, D. *et al*. Cargo and Dynamin Regulate Clathrin-Coated Pit Maturation. *PLOS Biol.* https://doi.org/10.1371/journal.pbio.1000057 (2009).
7. Kaplan, C. *et al.* Adaptive actin organization buffers endocytosis against changes in membrane tension. Preprint at https://www.biorxiv.org/content/10.1101/2020.04.05.026559v2 (2021).
8. Huang, B. *et al.* Three-dimensional Super-resolution Imaging by Stochastic Optical Reconstruction Microscopy. *Science* **319**, 810-813 (2008).

Chapter 5: Functional super-resolution microscopy of the cell

The work in this chapter was conducted in collaboration with Rui Yan, Bowen Wang, and Ke Xu*. It is reproduced in part here from Yan et al with permission from all co-authors. Copyright 2019 *Curr. Opin. Chem. Biol.*

Introduction

The rapid advances in super-resolution (fluorescence) microscopy (SRM) over the past decade [1,2], including single-molecule localization microscopy (SMLM, e.g., STORM [3], (F)PALM [4,5], and PAINT [6]) and stimulated emission depletion (STED) microscopy [7,8], have revolutionized how we perceive the world. The exquisite spatial resolution down to ~10 nm, combined with the inherent benefits of fluorescence microscopy, in particular, high molecular specificity and good compatibility with live samples, enables exciting discoveries in biology and beyond [1,2,9].

As implied by its name, the primary aim of SRM has been to improve the attainable spatial resolution, namely, to resolve the finest possible ultrastructure. The structural information, however, does not tell the full story of how the cell *functions*. The astoundingly ordered internal organization achieved within the small volume of the cell does not stop at the level of geometrical shapes. Driven far away from equilibrium, the local physicochemical parameters within a cell, e.g., pH, small-molecule concentrations, chemical polarity (hydrophobicity), and protein activities, also vary greatly over short distances. Such intracellular "microenvironments" locally regulate biochemical reactions and other cellular processes, and so dictate cell functions at a fundamental level [10,11]. Would it be possible to unveil and visualize such intracellular *functional* information with nanometer-scale (nanoscale) spatial resolution similar to what has been achieved for *structures* with SRM? If so, what new insights can be gained toward our understanding of how the cell works?

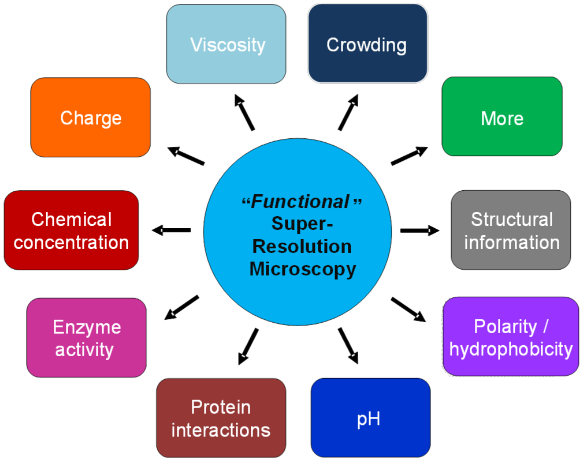

Figure 31. ***Functional* super-resolution microscopy (*f*-SRM)** explores the possibility to transcend the structural (shape) information offered by existing super-resolution methods and unveil multidimensional information of diverse intracellular *functional* parameters, like those shown in this diagram, with nanoscale spatial resolution and ultimate sensitivity down to single molecules.

In this review, we discuss emerging new possibilities to answer these fascinating questions by encoding specific *functional* information of intracellular microenvironments into certain, in some cases novel, dimensions of the SRM signal, a class of methodologies we collectively refer to as *functional* SRM (*f*-SRM; Figure 1). Although multifunctional and multiparametric fluorescence microscopy, often enabled by environment-sensitive and chemical-responsive fluorescent probes [11-16], long preceded the development of SRM, the relatively low spatial resolution (~300 nm) achieved with conventional, diffraction-limited microscopy limits how localized the microenvironments can be probed. As the probed volume scales cubically with the linear dimension, a 10-fold enhancement in spatial resolution, which is often achieved in SRM, could reduce the probed volume by 1,000 times, hence dramatic reduction of interference form the undesired surrounding signal when compared to the desired local signal. For SMLM-based techniques, the possibility to map local properties by examining the response of each probe molecule one at a time further represent the ultimate sensitivity, effectively removing the interferences between different molecules. Below we summarize emergent efforts toward *f*-SRM, grouped by how the functional information is optically encoded.

Fluorescence intensity

Fluorescence intensity is conceivably one of the most straightforward parameters for encoding functional information. Indeed, many fluorescent reporters for chemical imaging are based on fluorescence turn-on [11,13-16].

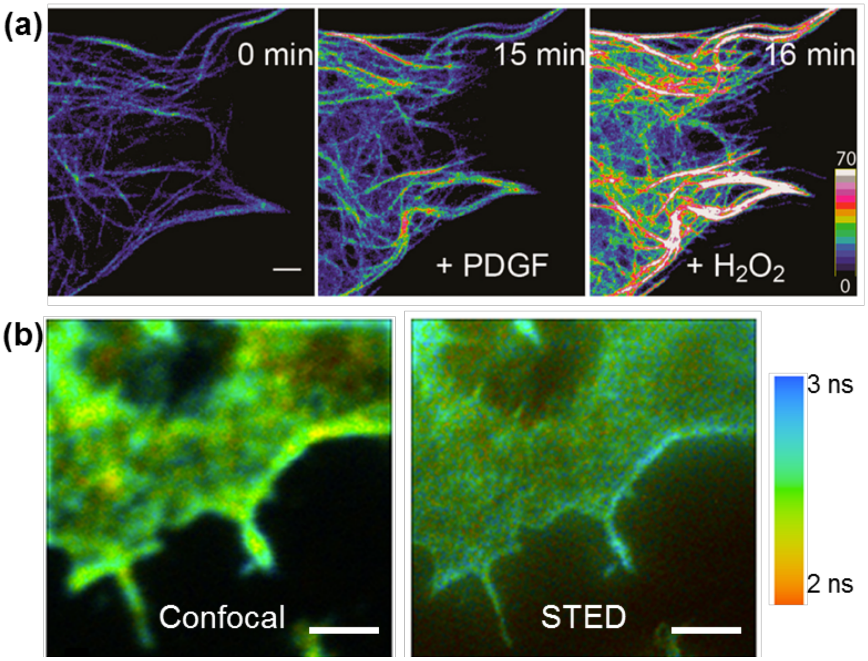

Figure 32. **f-SRM through fluorescence intensity and lifetime detections. (a)** STED images of EB3−HyPer2 fluorescence intensity change in an NIH 3T3 cell at indicated time points, after stimulation with 10 ng/mL PDGF and subsequent addition of 200 μM H_2O_2. **(b)** Comparison of confocal (left) and STED (right) fluorescence lifetime images of a fixed Drosophila S2 cell with Alexa Fluor 594-phalloidin-labeled actin. Scale bars: 2 μm. Panel (a) is adapted from [17]. Panel (b) is adapted from [22].

Mishina *et al.* [17]· adopted this strategy to visualize the concertation of H_2O_2 in live cells with STED SRM. By tagging HyPer2, a fluorescence turn-on fluorescent protein (FP) biosensor for H_2O_2, to the cytoskeleton, STED SRM images provided ~3-fold enhancement in spatial resolution when compared to conventional confocal microscopy. Treatment of the cell with platelet-derived growth factor (PDGF), as well as with H_2O_2, led to modest and substantial increases in the STED-measured HyPer2 intensity (Figure 2a), respectively, attributable to corresponding rises in local intracellular H_2O_2 concentration. In a more sophisticated approach, Mo *et al.* [18]· developed biosensors based on the increased fluctuation in fluorescence intensity as two FPs were brought into proximity, and thus, through stochastic optical fluctuation imaging, showed subdiffraction-limit features of protein kinase A (PKA) activity on the cell plasma membrane.

Fluorescence lifetime

Although the fluorescence intensity is easy to measure, its limitation for reporting functional information is also apparent. The detected intensity depends on the local concentration of the fluorescent probe, and so it is difficult to quantify for absolute values. Interpretation of time-dependent signal changes is further complicated by photobleaching, which could be significant for the strongly illuminated SRM experiments.

Fluorescence-lifetime imaging microscopy (FLIM) [19] is a powerful, intensity-insensitive method for probing local environments. The exponential decay rate of fluorescence emission, typically on the time scale of nanoseconds, depends strongly on both the dye identity and dye-environment interactions, thus a valuable reporter.

For SRM, although FLIM has been successfully incorporated with STED [20-23], the focus has been on the unmixing of different dyes into separate color channels for multi-target SRM [21,23]. Lesoine et al. [22] examined Alexa Fluor 594-phalloidin-labeled actin cytoskeleton in fixed cells, and noticed varying local fluorescence lifetime in the STED image (Figure 2b), a result potentially consistent with varied quenching interactions between the tagged dye and the local components of the cell. However, as a rather Gaussian-like distribution was found for the measured lifetime at different locations, it was unclear if the observed local variations merely reflected statistical error [22]. Nonetheless, given the wide usage of FLIM for environment sensing [19], lifetime-resolved SRM stands as a promising direction for future *f*-SRM efforts.

Fluorescence polarization

Fluorescence polarization and anisotropy measurements provide information on the orientation and rotational mobility of fluorescence molecules [24]. For SRM, polarization-resolved SMLM has been achieved by splitting the fluorescence into polarizations parallel and perpendicular to the excitation laser using either a polarizing beam splitter [25] or a Wollaston prism [26,27], and by modulating the polarization orientation of the excitation laser [28]. Gould et al. [25] thus showed, through polarization FPALM, local heterogeneities in the fluorescence polarization anisotropy of overexpressed Dendra2-actin molecules in fixed fibroblasts. Cruz *et al.* [26]· performed polarization-resolved dSTORM and found certain, but not all, dyes conjugated to phalloidin exhibited restricted polarization orientations when labeled to actin stress fibers in fixed cells. For *in vitro* samples, polarization-resolved SMLM has also demonstrated preferred orientations for dyes labeled to DNA strands [26,28] and insulin amyloid fibrils [27]. Thus, polarization-resolved SRM provides orientation information of the tagged fluorophores, hence new structural, and potentially functional, insights.

Ratiometric detection of spectral shift

Ratiometric detection is a commonly used, relative simple strategy to detect the color changes of fluorescence probes. Here, a dichroic mirror splits the fluorescence into long- and short-wavelength components, respectively, and the relative intensities measured for the two components provide the spectral information.

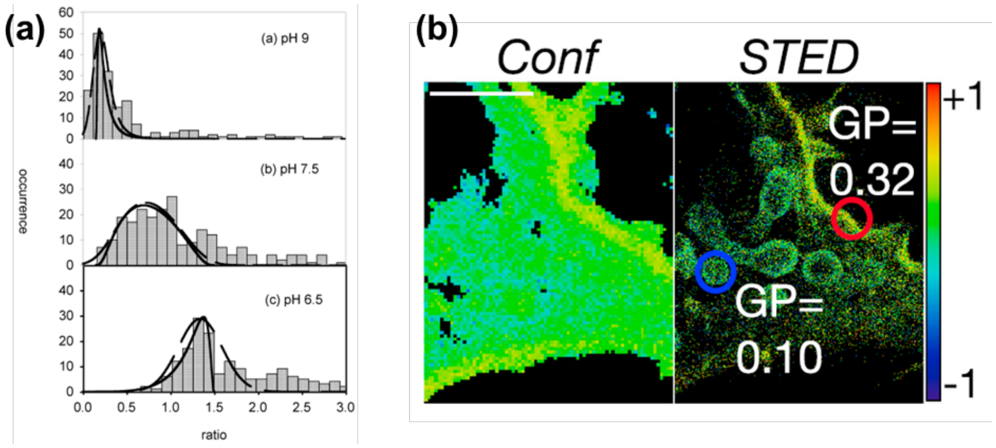

Figure 33 **f-SRM through ratiometric color detection. (a)** Histograms of the emission ratio $R = I_{580nm} / I_{640nm}$, I_{580nm} and I_{640nm} being the fluorescence intensities detected at 580 and 640 nm, respectively, for single SNARF-1-dextran molecules immobilized in agarose gels at different pH. **(b)** Ratiometric confocal and STED images of Di-4-AN(F)EPPTEA in a living CHO cell. Color denotes the generalized polarization (GP), $(I_1 - I_2)/(I_1 + I_2)$, where I_1 and I_2 are the fluorescence intensities detected in the 520-570 nm and 620-700 nm channels, respectively. Endocytic vesicles (blue circle) show smaller GP values than the plasma membrane (red circle). Scale bar: 500 nm. Panel (a) is adapted from [29]. Panel (b) is adapted from [30].

For single-molecule imaging, Brasselet and Moerner [29] investigated the local pH in agarose gels by sparsely doping dextran molecules tagged with SNARF-1, a fluorescent pH indicator. The pH-dependent spectral shift was measured as the ratio of single-molecule emission between two wavelengths centered at 580 and 640 nm. Interestingly, although the mean values from single-molecule ensembles matched that of bulk measurements, histograms of emission ratios of individual molecules at different pH revealed more scattered distributions at intermediate pH (Figure 3a). This difference suggests higher spatial heterogeneity of protonation chemistry at intermediate pH, which could not have been detected with ensemble measurements. Extending related approaches to SMLM-type SRM [31-33] and to cells represents future challenges.

For STED SRM, Sezgin *et al.* [30]•• achieved ratiometric spectral detection for several polarity-sensitive, solvatochromic membrane probes. The 3-fold enhancement of spatial resolution over confocal microscopy was instrumental in revealing local polarity differences. In particular, for Di-4-AN(F)EPPTEA-labeled live cells, STED detected significantly smaller generalized polarization (GP) values, and thus reduced local molecular order, for endocytic vesicles near the plasma membrane, a result that was obscure under diffraction-limited confocal spectral imaging (Figure 3b). Together with the above-discussed STED-FLIM experiments, it appears *f*-SRM through combing environment-sensing dyes with STED could lead to great promises.

Spectrally resolved super-resolution microscopy

The full power of integrating spectrum-changing fluorescent probes with SRM is unleashed by the recent rise of spectrally resolved SMLM (SR-SMLM) [34]. Whereas for conventional fluorescence microscopy, to measure the actual emission spectra (beyond ratiometric detection) necessitates spatially confined illumination or detection to avoid convolution of the spectral and spatial signal, single fluorescent molecules are, in themselves, self-confined point sources. By dispersing the emission of many single molecules simultaneously in the wide field and implementing fluorescence on-off switching, the spectra of millions of individual molecules can be obtained within minutes [35]·. Assembling such spectral information, together with the super-localized positions of the same molecules, thus enables SR-SMLM.

The initial demonstrations of SR-SMLM aimed at multicolor SRM [35-37]. Zhang *et al.* [35]· demonstrated that with spectrally resolved STORM, four dyes only ~10 nm apart in emission wavelength can be distinguished with negligible misidentification when labeled to different targets in fixed mammalian cells. Moreover, excellent three-dimensional (3D) spatial resolution was obtained for every dye, and the obtained 3D SRM images for all dyes were automatically aligned with the same coordinates. The rather narrow distribution of single-molecule spectra in this work contrasted early results of single molecules at solid surfaces [38-41], and indicated that the single-molecule fluorescence of many dyes was insensitive to the local environments in fixed cells. In comparison, Mlodzianoski *et al.* [36] carried out spectrally resolved FPALM, and noticed spectral wandering for a fraction of the detected single-molecule fluorescence of FPs in fixed cells, the mechanism of which remains to be elucidated.

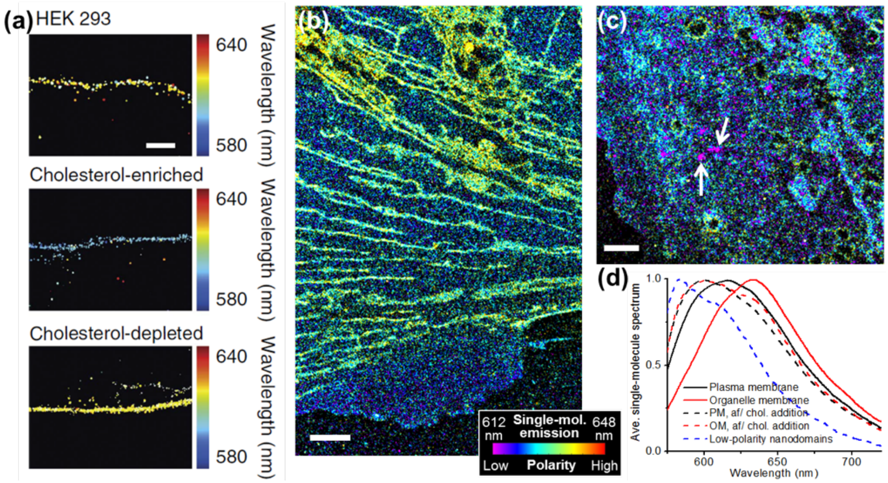

Figure 34. **f-SRM through spectrally resolved super-resolution microscopy. (a)** Grating-based spectrally resolved PAINT image of the side view of the Nile Red-labeled plasma membrane of HEK293 cells, untreated, cholesterol-enriched, or cholesterol-depleted. Redder emission corresponds to higher solvent polarity (lower hydrophobicity). **(b)** Prism-based spectrally resolved PAINT image of the in-plane view of the Nile Red-labeled membrane system of a live PtK2 cell. **(c)** Prism-based spectrally resolved STORM image of the Nile Red-labeled membrane system of a cholesterol-added COS-7 cell. Arrows point to low-polarity nanodomains. **(d)** Averaged single-molecule spectra at the plasma membrane (PM), organelle membrane (OM), and the low-polarity nanodomains. Scale bars: 100 nm (a); 2 μm (b,c). Panel (a) is adapted from [42]. Panels (b-d) are adapted from [43].

For *f*-SRM, Bongiovanni *et al.* [42]•• employed Nile Red, a widely studied solvatochromic dye [44], to enable surface hydrophobicity mapping through grating-based spectrally resolved PAINT. This enabled the probing of surface hydrophobicity for *in vitro* protein aggregates of α-synuclein and amyloid-β. In particular, it was found that the amyloid fibers have different surface hydrophobicity from their constituting oligomers, which may relate to cellular toxicity. For cells, this work visualized the hydrophobicity of cell plasma membranes in a side-view geometry, and noted spectral shifts for cholesterol-enriched and cholesterol-depleted conditions (Figure 4a).

Moon *et al.* [43]•• utilized spectrally resolved STORM and spectrally resolved PAINT, in combination with Nile Red staining, to reveal nanoscale heterogeneity in cell membranes. As a prism was used to attain a weaker dispersion for less overlapping of single-molecule spectra, as well as to reduce photon loss, the same strategy adopted in the original work of spectrally resolved STORM [35], this work enabled *f*-SRM mapping of the local chemical polarity for dense structures as in-plane views of the membrane system of live mammalian cells (Figure 4b). This helped reveal distinct polarity characteristics of the plasma membrane vs. the membranes of nanoscale intracellular organelles, with the latter being more polar (less hydrophobic) (Figure 4bd), in line with their expected biological functions. Cholesterol manipulation further showed that this striking contrast in local chemical polarity was driven by differences in the local cholesterol level. Moreover, *f*-SRM unveiled the formation of low-polarity, raft-like nanodomains upon cholesterol addition (Figure 4cd) or cholera toxin B treatment conditions, thus shedding new light onto a contentious subject [45,46].

Xiang *et al.* [47]• recently showed that *f*-SRM based on spectrally resolved PAINT could be extended to probe the nanoscale structure and composition of organic layers adsorbed on glass surfaces. One remarkable finding was that mixtures of miscible liquids spontaneously demixed into nanodroplets of varying compositions and sizes on the glass surface. Although this study did not involve cells, it provided new insights into the phase separation behaviors of molecules at the nanoscale, and so could inspire future work on understanding related intracellular processes [48].

Outlook

In conclusion, *f*-SRM has emerged over the past few years as a new class of powerful methodologies to address the highly intriguing, yet highly challenging, *functional* aspects of cell biology at the nanoscale. Diverse physicochemical parameters have been examined, and numerous strategies have been invoked to encode the sought functions, in many cases prompting the development of new optical tools that access new dimensions of the SRM readout. We expect future work to expand on existing possibilities by both encoding untested new functions and by further exploring other possible dimensionalities of the SRM signal, including through correlated approaches that tap into the power of other microscopy and spectroscopy techniques [49]. Throughout such endeavors, the development and/or identification of suitable, environmentally sensitive fluorescent probes undoubtedly hold the key. Thus, the multifunctional and multidimensional approach of *f*-SRM relies on multidisciplinary efforts; its future success demands in-depth discussion and collaboration between researchers across diverse fields.

Acknowledgments

We thank all past and current lab members for contribution. This work was supported by the National Science Foundation (CHE-1554717), the Beckman Young Investigator Program, the Packard Fellowships for Science and Engineering, and the Bakar Fellows Award. K.X. is a Chan Zuckerberg Biohub investigator.

References and recommended reading

1. Sahl, S. J., Hell, S. W. & Jakobs, S. Fluorescence nanoscopy in cell biology. *Nat. Rev. Mol. Cell Biol.* **18,** 685-701 (2017).
2. Sigal, Y. M., Zhou, R. & Zhuang, X. Visualizing and discovering cellular structures with super-resolution microscopy. *Science* **361,** 880-887 (2018).
3. Rust, M. J., Bates, M. & Zhuang, X. Sub-diffraction-limit imaging by stochastic optical reconstruction microscopy (STORM). *Nature methods* **3,** 793-796 (2006).
4. Betzig, E., Patterson, G. H., Sougrat, R., Lindwasser, O. W., Olenych, S., Bonifacino, J. S., Davidson, M. W., Lippincott-Schwartz, J. & Hess, H. F. Imaging intracellular fluorescent proteins at nanometer resolution. *Science* **313,** 1642-1645 (2006).
5. Hess, S. T., Girirajan, T. P. K. & Mason, M. D. Ultra-high resolution imaging by fluorescence photoactivation localization microscopy. *Biophys. J.* **91,** 4258-4272 (2006).
6. Sharonov, A. & Hochstrasser, R. M. Wide-field subdiffraction imaging by accumulated binding of diffusing probes. *Proc. Natl. Acad. Sci. U. S. A.* **103,** 18911-18916 (2006).
7. Hell, S. W. & Wichmann, J. Breaking the diffraction resolution limit by stimulated-emission - stimulated-emission-depletion fluorescence microscopy. *Opt. Lett.* **19,** 780-782 (1994).
8. Klar, T. A., Jakobs, S., Dyba, M., Egner, A. & Hell, S. W. Fluorescence microscopy with diffraction resolution barrier broken by stimulated emission. *Proc. Natl. Acad. Sci. U. S. A.* **97,** 8206-8210 (2000).
9. Wöll, D. & Flors, C. Super-resolution fluorescence imaging for materials science. *Small Methods* **1,** 1700191 (2017).
10. Theillet, F. X., Binolfi, A., Frembgen-Kesner, T., Hingorani, K., Sarkar, M., Kyne, C., Li, C. G., Crowley, P. B., Gierasch, L., Pielak, G. J., Elcock, A. H., Gershenson, A. & Selenko, P. Physicochemical properties of cells and their effects on intrinsically disordered proteins (IDPs). *Chem. Rev.* **114,** 6661-6714 (2014).
11. Yang, Z., Cao, J., He, Y., Yang, J. H., Kim, T., Peng, X. & Kim, J. S. Macro-/micro-environment-sensitive chemosensing and biological imaging. *Chem. Soc. Rev.* **43,** 4563-4601 (2014).
12. National_Research_Council *Visualizing chemistry : the progress and promise of advanced chemical imaging* (National Academies Press, Washington, DC, 2006).
13. Chan, J., Dodani, S. C. & Chang, C. J. Reaction-based small-molecule fluorescent probes for chemoselective bioimaging. *Nat. Chem.* **4,** 973-984 (2012).
14. Schaferling, M. The art of fluorescence imaging with chemical sensors. *Angew. Chem.-Int. Edit.* **51,** 3532-3554 (2012).
15. Li, X. H., Gao, X. H., Shi, W. & Ma, H. M. Design strategies for water-soluble small molecular chromogenic and fluorogenic probes. *Chem. Rev.* **114,** 590-659 (2014).
16. Klymchenko, A. S. Solvatochromic and fluorogenic dyes as environment-sensitive probes: design and biological applications. *Acc. Chem. Res.* **50,** 366-375 (2017).

17. Mishina, N. M., Mishin, A. S., Belyaev, Y., Bogdanova, E. A., Lukyanov, S., Schultz, C. & Belousov, V. V. Live-cell STED microscopy with genetically encoded biosensor. *Nano Lett.* **15,** 2928-2932 (2015).
18. Mo, G. C. H., Ross, B., Hertel, F., Manna, P., Yang, X. X., Greenwald, E., Booth, C., Plummer, A. M., Tenner, B., Chen, Z., Wang, Y. X., Kennedy, E. J., Cole, P. A., Fleming, K. G., Palmer, A., Jimenez, R., Xiao, J., Dedecker, P. & Zhang, J. Genetically encoded biosensors for visualizing live-cell biochemical activity at super-resolution. *Nat. Methods* **14,** 427-434 (2017).
19. Berezin, M. Y. & Achilefu, S. Fluorescence lifetime measurements and biological imaging. *Chem. Rev.* **110,** 2641-2684 (2010).
20. Auksorius, E., Boruah, B. R., Dunsby, C., Lanigan, P. M. P., Kennedy, G., Neil, M. A. A. & French, P. M. W. Stimulated emission depletion microscopy with a supercontinuum source and fluorescence lifetime imaging. *Opt. Lett.* **33,** 113-115 (2008).
21. Bückers, J., Wildanger, D., Vicidomini, G., Kastrup, L. & Hell, S. W. Simultaneous multi-lifetime multi-color STED imaging for colocalization analyses. *Opt. Express* **19,** 3130-3143 (2011).
22. Lesoine, M. D., Bose, S., Petrich, J. W. & Smith, E. A. Supercontinuum stimulated emission depletion fluorescence lifetime imaging. *J. Phys. Chem. B* **116,** 7821-7826 (2012).
23. Niehorster, T., Loschberger, A., Gregor, I., Kramer, B., Rahn, H. J., Patting, M., Koberling, F., Enderlein, J. & Sauer, M. Multi-target spectrally resolved fluorescence lifetime imaging microscopy. *Nat. Methods* **13,** 257-262 (2016).
24. Jameson, D. M. & Ross, J. A. Fluorescence polarization/anisotropy in diagnostics and imaging. *Chem. Rev.* **110,** 2685-2708 (2010).
25. Gould, T. J., Gunewardene, M. S., Gudheti, M. V., Verkhusha, V. V., Yin, S. R., Gosse, J. A. & Hess, S. T. Nanoscale imaging of molecular positions and anisotropies. *Nat. Methods* **5,** 1027-1030 (2008).
26. Cruz, C. A. V., Shaban, H. A., Kress, A., Bertaux, N., Monneret, S., Mavrakis, M., Savatier, J. & Brasselet, S. Quantitative nanoscale imaging of orientational order in biological filaments by polarized superresolution microscopy. *Proc. Natl. Acad. Sci. U. S. A.* **113,** E820-E828 (2016).
27. Shaban, H. A., Valades-Cruz, C. A., Savatier, J. & Brasselet, S. Polarized super-resolution structural imaging inside amyloid fibrils using Thioflavine T. *Sci Rep* **7,** 12482 (2017).
28. Backer, A. S., Lee, M. Y. & Moerner, W. E. Enhanced DNA imaging using super-resolution microscopy and simultaneous single-molecule orientation measurements. *Optica* **3,** 659-666 (2016).
29. Brasselet, S. & Moerner, W. E. Fluorescence behavior of single-molecule pH-sensors. *Single Molecules* **1,** 17-23 (2000).
30. Sezgin, E., Schneider, F., Zilles, V., Urbancic, I., Garcia, E., Waithe, D., Klymchenko, A. S. & Eggeling, C. Polarity-sensitive probes for superresolution stimulated emission depletion microscopy. *Biophys. J* **113,** 1321-1330 (2017).
31. Bossi, M., Folling, J., Belov, V. N., Boyarskiy, V. P., Medda, R., Egner, A., Eggeling, C., Schonle, A. & Hell, S. W. Multicolor far-field fluorescence nanoscopy through isolated detection of distinct molecular species. *Nano Lett.* **8,** 2463-2468 (2008).

32. Testa, I., Wurm, C. A., Medda, R., Rothermel, E., von Middendorf, C., Folling, J., Jakobs, S., Schonle, A., Hell, S. W. & Eggeling, C. Multicolor fluorescence nanoscopy in fixed and living cells by exciting conventional fluorophores with a single wavelength. *Biophys. J.* **99,** 2686-2694 (2010).
33. Gunewardene, M. S., Subach, F. V., Gould, T. J., Penoncello, G. P., Gudheti, M. V., Verkhusha, V. V. & Hess, S. T. Superresolution imaging of multiple fluorescent proteins with highly overlapping emission spectra in living cells. *Biophys. J.* **101,** 1522-1528 (2011).
34. Yan, R., Moon, S., Kenny, S. J. & Xu, K. Spectrally resolved and functional super-resolution microscopy via ultrahigh-throughput single-molecule spectroscopy. *Accounts Chem. Res.* **51,** 697-705 (2018).
35. Zhang, Z., Kenny, S. J., Hauser, M., Li, W. & Xu, K. Ultrahigh-throughput single-molecule spectroscopy and spectrally resolved super-resolution microscopy. *Nat. Methods* **12,** 935-938 (2015).
36. Mlodzianoski, M. J., Curthoys, N. M., Gunewardene, M. S., Carter, S. & Hess, S. T. Super-resolution imaging of molecular emission spectra and single molecule spectral fluctuations. *PLoS One* **11,** e0147506 (2016).
37. Dong, B. Q., Almassalha, L., Urban, B. E., Nguyen, T. Q., Khuon, S., Chew, T. L., Backman, V., Sun, C. & Zhang, H. F. Super-resolution spectroscopic microscopy via photon localization. *Nat. Commun.* **7,** 12290 (2016).
38. Trautman, J. K., Macklin, J. J., Brus, L. E. & Betzig, E. Near-field spectroscopy of single molecules at room-temperature. *Nature* **369,** 40-42 (1994).
39. Macklin, J. J., Trautman, J. K., Harris, T. D. & Brus, L. E. Imaging and time-resolved spectroscopy of single molecules at an interface. *Science* **272,** 255-258 (1996).
40. Xie, X. S. & Trautman, J. K. Optical studies of single molecules at room temperature. *Annu. Rev. Phys. Chem.* **49,** 441-480 (1998).
41. Lu, H. P. & Xie, X. S. Single-molecule spectral fluctuations at room temperature. *Nature* **385,** 143-146 (1997).
42. Bongiovanni, M. N., Godet, J., Horrocks, M. H., Tosatto, L., Carr, A. R., Wirthensohn, D. C., Ranasinghe, R. T., Lee, J. E., Ponjavic, A., Fritz, J. V., Dobson, C. M., Klenerman, D. & Lee, S. F. Multi-dimensional super-resolution imaging enables surface hydrophobicity mapping. *Nat. Commun.* **7,** 13544 (2016).
43. Moon, S., Yan, R., Kenny, S. J., Shyu, Y., Xiang, L., Li, W. & Xu, K. Spectrally resolved, functional super-resolution microscopy reveals nanoscale compositional heterogeneity in live-cell membranes. *J. Am. Chem. Soc.* **139,** 10944-10947 (2017).
44. Greenspan, P. & Fowler, S. D. Spectrofluorometric studies of the lipid probe, nile red. *J. Lipid Res.* **26,** 781-789 (1985).
45. Lingwood, D. & Simons, K. Lipid rafts as a membrane-organizing principle. *Science* **327,** 46-50 (2010).
46. Sevcsik, E. & Schutz, G. J. With or without rafts? Alternative views on cell membranes. *Bioessays* **38,** 129-139 (2016).
47. Xiang, L., Wojcik, M., Kenny, S. J., Yan, R., Moon, S., Li, W. & Xu, K. Optical characterization of surface adlayers and their compositional demixing at the nanoscale. *Nat. Commun.* **9,** 1435 (2018).
48. Shin, Y. & Brangwynne, C. P. Liquid phase condensation in cell physiology and disease. *Science* **357,** eaaf4382 (2017).

49. Hauser, M., Wojcik, M., Kim, D., Mahmoudi, M., Li, W. & Xu, K. Correlative super-resolution microscopy: new dimensions and new opportunities. *Chem. Rev.* **117,** 7428-7456 (2017).